



IST-2000-30148 I-METRA

D2

Channel Characterisation

| | |
|---|---|
| Contractual Date of Delivery to the CEC: | 31 October, 2002 |
| Actual Date of Delivery to the CEC: | 31 October 2002 |
| Author(s): | Jean Philippe Kermaol, Laurent Schumacher, Preben Mogensen |
| Participant(s): | AAU |
| Workpackage: | WP2: Channel Characterisation |
| Est. person months: | 6 |
| Security: | Public |
| Nature: | Report |
| Version: | 1.1 |
| Total number of pages: | 112 |

Abstract:

This deliverable documents a thorough investigation of the propagation properties of MIMO (Multi Input Multi Output) radio channels. This study is based on the extensive MIMO measurement campaigns performed during the ACTS SUNBEAM and IST METRA projects. Based on this propagation study, an upgrade of the stochastic MIMO radio channel model proposed by METRA is presented, which embeds the most significant findings of the analysis. The upgrade has also been designed to comply with the evolution of the 3GPP standardisation (as of April 2002). The upgraded model has been implemented in MATLAB[®], along with tools enabling to derive the correlation coefficients of Multiple Element Arrays (MEA) from a high-level description of their deployment and of the propagation scenario. The measured data have been used to validate the upgraded model for the polarization diversity in narrowband cases. Finally, the performances of MIMO systems are evaluated from measured and simulated data by means of theoretical Shannon capacity results. A significant part of this work can be seen as a follow-up of the work presented in IST METRA Deliverable 2.

Keyword list: MIMO channel propagation analysis, Eigenanalysis, Correlation, MIMO performance evaluation.

0 EXECUTIVE SUMMARY

This deliverable investigates the propagation parameters which influence the performances of a new technology known as MIMO (Multi Input Multi Output). It involves a state-of-the-art combination of MEAs (Multi Element Array) and digital signal processing. The MIMO concept is defined as a radio link with M elements at one end and N elements at the other end. The benefit of the MIMO technology comes from the creation of $\min(M,N)$ orthogonal information subchannels, the combination of Tx and Rx diversity, and the increased antenna gain.

The performance of the MIMO technology depends directly on the propagation properties of the MIMO channel, through the correlation coefficients, the BPRs (Branch Power Ratios) at the MEAs, the polarisation, etc. It is therefore of paramount importance to gain a good insight in these properties. This deliverable therefore presents a thorough analysis of measured data collected during ACTS SUNBEAM [2] and IST METRA [1] projects. The results of this analysis give a better understanding of the MIMO propagation channel and on the performances to be achieved through it. They also deliver sets of significant parameters that characterise MIMO channels and enable their simulation.

The present deliverable also describes an upgrade of the MIMO radio channel which benefits from the findings of the propagation analysis and complies with the evolution of the 3GPP standardisation (as of April 2002). This upgraded model has been implemented on the MATLAB[®] simulation platform, along with tools to derive the correlation coefficients of MEAs in a variety of scattering scenarios. The measured data are used to validate a stochastic MIMO radio channel model for the polarization domain in the narrowband condition.

Finally, the performance of the MIMO technology is evaluated by means of theoretical Shannon capacity results derived from measured and simulated data.

At the end of this propagation study, conclusions and recommendations are proposed in order to implement the MIMO technology in the most efficient manner. Radio propagation results indicate that high data rates are achievable with a large number of decorrelated elements at both MEAs and large SNRs (Signal to Noise Ratio). One could claim that these conditions would be fulfilled in WLAN applications. However, in the case of UMTS, the typical operating SNR and the lack of space on the handset could be an issue.

The reading of the IST METRA Deliverable 2 [1] and the ACTS SUNBEAM Deliverable D411 [2] is a prerequisite to fully understand the measurement analysis presented in the present document. Parts of this deliverable have been presented as PhD thesis [3].

1 ACKNOWLEDGEMENT

The authors would like to thank Juha Ylitalo and Esa Tiirola from Nokia Networks (Oulu) for their help during the beamforming analysis of the measured data.

DISCLAIMER

The work associated with this report has been carried out in accordance with the highest technical standards and the I-METRA partners have endeavoured to achieve the degree of accuracy and reliability appropriate to the work in question. However since the partners have no control over the use to which the information contained within the report is to be put by any other party, any other such party shall be deemed to have satisfied itself as to the suitability and reliability of the information in relation to any particular use, purpose or application.

Under no circumstances will any of the partners, their servants, employees or agents accept any liability whatsoever arising out of any error or inaccuracy contained in this report (or any further consolidation, summary, publication or dissemination of the information contained within this report) and/or the connected work and disclaim all liability for any loss, damage, expenses, claims or infringement of third party rights.

| | | |
|----------|--|-----------|
| 0 | EXECUTIVE SUMMARY | 2 |
| 1 | ACKNOWLEDGEMENT | 3 |
| 2 | NOTATIONS | 7 |
| 2.1 | ACRONYMS | 7 |
| 2.2 | MATHEMATICAL OPERATORS | 7 |
| 2.3 | SYMBOLS | 8 |
| 3 | INTRODUCTION | 10 |
| 3.1 | MIMO SYSTEMS | 10 |
| 3.2 | A BETTER INSIGHT INTO MIMO CHANNELS | 11 |
| 3.3 | OUTLINE OF THE DELIVERABLE | 12 |
| 4 | GENERAL BACKGROUND INFORMATION | 13 |
| 4.1 | INTRODUCTION | 13 |
| 4.2 | GENERAL MIMO STRUCTURE | 13 |
| 4.3 | THE EIGENANALYSIS METHOD AND INTERPRETATION | 14 |
| 4.4 | THE MIMO PROPAGATION SCENARIOS | 17 |
| 4.5 | THE ANTENNA AND DIVERSITY GAIN ASPECT | 18 |
| 4.5.1 | Temporal Illustration of the Eigenvalue | 19 |
| 4.5.2 | Antenna Gain | 20 |
| 4.5.3 | Diversity Gain | 21 |
| 4.5.4 | The Capacity Aspect | 22 |
| 4.5.5 | Water-filling Power Allocation | 23 |
| 4.5.6 | Uniform Power Allocation Scheme | 24 |
| 4.6 | CORRELATION DEFINITION | 25 |
| 4.7 | BRANCH POWER RATIO | 27 |
| 4.8 | MINI-GLOSSARY OF MIMO TERMINOLOGY | 27 |
| 4.9 | SUMMARY AND INTERIM CONCLUSION | 28 |
| 5 | CHARACTERISATION OF THE RADIO CHANNEL | 30 |
| 5.1 | FROM WIDEBAND TO NARROWBAND | 30 |
| 5.2 | STATISTICAL DISTRIBUTION OF THE NB SIGNAL | 32 |
| 5.3 | ANALYSIS OF THE DIRECTION OF ARRIVAL | 34 |
| 5.3.1 | Geometrical Constraint | 35 |
| 5.3.2 | A Conventional Beamforming DoA Algorithm | 40 |
| 5.3.3 | DoA Results Characterisation | 41 |
| 5.4 | POWER CORRELATION COEFFICIENT ANALYSIS | 44 |
| 5.4.1 | Spatial Domain | 45 |
| 5.4.2 | Polarization, Joint Spatial-Polarization and Joint Pattern-Spatial-Polarization Domain | 48 |
| 5.5 | REFERENCE PROPAGATION PATHS | 54 |
| 5.5.1 | Example 1 | 54 |
| 5.5.2 | Example 2 | 55 |
| 5.5.3 | Example 3 | 55 |
| 5.5.4 | Example 4 | 55 |
| 5.5.5 | Example 5 | 55 |
| 5.5.6 | Example 6 | 55 |
| 5.6 | SUMMARY AND INTERIM CONCLUSION | 56 |
| 6 | UPDATED VERSION OF THE IST METRA MIMO RADIO CHANNEL MODEL | 57 |
| 6.1 | HOW TO APPLY THE MODEL | 57 |
| 6.2 | LIMITATIONS TO THE MODEL | 59 |

| | | |
|-----------|--|------------|
| 6.3 | EXPERIMENTAL VALIDATION IN THE SPATIAL DOMAIN..... | 60 |
| 6.4 | EXPERIMENTAL VALIDATION IN THE POLARIZATION DOMAIN..... | 61 |
| 6.5 | SUMMARY AND INTERIM CONCLUSION..... | 63 |
| 7 | MATLAB IMPLEMENTATION OF THE MIMO RADIO CHANNEL..... | 64 |
| 7.1 | FOREWORD - MOTIVATIONS..... | 64 |
| 7.2 | INTRODUCTION..... | 64 |
| 7.3 | SPATIAL CORRELATION – DIRECTORY <i>CORRELATION_MULTIPLE_CLUSTER</i> | 66 |
| 7.4 | MIMO RADIO CHANNEL – DIRECTORY <i>UMTS_TESTBED</i> | 68 |
| 7.4.1 | Initialisation phase..... | 68 |
| 7.4.2 | Processing phase..... | 70 |
| 7.4.3 | Post-processing phase..... | 72 |
| 7.5 | LIMITATIONS OF THE IMPLEMENTATION..... | 75 |
| 7.6 | DISTRIBUTION TERMS..... | 75 |
| 7.7 | DISTRIBUTION STATISTICS..... | 76 |
| 7.8 | SUMMARY AND INTERIM CONCLUSION..... | 76 |
| 8 | PERFORMANCE EVALUATION OF THE MIMO RADIO CHANNEL..... | 77 |
| 8.1 | IMPACT OF THE RADIO CHANNEL ON THE MIMO PERFORMANCE..... | 77 |
| 8.1.1 | Spatial Domain..... | 78 |
| 8.1.2 | Impact of the MEA Topology..... | 81 |
| 8.1.3 | Polarization Domain..... | 82 |
| 8.1.4 | Joint Spatial-Polarisation Domain..... | 85 |
| 8.2 | BRANCH POWER RATIO: A PRACTICAL ISSUE..... | 91 |
| 8.2.1 | SIMO Approach..... | 92 |
| 8.2.2 | MIMO Approach..... | 94 |
| 8.2.3 | Capacity Results..... | 96 |
| 8.3 | CAPACITY RESULTS FOR MICROCELL AND PICOCELL..... | 98 |
| 8.4 | SUMMARY AND INTERIM CONCLUSION..... | 101 |
| 9 | CONCLUSIONS..... | 102 |
| 10 | APPENDIX A - EXPERIMENTAL VALIDATION IN THE POLARIZATION DOMAIN.... | 104 |
| 10.1 | MIMO STRUCTURE CONSIDERING POLARIZATION DIVERSITY..... | 104 |
| 10.2 | EXPERIMENTAL IMPLEMENTATION OF MIMO IN THE POLARIZATION DOMAIN..... | 105 |
| 10.3 | THE CORRELATION ASSUMPTION WITH RESPECT TO POLARIZATION..... | 105 |
| 10.4 | DETERMINATION OF THE MODEL OPTION..... | 108 |
| 11 | REFERENCES..... | 110 |

2 NOTATIONS

2.1 Acronyms

| | |
|-------|--|
| 2-D | Two Dimensional |
| 3GPP | 3rd Generation Partnership Project |
| AoA | Angle of Arrival |
| AoD | Angle of Departure |
| AS | Azimuth Spread |
| BPR | Branch Power Ratio |
| BS | Base Station |
| CDF | Cumulative Distribution Function |
| DoA | Direction of Arrival |
| DoD | Direction of Departure |
| EVD | EigenValue Decomposition |
| FDD | Frequency Division Duplex |
| ISM | Industrial, Scientific, and Medical |
| LOS | Line-of-Sight |
| MEA | Multi Element Array |
| MIMO | Multi Input Multi Output |
| MISO | Multiple Input Single Output |
| NB | NarrowBand |
| PAS | Power Azimuth Spectrum |
| PDP | Power Delay Profile |
| RMS | Root Mean Square |
| Rx | Receiver |
| SIMO | Single Input Multiple Output |
| SISO | Single Input Single Output |
| SNR | Signal to Noise Ratio |
| SVD | Singular Value Decomposition |
| TDD | Time Division Duplex |
| Tx | Transmitter |
| ULA | Uniform Linear Array |
| UMTS | Universal Mobile Telecommunications System |
| WCDMA | Wideband Code Division Multiple Access |
| WLAN | Wireless Local Area Network |

2.2 Mathematical Operators

| | |
|--------------------------------|-------------------------------------|
| \cdot^* | Complex conjugate operation |
| $[\cdot]^H$ | Hermitian transpose operation |
| $[\cdot]^T$ | Transpose operation |
| $\bar{X} = \mathbf{E}[X]$ | Expectation over time (or distance) |
| $\langle \cdot, \cdot \rangle$ | Correlation coefficient operation |

| | |
|-------------------------|---|
| Re{.} | Returns the real part of the complex argument |
| ^(w) = | Water-filling power allocation scheme |
| ^(u) = | Uniform power allocation scheme |
| <i>det(.)</i> | Determinant |
| <i>log₁₀</i> | Logarithm base 10 |
| <i>log₂</i> | Logarithm base 2 |
| <i>Rank(.)</i> | Return the rank of a matrix |
| <i>min(.)</i> | Return the minimum of the argument |
| <i>vec(.)</i> | Reshapes a matrix into a column vector |
| <i>M</i> × <i>N</i> | <i>M</i> by <i>N</i> matrix dimension |
| <i>A</i> × <i>B</i> | Element by element multiplication of the matrices <i>A</i> and <i>B</i> |

2.3 Symbols

| | |
|-------------------------------|---|
| $\alpha_{mn}(t)$ | Complex NB transmission coefficient |
| $\alpha_{mn}^{wb}(t, \tau_l)$ | Measured complex IR between the <i>m</i> th and the <i>n</i> th MEA element |
| <i>t</i> | Time |
| τ | Delay |
| γ_k | <i>k</i> th eigenvalue |
| σ_k | <i>k</i> th Singular value |
| λ_k | Normalized <i>k</i> th eigenvalue |
| <i>n</i> | Index of MEA elements at the MS |
| <i>m</i> | Index of MEA elements at the BS |
| <i>y(t)</i> | Received signal vector |
| <i>y_m(t)</i> | Received signals |
| <i>s(t)</i> | Transmitted vector signal |
| <i>s_n(t)</i> | Transmitted signals |
| <i>H</i> | NB MIMO channel transfer matrix |
| <i>R</i> | Instantaneous correlation matrix |
| <i>U</i> | Left unitary matrices |
| <i>u</i> | Left singular vector |
| <i>V</i> | Right unitary matrices |
| <i>v</i> | Right singular vector |
| <i>K</i> | Number of parallel subchannels |
| <i>k</i> | Index of the parallel subchannel |
| ζ | SNR |
| ζ_k | SNR per <i>k</i> th subchannel |
| σ_n^2 | Noise power |
| ρ | Correlation coefficient |
| ρ_{cplx} | Correlation coefficient: Complex domain |
| ρ_{env} | Correlation coefficient: Magnitude (envelope) domain |
| ρ_{power} | Correlation coefficient: Power domain |

| | |
|--------------------------|--|
| $ \rho_{S\Delta_i} $ | Correlation coefficient: spatial domain with a spatial distance Δ_i |
| $ \rho_P $ | Correlation coefficient: Polarization domain |
| $ \rho_{S\Delta_i+P} $ | Correlation coefficient: joint spatial-polarization domain |
| $ \rho_{R+P+S\Delta_i} $ | Correlation coefficient: joint pattern-spatial-polarization domain |
| σ | RMS delay spread |
| $\sigma_{channel}$ | RMS delay spread of the channel |
| σ_{system} | RMS delay spread of the measurement system |
| D | Effective aperture of the MEA |
| f_o | Nyquist criteria |
| f_{max} | Highest frequency component in the signal |
| d_o | Spatial Nyquist criteria |
| $BW_{[3dB]}$ | Half power beamwidth |
| Ω | Number of linear elements in the MEA along broadside |
| d | Actual element separation |
| C | Capacity normalized to the system bandwidth |
| K -factor | Ricean factor |

3 INTRODUCTION

3.1 MIMO systems

In conventional communication systems, one antenna at the transmitter (Tx) and one at the receiver (Rx)—a so called SISO (Single Input Single Output) antenna system—creates a bottleneck in terms of capacity. Whatever the modulation scheme used, the coding strategy employed, or other system artefacts, the radio channel will always set the limit for the telecom engineers. This situation is rather critical in the current wireless communication market since the user demand for higher data rates is increasing. For instance, the wireless Internet connection is the next step for the users to be connected to the web while being on the move. To increase the capacity of wireless systems, three options are usually considered: the deployment of additional Base Stations (BS), the exploitation of more bandwidth, and/or transmissions with higher spectral efficiency.

More BS involves tighter network planning and the deployment of narrower cells, which is a very onerous way of increasing the capacity. On the other hand, some believe that the answer to the demand for high data rates lies in the millimetre wave band because more bandwidth is available there. However, this technology is still expensive. Furthermore, both UMTS¹ [1] and WLAN² [5], regarded today as suitable wireless technologies depending on the scenario, work at microwave band, e.g. 2 GHz for UMTS and 2 and 5 GHz for WLAN systems. As a result, the use of higher frequencies does not seem to be the short-term answer to nowadays wireless needs. The motivation of this deliverable is therefore to investigate the potentialities of a recently introduced technology referred to as MIMO (Multi Input Multi Output) from a physical, propagation point-of-view. MIMO involves a state-of-the-art combination of MEA (Multi Element Array) and digital signal processing in order to achieve higher spectral efficiency.

Claude E. Shannon (1916-2001) derived a formula to evaluate the information theory capacity C of a transmission channel, normalized with respect to the bandwidth and expressed as a function of the signal to noise ratio (SNR), ζ . The relation he obtained, $C = \log_2(1 + \zeta)$, means that for SNRs $\gg 1$, a 3 dB increase in SNR results in an enhancement of the capacity by 1 b/s/Hz. In a single user scenario, the SNR is basically related to the thermal noise. A method to increase it, and subsequently the capacity, is to increase the Tx power. However, this solution is not recommended, not only for health reasons [6], due to the exposure to electromagnetic radiation, but also due to the fact that transmitting higher powers requires that power amplifiers operate linearly in higher regime. This is a difficult task for the hardware designer, not mentioning the heat dissipation due to higher Tx powers. Moreover, in interference-limited cellular scenarios

¹ UMTS: Universal Mobile Telecommunications System

² WLAN: Wireless Local Area Network

the noise floor, usually higher than the thermal noise, is due to the interfering users. Increasing the Tx power would therefore not help to increase the capacity.

Another method to increase the capacity would be to improve the received SNR by using diversity techniques along with some optimum combining technique. For some years, the use of MEAs at the Rx, namely the fixed terminal, considering one single element at the Tx has been the subject of a lot of research activity, [7], [8] among others, and was designated as SIMO (Single Input Multiple Output) system. Similarly at the Tx, the UMTS WCDMA³ standard supports transmit diversity using a single element at the Rx, which is equivalent to a MISO (Multiple Input Single Output) system [9].

The natural evolution of the SIMO and MISO technologies is to provide MEAs at both ends of the radio link, hence creating a MIMO system. Telatar [10] showed that a huge capacity gain compared to SISO can be achieved using the generalised form of the Shannon equation when considering MIMO technology. The benefit of using the MIMO technology results from a combination of multiplexing, combining and antenna gains.

3.2 A better insight into MIMO channels

Obviously, the gains that MIMO systems can deliver strongly depend on the characteristics of the radio environment. During the ACTS SUNBEAM [2] and the IST METRA [1] projects, extensive measurement campaigns were performed in a variety of environments, outdoor-to-outdoor (macrocell), outdoor-to-indoor (microcell) and indoor-to-indoor (picocell). A subset of key parameters (correlations matrices, Doppler spectrum) was extracted from these measurements to be fed in the stochastic MIMO channel model proposed by METRA. This stochastic model was experimentally validated by comparing measured data to the outcome of simulations.

The purpose of the characterisation work in I-METRA has been to go deeper into the exploitation of the measurement data collected during SUNBEAM and METRA, in order to get a better insight in the properties of MIMO radio channels. This insight has been gained through large-scale post-processing of the measurement data. It has led to the study of the influence of a large set of parameters and contexts, such as correlation, polarization, directional information, power imbalance and presence of a Line-of-Sight (LOS) component.

Additionally, in parallel to this characterization, the MIMO channel model proposed by METRA has evolved in two ways. On the one hand, it has been modified so as to embed the findings of the characterization activities, mainly the impact of power imbalance and polarization diversity. On the other hand, it has been maintained inline with the evolution of standardization in 3GPP.

³ WCDMA: Wideband Code Division Multiple Access

3.3 Outline of the Deliverable

Section 4 presents the technical as well as the theoretical background on the efficiency of the MIMO system compared to the SISO system. The eigenvalues are presented as a quantitative approach to the parallel subchannelling concept along with capacity formula derived for the MIMO technology. Definitions of correlation coefficient and Branch Power Ratio (BPR) are presented. Finally, a glossary of the terminology used in this document is provided.

Section 5 addresses the characterization of the radio channel. This section presents the analysis of the measured data with respect to SISO and SIMO antenna topologies in order to understand the propagation properties of the radio channel. It includes the study of the statistical distribution in terms of the Ricean *K-factor* and a characterisation of the direction of arrival (DoA). A detailed analysis of the power correlation coefficient is performed so that the performance of the MIMO technology developed later in the deliverable can be explained. Finally, several measured paths are selected and their properties are listed so that they can be used as reference scenarios in the rest of the document.

Section 6 describes the update performed on the IST METRA MIMO radio channel model [13] with emphasis on its empirical validation of the polarization domain. Also results of the validation of the model are presented in the spatial domain. The validation was based on the comparison between measured and simulated eigenvalues; the simulated results are being based on the characterisation of the measured environment.

Section 7 introduces the MATLAB[®] implementation of the MIMO channel model initially proposed by METRA and updated during I-METRA according to the findings of the characterization on the one hand, and the evolution of 3GPP standardization on the other hand. The package enables its user to derive correlation coefficients for linear arrays in a variety of scenarios. These coefficients can later be used in the actual channel model to simulate the corresponding MIMO channel. The limitations of the current version of the implementation are then discussed. Since the package is distributed as a freeware, the distribution terms and the status of the diffusion so far are also addressed in Section 7.

Section 8 provides theoretical Shannon capacity results, where two power allocation strategies are compared, for different types of environments, using different diversity techniques and antenna setups. The impact of the BPR at the MEAs on the MIMO technology performance is also addressed. Conclusions and recommendations are presented assuming a single-user scenario.

Finally, Section 9 presents a summary of the concluding remarks made in the previous sections.

4 GENERAL BACKGROUND INFORMATION

4.1 Introduction

The purpose of this section is to provide a basic understanding of the MIMO technology, necessary for the reading of the deliverable, with a special emphasis on antenna array and digital signal processing. At first, a general description of the MIMO structure is given. The concept of parallel subchannelling is then introduced by mean of eigenanalysis, followed by its engineering interpretation. The antenna and diversity gains are also discussed in the context of MIMO technology.

The major motivation for the increasing interest in the MIMO technology, i.e., the capacity aspect, is discussed versus the capacity offered by conventional SISO technologies. This introduces two different power allocation schemes; the water-filling and the uniform power allocation strategy.

The correlation coefficient, which has a major influence in relation to the MIMO technology, is also defined in this section; it is used extensively throughout the document. Another important aspect to consider in the MIMO technology is the BPR thereby its definition in this section.

Finally a mini-glossary gathering the different MIMO propagation terminologies used in this deliverable is presented.

4.2 General MIMO Structure

The MIMO concept is defined, throughout this deliverable, as a radio link with M elements at the BS and N elements at the mobile station (MS) as pictured in Figure 1. For uplink the Tx is at the MS and the Rx at the BS while for downlink, the roles are reversed. In this document, the actual role (Tx/Rx) of the MS and the BS is not important with regard to the conclusion made on the MIMO technology.

The term *element* is used instead of *antenna* to avoid potential confusion when dealing with polarization diversity since sometimes an antenna can be dual polarized with two elements.

The received signal vector $\mathbf{y}(t)$ at the BS antenna array is denoted by

$$\mathbf{y}(t) = [y_1(t), y_2(t), \dots, y_M(t)]^T, \quad (4.1)$$

where $y_m(t)$ is the signal at the m th antenna element and $[\cdot]^T$ denotes the transpose operation. Similarly, the transmitted signals at the MS, $s_n(t)$, define the vector $\mathbf{s}(t)$

$$\mathbf{s}(t) = [s_1(t), s_2(t), \dots, s_N(t)]^T, \quad (4.2)$$

The vectors $\mathbf{y}(t)$ and $\mathbf{s}(t)$ are related by the following expression

$$\mathbf{y}(t) = \mathbf{H}(t)\mathbf{s}(t) + \mathbf{n}(t) \quad (4.3)$$

where $\mathbf{n}(t)$ is additive white Gaussian noise and $\mathbf{H}(t) \in C^{M \times N}$ is the instantaneous narrowband (NB) MIMO radio channel matrix. $\mathbf{H}(t)$ describes the connections between the MS and the BS and can be expressed as

$$\mathbf{H}(t) = \begin{bmatrix} \alpha_{11}(t) & \alpha_{12}(t) & \cdots & \alpha_{1N}(t) \\ \alpha_{21}(t) & \alpha_{22}(t) & \cdots & \alpha_{2N}(t) \\ \vdots & \vdots & \ddots & \vdots \\ \alpha_{M1}(t) & \alpha_{M2}(t) & \cdots & \alpha_{MN}(t) \end{bmatrix} \quad (4.4)$$

where $\alpha_{mn}(t)$ is the complex NB transmission coefficient from element n at the MS to element m at the BS.

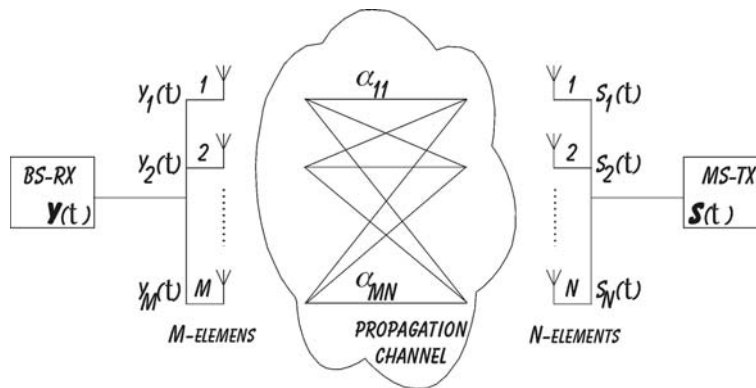


Figure 1. Two antenna arrays in a scattering environment. Representation of an uplink situation.

The term “instantaneous” refers to a snap-shot of the radio propagation channel. In the context of mobile measurement, one snap-shot is equivalent to one sample of the recorded multipath in time (or distance). In the rest of the deliverable, in order to keep the reading simple, the explicit time dependency (t) of $\mathbf{H}(t)$ and $\alpha_{mn}(t)$ is dropped.

4.3 The Eigenanalysis Method and Interpretation

The motivation for deploying MIMO technology in wireless systems is the possibility to achieve orthogonal subchannels between the two ends of the path in a rich scattering environment and subsequently to increase the offered capacity. The concept of orthogonality emphasizes the strength of the MIMO system since it indicates that these

multiple channels are independent from each other. The MIMO technology is also beneficial in increasing the antenna gain and in providing combined Tx/Rx diversity.

Mathematically, the number of independent subchannels between two terminals can be estimated by using the singular value decomposition (SVD) of the matrix \mathbf{H} or the eigenvalue decomposition (EVD) [14] of the instantaneous correlation matrix \mathbf{R} defined as

$$\mathbf{R} = \mathbf{H}\mathbf{H}^H \text{ or } \mathbf{R} = \mathbf{H}^H \mathbf{H} \quad (4.5)$$

where $[\cdot]^H$ represents Hermitian transposition, i.e. the transpose conjugate.

The derivation of the parallel independent channels is summarized below where \mathbf{U} and \mathbf{V} are unitary matrices, $\mathbf{\Sigma}$ and $\mathbf{\Gamma}$ are diagonal matrices and \mathbf{u} and \mathbf{v} are the left and right singular vectors, respectively. On the other hand, K is defined in relation (4.8). There is an important relationship between the SVD of \mathbf{H} and the EVD of \mathbf{R} such that $\sigma_k^2 = \gamma_k$ where σ_k is the k th singular value and γ_k is the k th eigenvalue. Γ_{ij} denotes the elements of the matrix $\mathbf{\Gamma}$.

| SVD | EVD |
|---|--|
| $\mathbf{H} = \mathbf{U}\mathbf{\Sigma}\mathbf{V}^H$ where $\mathbf{\Sigma} = \text{diag}(\sigma_1, \dots, \sigma_K)$ $\sigma_1 \geq \sigma_2 \geq \dots \geq \sigma_K \geq 0$ with | $\mathbf{H}\mathbf{H}^H = \mathbf{U}\mathbf{\Gamma}\mathbf{U}^H \text{ or } \mathbf{H}^H \mathbf{H} = \mathbf{V}\mathbf{\Gamma}\mathbf{V}^H$ $\Gamma_{ij} = \Sigma_{ij}^2$ where $\mathbf{\Gamma} = \text{diag}(\gamma_1, \dots, \gamma_K)$ $\gamma_1 \geq \gamma_2 \geq \dots \geq \gamma_K \geq 0$ with |
| $\mathbf{U} = [\mathbf{u}_1, \dots, \mathbf{u}_M] \in \mathbf{C}^{M \times M}$ $\mathbf{V} = [\mathbf{v}_1, \dots, \mathbf{v}_N] \in \mathbf{C}^{N \times N}$ | |

In the rest of the deliverable, the normalized k th eigenvalue λ_k is used instead of γ_k . Unless otherwise mentioned, the normalization is made with respect to the mean power $|\alpha_{mn}|^2$ between all possible pairs of MS-BS elements so that λ_k is defined as

$$\lambda_k = \frac{\gamma_k}{\mathbf{E} \left[\frac{1}{MN} \sum_{m=1}^M \sum_{n=1}^N |\alpha_{mn}|^2 \right]} \quad (4.6)$$

where $\mathbf{E}[\cdot]$ denotes the expectation over time (or distance). In order to keep the reading simple, the explicit term *normalized* is dropped.

Irrespective of the numerical method used to perform the analysis, a channel matrix \mathbf{H} may offer K parallel subchannels with different power gains, λ_k , where

$$K = \text{Rank}(\mathbf{R}) \leq \min(M, N) , \quad (4.7)$$

and the functions $\text{Rank}(\cdot)$ and $\min(\cdot)$ return the rank of a matrix and the minimum value of the arguments, respectively [14].

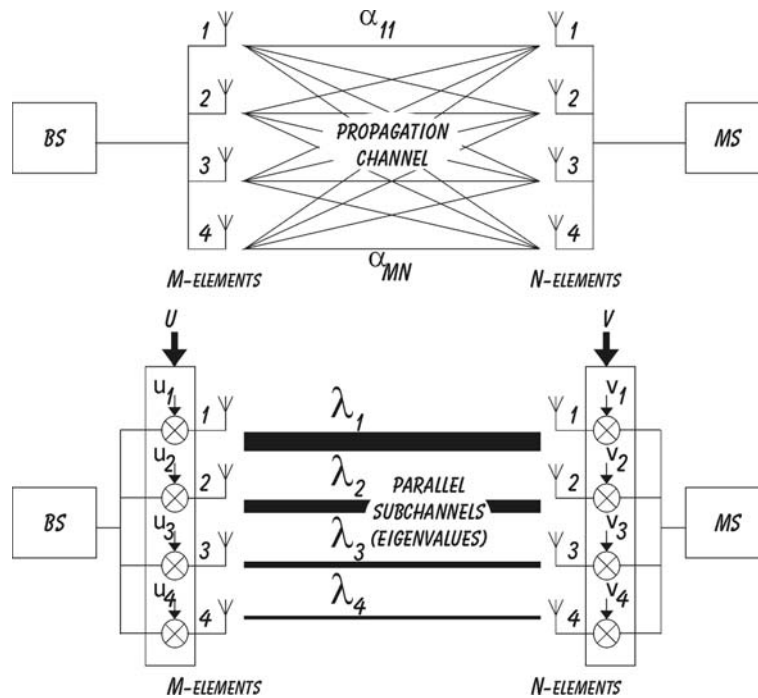


Figure 2: Illustration of parallel subchannels for a 4x4 MIMO MEA topology

In engineering terms, \mathbf{u} and \mathbf{v} are also referred to as the weight vectors while the k th eigenvalue can be interpreted as the power gain of the k th orthogonal subchannel [14]. This is illustrated in Figure 2 for a 4x4 MIMO antenna topology.

In such a configuration, $MN=16$ radio links, α_{mn} , are created, but only 4 orthogonal subchannels with power gain λ_1 to λ_4 are available. The difference in the thickness of the lines emphasizes the difference in gain of the parallel subchannels so that

$$\lambda_1 \geq \lambda_2 \geq \dots \geq \lambda_K \geq 0 . \quad (4.8)$$

To get the weight vectors, it is numerically more convenient to use the SVD of \mathbf{H} while to obtain the eigenvalue it is easier to use the EVD. The EVD technique is the optimal way to extract the power gain of the MIMO subchannels. However, if this technique is to be optimal in a practical system implementation, the proper unitary matrix \mathbf{U} and \mathbf{V} must be applied at the respective ends of the link. Consequently, the EVD method is only useful when the channel is known, i.e., when the information of the radio channel is

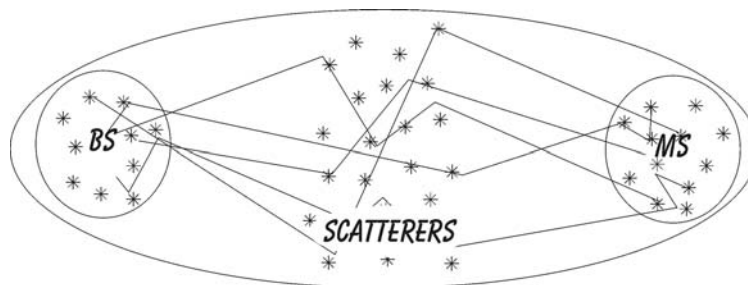
available at both the Tx and the Rx; a situation which can be assumed reasonable for time division duplex (TDD) systems while for frequency division duplex (FDD) systems significant feedback information is required.

4.4 The MIMO Propagation Scenarios

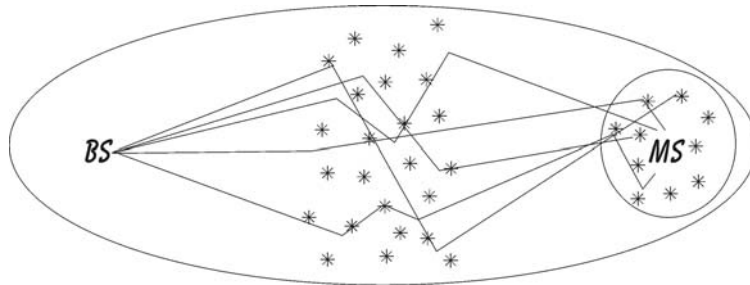
This section presents the different MIMO propagation scenarios which have been extensively studied to date in the MIMO literature. Before enumerating them, the notion of angular dispersive channels is needed at this stage of the deliverable [22]. The angular power density distribution of the environment, i.e., the power at each angle of arrival, fully describes the angular spreading of the signal. This is also often referred to as the Power Azimuth Spectrum (PAS). It is obtained as the Fourier transform of the spatial correlation function [27] [28]. The Azimuth Spread (AS) is defined as the root second central moment of the PAS [7]. The PAS is closely related to the spatial correlation at the MEA, i.e., depending of the spatial separation between the elements of the MEA, a low AS is equivalent to a high spatial correlation coefficient and vice versa. Expressions of the spatial correlation function have been derived in the literature assuming that the PAS follows a cosine raised to an even integer [23], a Gaussian function [24], a uniform function [25], and a Laplacean function [26].

Three MIMO scenarios, each exhibiting a different propagation characteristic, are listed below:

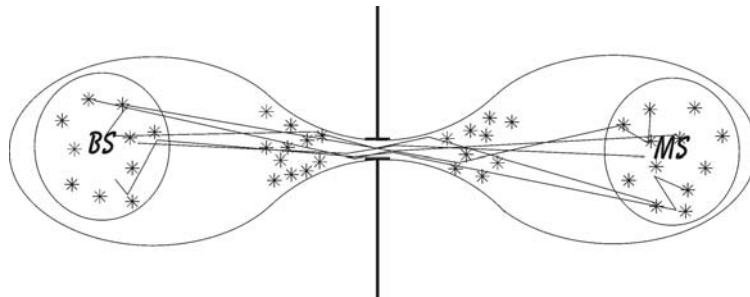
- *Uncorrelated Scenario.* In a rich scattering environment, the elements of \mathbf{H} are fully decorrelated. This corresponds to a full rank scenario where the maximum number eigenvalues is achieved.



- *Correlated scenario.* In a situation with Line-of-Sight (LOS) or low AS at one or both ends of the radio link, the elements of \mathbf{H} exhibit a certain correlation which results in a low rank scenario hence providing a lower number of eigenvalues.



- The pin-hole [20] or keyhole [29] is a scenario where the signals at the MEAs at both the Tx and Rx are decorrelated but the rank of \mathbf{H} is one. This is analogue to a propagation scenario where the radio link is interrupted by an infinite metallic plate with a hole in the middle which is the only way for the signal to pass through, subsequently creating only one subchannel.



Practically, this would be the case when Tx and Rx are on opposite sides of a mountain and the signal can only pass through a tunnel. Another practical interpretation was reported in [17] where a diffraction-induced keyhole could appear. However, as conceived by the same authors, such a scenario may be very rare and difficult to encounter. Moreover, the pin-hole effect has also been considered for situations with large Tx-Rx separation, a situation where the low SNR would anyway degenerate MIMO capacity. In [30] and [16], the concept of keyhole embraces the three scenarios presented above where the first and third scenarios are extreme cases.

4.5 The Antenna and Diversity Gain Aspect

The enhancement in the radio link from the MIMO technology can be expressed in terms of antenna gain, diversity order and throughput performance. As already presented by Andersen in [31], the antenna gain and the diversity order obtained from a MIMO system depend on the scattering environment and especially on the AS at each end of the MIMO radio link. These findings are summarized in Table 1 since they outline MIMO performance very well for different scenarios. In Table 1, the antenna radiation pattern of each element of the MEA is assumed isotropic and the mean gain is the strongest eigenvalue λ_1 .

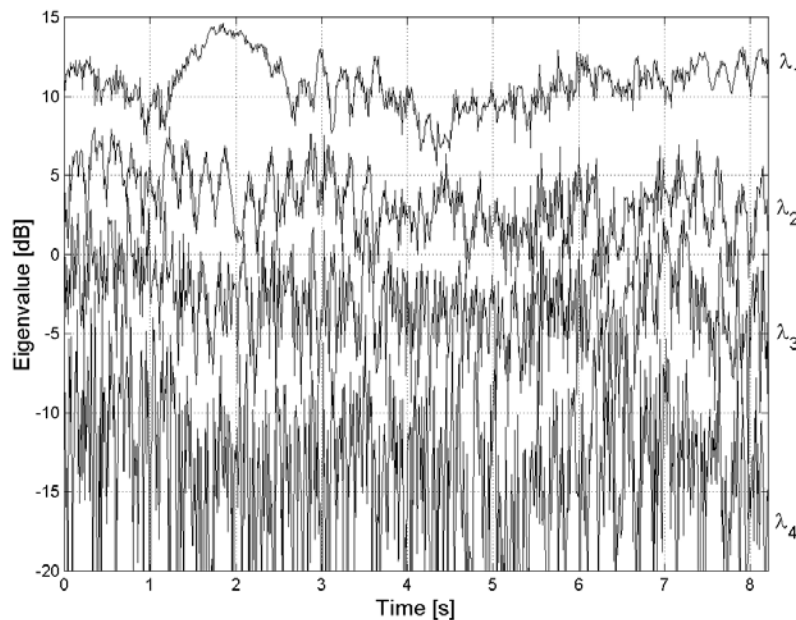
| AS at the MS | AS at the BS | | Scenario | Mean gain | Diversity Order |
|--------------|--------------|---------------|--------------|-------------------------------|-----------------|
| low | low | \Rightarrow | correlated | MN | 1 |
| low | high | \Rightarrow | correlated | MN | M |
| high | low | \Rightarrow | correlated | MN | N |
| high | high | \Rightarrow | decorrelated | $\sim(\sqrt{M} + \sqrt{N})^2$ | MN |

Table 1: Antenna gain and diversity order in a MIMO context for different scenarios (Source: [31])

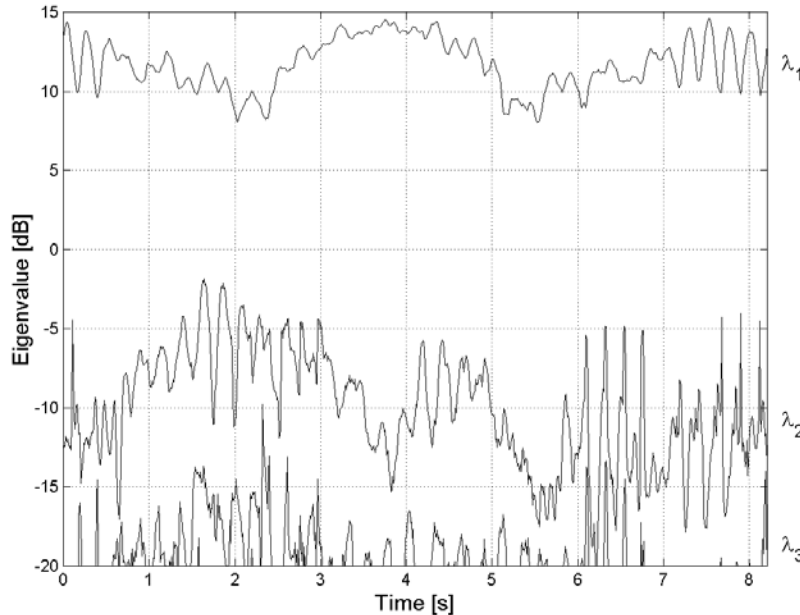
4.5.1 Temporal Illustration of the Eigenvalue

A quantitative description of the MIMO gain performance is the temporal representation of the eigenvalues. Figure 3 (i) presents the behaviour of the eigenvalues derived from a measured 4x4 MIMO setup where the AS is high at both the BS and MS whereas Figure 3 (ii) presents a situation where the AS is low at the BS and high at the MS.

The behaviour of the eigenvalues can be summarized in two items: they fluctuate with time and the strength of each λ_k strongly varies depending on the propagation scenario, i.e., correlated or uncorrelated.



(i) Decorrelated scenario \Rightarrow AS-BS:high-MS:high



(ii) Correlated scenario \Rightarrow AS-BS:low-MS:high

Figure 3: Variation of the eigenvalues over time.

4.5.2 Antenna Gain

Another method to present the eigenvalues is by using their cumulative distribution function (cdf). Throughout the rest of the deliverable, unless otherwise mentioned, the cdf is computed over time. The logarithm of the cdf is shown to be coherent with the original eigenvalue representation reported in [14].

Figure 4 presents the empirical cdf of the normalized eigenvalues compared to a Rayleigh SISO channel. The graphs should read as follows. At the 10%⁴ level a power gain of 19 dB is achieved using MIMO compared to a SISO set-up. The 10% cdf level is often used in this document, since it is a typical measure for system-level performance. The mean value of the strongest eigenvalue of Figure 4 is 11 dB which is in line with the value of 10 dB from [31] for a fully decorrelated 4x4 case.

The cdf representation is also very useful when interpreting the diversity performance in a MIMO system. The steepness of the slope of the cdf reflects the diversity order. The steeper the slope, the less amplitude of the fluctuation in the signal, i.e., the fades due to the multipath are less deep, and therefore a higher degree of diversity is obtained as shown in Figure 4.

⁴ 10% is equivalent to $\log_{10}(0.1)=-0.1$

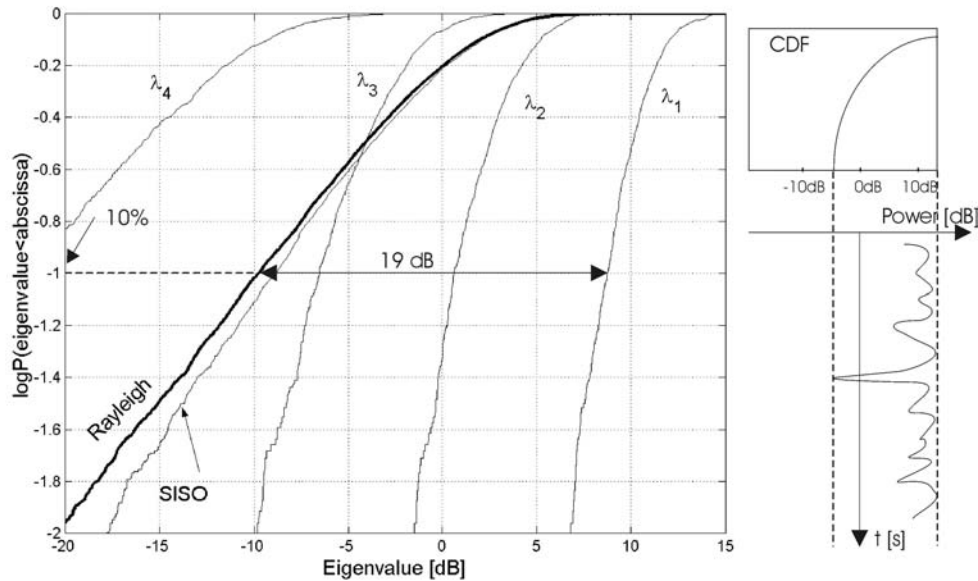


Figure 4: Cdf of the eigenvalues. The slope is an indication of the amplitude of the eigenvalue fluctuations. Same decorrelated scenario presented in Figure 3 (i)

4.5.3 Diversity Gain

Figure 5 illustrates the improvement in antenna gain and diversity order from a measured MIMO system for a correlated scenario, i.e., low AS at the BS and a high AS at the MS. Three different $M \times N$ antenna set-ups are compared: 1×1 , 1×4 and 4×1 . Recall the following notation:

$$\boxed{\text{BS} \rightarrow M \times N \leftarrow \text{MS}}$$

A simulated Rayleigh curve is plotted and compared to the measured 1×1 radio link suggesting that the 1×1 measured signal is Ricean distributed since its curve is steeper than the Rayleigh curve. Relative to this measured SISO case a gain of 6 dB at 10% level is achieved for a 4×1 set-up. This is the classical gain of $10 \log_{10}(M)$ with $M=4$ at the BS, i.e. no Rx diversity gain is obtained, the slope of the 4×1 is the same as for the 1×1 situation.

However, the slope is steeper for a 1×4 topology, the diversity gain at the MS is added to the array gain, and 9 dB gain is achieved at 10% level. In the 4×1 case, the 4 antenna elements at the BS act as a single high gain antenna while in the 1×4 case the 4 antenna elements at the MS are uncorrelated and therefore they achieve both antenna gain and diversity.

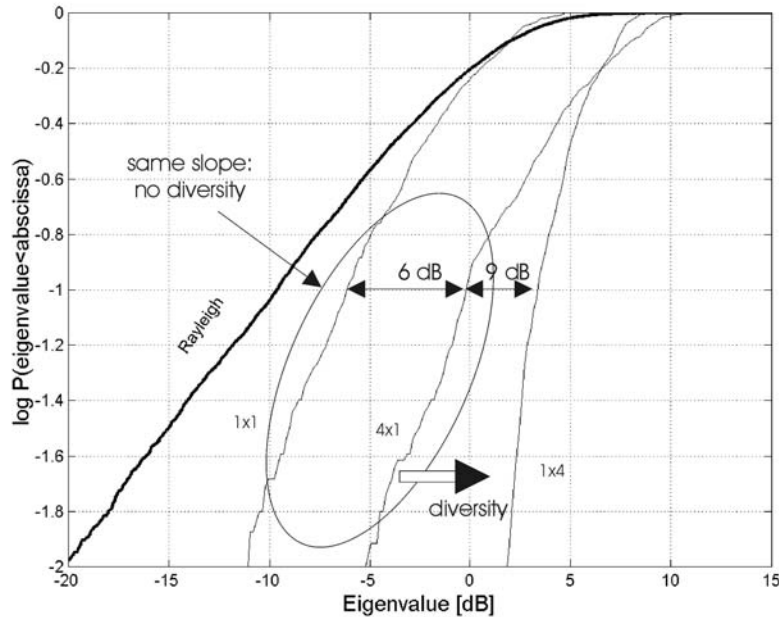


Figure 5: Empirical illustration of the antenna gain and the diversity gain for different spatial antenna array configuration set-ups for the correlated scenario. AS-BS:low-MS:high

4.5.4 The Capacity Aspect

The concept of orthogonal subchannels is now understood. This permits to introduce the capacity concept that MIMO systems can offer compared to a conventional SISO system. This section defines the spectral efficiency of MIMO channels based on the channel capacity as defined in information theory [32] [19]. This is the theoretical maximum amount of information that can be transmitted over a bandwidth limited channel for which error-free transmission is possible in the context of Gaussian channel [33].

In real system implementation, the achievable capacity is limited due to coding, detection, constellation size among others [34], therefore the capacity results presented along the deliverable are to be seen as upper bound values. This study is limited to a single-user scenario where two power allocation strategies are compared: the water-filling and the uniform power allocation strategies. The Shannon's formula for a SISO radio channel is expressed as:

$$C = \log_2(1 + \zeta) , \quad (4.9)$$

where ζ is the signal-to-noise ratio SNR.

For the MIMO technology, Telatar [10] presented the total Shannon's capacity, for uniform power allocation strategy, as

$$C = \log_2 [\det(\mathbf{I} + \mathbf{Q}\mathbf{H}^H \mathbf{H})] \quad (4.10)$$

where \mathbf{I} is the identity matrix, \mathbf{Q} is the signal covariance matrix, $\det(.)$ is the determinant and \log_2 is the logarithm base 2. This formulation is often used by the MIMO community.

Equation (4.10) can be rewritten so as to emphasize the influence of the K parallel subchannels [14] and the total Shannon's capacity is defined as

$$C = \sum_{k=1}^K \log_2 (1 + \zeta_k) \quad (4.11)$$

where ζ_k is the SNR for the k th subchannel and is defined as

$$\zeta_k = \lambda_k \frac{P_k}{\sigma_n^2} \quad (4.12)$$

where P_k is the power assigned to the k th subchannel and σ_n^2 is the noise power. Hence, (4.11) can be rewritten as

$$C = \sum_{k=1}^K \log_2 \left(1 + \lambda_k \frac{P_k}{\sigma_n^2} \right). \quad (4.13)$$

Depending on the power allocation scheme employed, the total transmitted power is distributed in a different manner between subchannels.

When considering the total capacity offered by the MIMO set-up, the total mean SNR per Rx antenna is defined as

$$SNR = \frac{\mathbf{E}[P_{Rx}]}{\sigma_n^2} = \frac{\mathbf{E}[P_{Tx}]}{\sigma_n^2} \quad (4.14)$$

where the time-averaged channel power gain is assumed 0 dB so that there is no loss in average between P_{Tx} and P_{Rx} .

4.5.5 Water-filling Power Allocation

When the channel is known, i.e., when the information of the radio channel is available at the Tx, it is possible to apply the EVD and the k th eigenvalue can be extracted. Given the set of normalized eigenvalues λ_k , the power P_k allocated to each k th subchannel is determined so as to maximize capacity. This solution is known from Gallager's water filling theorem [14] in which each subchannel is filled up to a common level D defined as

$$\frac{1}{\lambda_1} + P_1 = \dots = \frac{1}{\lambda_k} + P_k = D , \quad (4.15)$$

with a constraint on the input power such that

$$\sum_{k=1}^K P_k = P_{Tx} , \quad (4.16)$$

P_{Tx} is the total transmitted power. This means that the subchannel with the highest gain, i.e. the strongest eigenvalue, is allocated the largest fraction of power. In the case where $1/\lambda_k > D$, $P_k = 0$. Given (4.10) this is achievable when \mathbf{Q} is diagonal and the optimal diagonal entries are computed from the water filling theorem.

Hence, (4.11) can be rewritten as

$$C = \sum_{k=1}^K \log_2 \left(1 + \lambda_k \frac{P_k}{\sigma_n^2} \right) , \quad (4.17)$$

where $\overset{(w)}{=}$ denotes the water-filling power allocation scheme.

4.5.6 Uniform Power Allocation Scheme

In the situation where the channel is unknown, i.e., when the information of the radio channel is not available at the Tx, the uniform distribution of the power is the most reasonable power allocation scheme to use. In practice, the total transmitted power P_{Tx} is equally split among the N elements of the array at the Tx [14] and is independent of λ_k so that

$$P_n = \frac{P_{Tx}}{N}, \forall n = 1 \dots N . \quad (4.18)$$

For simplicity in this deliverable, it is assumed [19] that the Tx power is distributed evenly to the subchannels so that given (4.10), \mathbf{Q} is diagonal and its entries are defined as

$$P_n = P_k . \quad (4.19)$$

Therefore, equation (4.11) can be rewritten as

$$C = \sum_{k=1}^K \log_2 \left(1 + \lambda_k \frac{P_n}{\sigma_n^2} \right) \quad (4.20)$$

where $\overset{(u)}{=}$ denotes the uniform power allocation scheme.

4.6 Correlation Definition

Up to now in this report (see pages 17 and 21), the terms correlation or decorrelation have been largely used to emphasize the importance of the correlation properties between MEAs' elements. This section defines the correlation coefficient which is addressed through this work. The basic statistical definition of the correlation coefficient ρ used in this document is given by

$$\rho = \langle a, b \rangle = \frac{\mathbf{E}[ab^*] - \mathbf{E}[a]\mathbf{E}[b^*]}{\sqrt{(\mathbf{E}[|a|^2] - |\mathbf{E}[a]|^2)(\mathbf{E}[|b|^2] - |\mathbf{E}[b]|^2)}} \quad (4.21)$$

where $*$ and $\langle \cdot, \cdot \rangle$ are the complex conjugate and the correlation coefficient operators. Depending on the nature of both a and b , three different correlation coefficients can be defined: complex, envelope or power. Consider two complex variables x and y .

➤ Complex, $a=x$ and $b=y$, ρ_{cplx} :

$$\rho_{cplx} = \langle x, y \rangle \quad (4.22)$$

➤ Envelope, $a=|x|$ and $b=|y|$, ρ_{env} :

$$\rho_{env} = \langle |x|, |y| \rangle \quad (4.23)$$

➤ Power, $a=|x|^2$ and $b=|y|^2$, ρ_{pow} :

$$\rho_{pow} = \langle |x|^2, |y|^2 \rangle \quad (4.24)$$

In the context of modelling, the complex correlation coefficient carries the full information (amplitude and phase) required to model properly the radio channel; this explains why the complex correlation coefficient is used in the upgraded version of the MIMO radio channel modelling in Section 6.

The envelope and the power correlation coefficients, however, have a clearer engineering interpretation than the complex correlation coefficient. In the 1970-80s, the analysis of the correlation was often performed on an envelope correlation basis [23] [35] [24]. This choice was motivated by the limitations of the measurement system itself, since it could only provide the amplitude or the power of the measured signal and not its phase. Furthermore, engineers also found it easier to handle the envelope or power correlation coefficient rather than the complex correlation coefficient as reported in [36] since typical

values of $\rho_{pow} \leq 0.7$ [37] or $\rho_{pow} \leq 0.5$ [37] are sufficient to achieve significant diversity gain. Nevertheless, the concept of the complex correlation coefficient was already addressed theoretically in the late 1950s [39] and early 1960s [40]. It is shown in these references that the two definitions (4.22) and (4.24) are linked to each other by the relationship

$$\rho_{pow} = |\rho_{cplx}|^2, \quad (4.25)$$

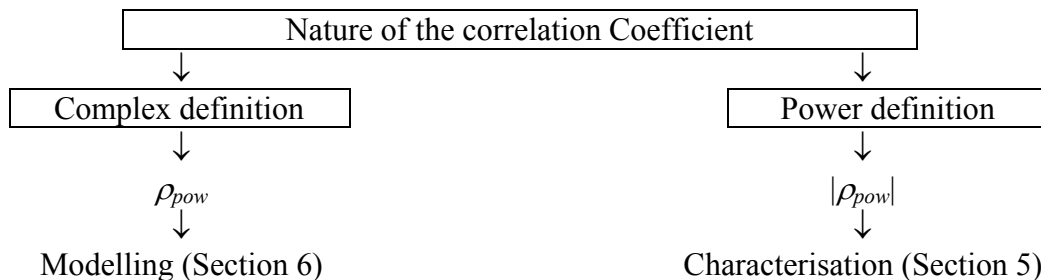
for Rayleigh distributed signals [40] and

$$\rho_{pow} = \frac{|\rho_{cplx}|^2 + 2 \operatorname{Re}\{\rho_{cplx}\} \sqrt{K_a K_b}}{\sqrt{(2K_a + 1)(2K_b + 1)}} \quad (4.26)$$

for Ricean distributed signals [39] where $K_{a,b}$ are the *K-factors* of the complex signals a and b , and $\operatorname{Re}\{\cdot\}$ returns the real part of the complex argument. The definition in (4.24) for ρ_{pow} is restricted to the interval $[-1,1]$ while ρ_{pow} in (4.25) is confined to $[0,1]$. This discrepancy can be alleviated considering the fact that a correlation value of -1 is equivalent to a signal being totally correlated with another but shifted by π , like for a sine wave; for simplicity's sake in handling the measured data and comparing the correlation results with published work, the correlation coefficient analysis presented in Section 5 is based on the absolute power definition $|\rho_{pow}|$.

Studies on the envelope and power correlation coefficient corrupted by additive white Gaussian noise [41] indicate that for signals exhibiting SNR lower than 20 dB, the correlation value is negatively biased and a corrective factor is needed. The magnitude of the corrective factor is 0.05 when $10 \text{ dB} \leq \text{SNR} \leq 20 \text{ dB}$. The need for correction was not necessary in this study, since the majority of the measured SNR achieved during the measurement campaigns were higher than 20 dB.

The difference in the nature of the correlation coefficient studied in different sections of this deliverable due to their applications is summarized below.



4.7 Branch Power Ratio

An important parameter to take into account when implementing the MIMO technology is the BPR. In this deliverable the BPR is defined as the ratio between the powers P_n on the n th element's branches of the MEA.

$$BPR_{ij} = \frac{P_i}{P_j}, \quad (4.27)$$

Therefore an equal, or balanced, mean BPR, \overline{BPR} , indicates that the average power on each branch is equal which can be written as

$$\overline{P}_1 = \overline{P}_2 = \dots = \overline{P}_N, \quad (4.28)$$

$$\overline{BPR}_{ij} = \frac{\overline{P}_i}{\overline{P}_j} \cong 0 \text{ dB}. \quad (4.29)$$

In this document, a $\overline{BPR} = 0.22 \text{ dB}$ is considered equal. An unequal or unbalanced \overline{BPR} means that the

$$\overline{P}_1 \neq \overline{P}_2 \neq \dots \neq \overline{P}_N, \quad (4.30)$$

$$\overline{BPR} \ll 0 \text{ dB} \quad (4.31)$$

Based on measured data, it is shown in this deliverable that even though the correlation coefficient values are very low ($\rho_{pow} \leq 0.2$), the MIMO technology is not optimal when the mean BPR is unequal as shown in Section 8. Unless otherwise mentioned all the MIMO results are presented considering an equal mean BPR.

4.8 Mini-glossary of MIMO Terminology

This section presents a mini-glossary of the MIMO propagation terminology applied in the rest of the deliverable along with an illustration in Figure 6.

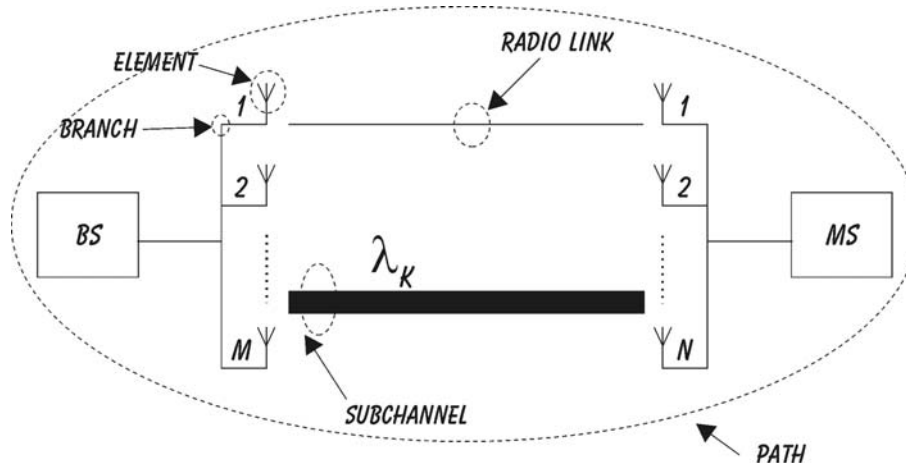


Figure 6: Illustration of the MIMO propagation terminology applied in the rest of the deliverable

- **Radio link** A radio link is defined as the radio connection between two single elements of the two MEAs, also referred as α_{mn} .
- **Path** A path is defined as the radio connection between the two MEAs of a MIMO configuration. In the case of measurement campaign, this is also equivalent to the pair (MS,BS) of a measurement location. In a path there are MN radio links.
- **Subchannel** A subchannel, i.e. the eigenvalue, is equivalent to a virtual link between the two MEAs.
- **Branch** A branch is the output of an element.

4.9 Summary and Interim Conclusion

This section presented the necessary background to fully understand the MIMO antenna technology. A general description of the MIMO structure, i.e. M antenna elements at the BS and N antenna elements at the MS, was given. The concept of parallel subchannelling was introduced by mean of eigenanalysis. Three MIMO propagation scenarios are identified: the uncorrelated scenario, the correlated scenario and the pin-hole effect.

The antenna and diversity gains in the context of MIMO technology was discussed. The normalized eigenvalues λ_k represent the power gain of the k th parallel subchannel. The antenna gain of the MIMO system is the strongest eigenvalue λ_i , and the slope of the cdf of the eigenvalues illustrates the degree of diversity in the MIMO system.

The major motivating factor in the MIMO technology is the high spectral efficiency offered compare to the conventional SISO technology. The theoretical capacity performance of MIMO technology was defined from the generalised Shannon equation and was shown to be related to the parallel subchannels. Definitions of two different

power allocation schemes were presented, the water-filling and the uniform power allocation strategies.

The correlation coefficient, which has a major influence in relation to MIMO technology and which is used extensively throughout the deliverable, was also defined in this section. In the context of modelling, the complex correlation coefficient is more suited and therefore used in Section 6, whereas the power correlation coefficient, providing a clearer engineering interpretation of the propagation analysis, is used in Section 5. The BPR which has also a major influence in relation to the performance of the MIMO technology has been defined in this section.

Finally a mini-glossary has been presented to gather the different MIMO propagation terminology used in this deliverable.

5 CHARACTERISATION OF THE RADIO CHANNEL

The analysis of the measured data has been divided into two parts. The first part is presented in this section and deals with the propagation characteristics of the measured environment with respect to SISO and SIMO antenna topologies. The second part of the analysis is presented in Section 7, where MIMO system performance in terms of theoretical Shannon capacity is addressed.

This section is dedicated to the extraction of channel parameters from the measured data. The channel parameters are obtained from the NB information of the WB measured data. It includes the study of the statistical distribution in terms of the Ricean *K-factor* and a characterisation of the Direction of Arrival (DoA). The two informations are used together to categorise the environment investigated in terms of their LOS/NLOS and low/high AS characteristics. Conclusions on the angular distribution of the wave in indoor environments are drawn based on the DoA analysis applied to the measured data. A cluster type of distribution rather than a uniform one is shown. Furthermore, the DoA analysis allows drawing conclusions on whether the WSS requirement holds for the measured data. It is shown that some measurement paths do not hold such a requirement.

Study of the power correlation coefficient is addressed based on measured data for different cell environments, i.e., picocell and microcell, and different antenna configurations. The analysis considers the spatial correlation coefficient, the polarization correlation coefficient, the joint spatial-polarization correlation coefficient, and the joint pattern-spatial-polarization correlation coefficient.

Finally, a summary of some measurement paths is proposed at the end of this section. They are selected for their propagation characteristics, and are specifically used in the rest of this deliverable as examples of the performance of the MIMO technology.

5.1 From Wideband to Narrowband

The measurement campaign provided MIMO sounding radio channel data. A simple algorithm called CLEAN, originally developed for processing astronomical images [43] and recently used to estimate the dispersion of the radio channel [44] [45] was selected to extract the high resolution complex information from the WB measured data. This algorithm performs fairly well when the temporal dispersion is sufficiently large compared to the resolution of the measurement system. In large microcells, i.e., the microcell investigated during the SUNBEAM project, the CLEAN algorithm would be efficient. However, for picocells or microcells of smaller size, like the one investigated as part of the METRA project, the resolution of the measurement signal was too low to identify any time dispersion in the radio communication channel without error from the CLEAN algorithm.

The RMS (Root Mean Square) delay spread, σ , is used in this section to quantify the low time dispersion of the indoor channel. The RMS delay spread of the channel $\sigma_{channel}$, can

be extracted from the relationship which links the RMS delay spread of the measurement system $\sigma_{system} = 0.0946 \mu s$ derived from the *back-to-back* measured IR, and the recorded $\sigma_{measured}$. This relation is based on the variance subtraction operation

$$\sigma_{channel}^2 = \sigma_{measured}^2 - \sigma_{system}^2$$

and is applicable when assuming decorrelated scatterers [46], [36] or non coherent voltage addition [47].

The cdf of $\sigma_{channel}$ was computed for all the measured paths and is presented in Figure 7. The sampling resolution of the measurement system was $0.122 \mu s$, whereas the excess delay resolution was $1.5 \text{ chip} = 0.366 \mu s$ so no significance can be attributed to details between 0 and $0.366 \mu s$. However, it illustrates that for 98% of the paths in the picocell environments, $\sigma_{channel}$ is less than $0.366 \mu s$. This is in good agreement with [46] [48] among others for indoor scenarios. For the microcell environment it is observed that only 25% of the paths provide larger time dispersion. Based on these results, it was decided to use the NB information in the subsequent analysis.

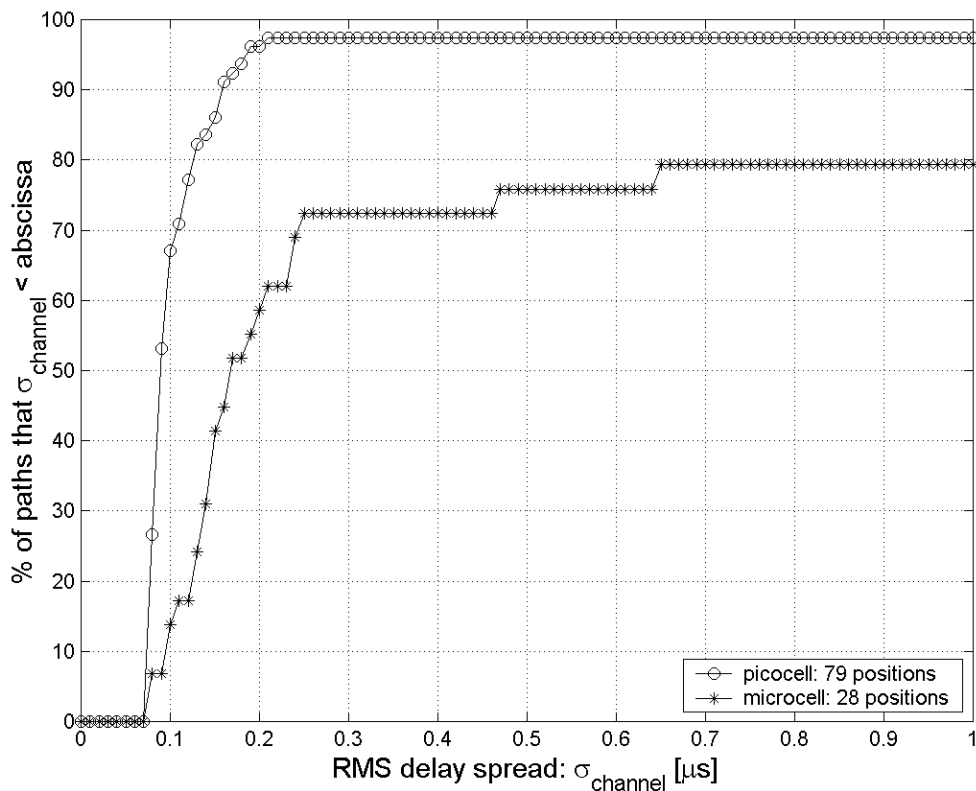


Figure 7: cdf of $\sigma_{channel}$ for picocell and microcell environments.

The complex NB information, $\alpha_{mn}(t)$, is computed from the measured WB signal $\alpha_{mn}^{wb}(t, \tau_l)$ where t and τ are time and delay respectively. This operation is equivalent to selecting one specific frequency component in the frequency domain, i.e., $f=0$ at baseband, of the WB measured signals [36] and so that

$$\alpha_{mn}(t) = \frac{1}{L} \sum_{l=1}^L \alpha_{mn}^{wb}(t, \tau_l)$$

where $1/L$ is used as a scaling factor. The main motivation for performing this operation is that the limited excess delay resolution (1.5 chip) did not enable to resolve multipath components in typical indoor environments. For the computation of $\alpha_{mn}(t)$, a square window is applied on the $\alpha_{mn}^{wb}(t, \tau_l)$, meaning that only a part of the WB measured data is used in the average process, hence filtering out part of the noise.

5.2 Statistical Distribution of the NB Signal

For a more comprehensive characterization of the radio channel based on the measured data, it is necessary to know the statistical nature, i.e., the Ricean *K-factor*, of the post-processed measured NB signal; the result of this analysis is useful for the categorization of the paths when the correlation coefficient is investigated.

Often radio paths are categorized as LOS or NLOS. In this deliverable LOS is defined as a path where there is no obstruction between the two ends of the radio path. LOS scenario are often associated with the Rice distribution, since a strong signal component (the actual LOS) and smaller components (the reflected waves) compose such a distribution, while in a Rayleigh distribution, the LOS components disappears and only the reflected waves are existent.

For the microcell environments, the concept of LOS is inadequate since the outdoor wall of a building lies between the two ends of the radio path. However the existence of a strong direct component in such a scenario would still results in a Rice distribution. This strong direct component would be the result of the energy being narrow beamed due to a low AS at one or both ends of the paths. Subsequently, the value of the *K-factor* should rather be attributed to the spatial dispersion of the waves; the AS was used as a reference to interpret the behaviour of the *K-factor*.

A classification of the interpretation of the estimated *K-factor* is shown in Table 2 where environment, size, structure and cell type are dependent parameters.

| Cell type | <i>K-factor</i> | |
|-----------|------------------------------|--------------------------------|
| | $\in [0, 2[$ (Rayleigh-like) | $\in [2, \infty [$ (Rice-like) |
| Picocell | NLOS | LOS |
| Microcell | high AS | low AS (at the BS) |

Table 2: Classification of the *K-factor*.

The method used to estimate the K -factor is based on the work reported in [49]. The analysis considers a 4×4 antenna setup so that the SISO amount of statistics on the received signal is increased by a factor of 16. Equivalently, the K -factor is estimated over a distance of about $188\lambda = 16 \times 11.8\lambda$.

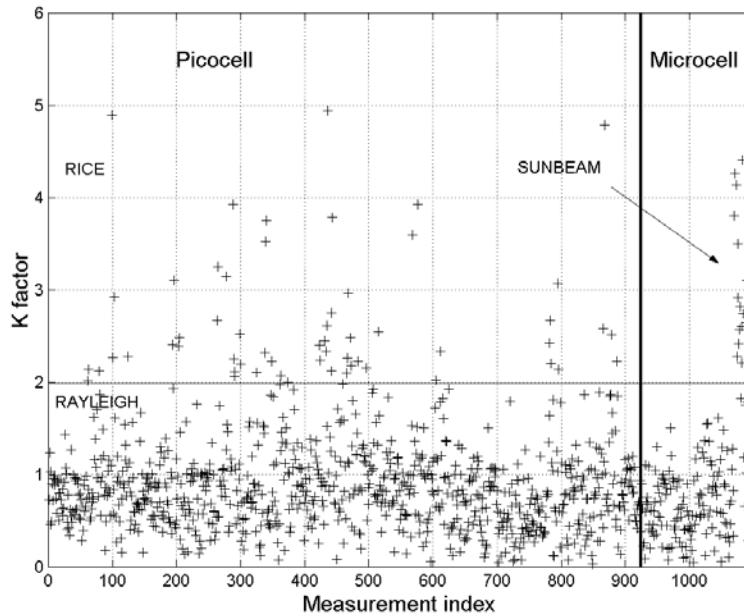


Figure 8: K -factor value for all the picocell and microcell environments for all the transmit and receive antenna configurations.

Figure 8 presents the estimated K -factor including all the picocell and microcell environments and all the transmit and receive antenna configurations. The graph has been divided into two zones: the picocell and the microcell and the estimated K -factor indicates a fluctuation from 0 to 6. It is difficult to set a strict boundary between Rice and Rayleigh distributed signals. The value of 2 is believed to be reasonable considering the uncertainty of the measured data and the inherent errors in the estimation process. Therefore, a low value of the K -factor, i.e., $K < 2$, is regarded to be equivalent to a Rayleigh distributed radio channel while for larger value of K -factor, i.e., $K \geq 2$, the radio channel is said to be Ricean distributed.

For the picocell environments, the majority of the K -factor values are lower than 2, indicating that the signals are Rayleigh distributed for LOS and NLOS indoor scenarios. For the microcell environments, two measurement set-ups with two different element spacings have been used at the BS; therefore, it is preferred to investigate the microcell per measurement set-up. The SUNBEAM project indicates a majority of the scenario being Ricean distributed (Only 2 paths are identified with Rayleigh distributed signals), while for the METRA project, the microcell environment exhibits Rayleigh distributed signals.

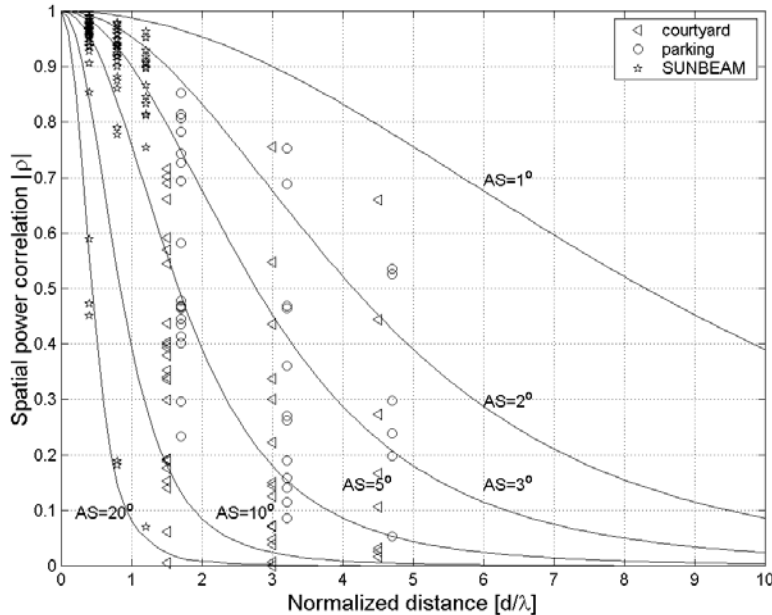


Figure 9: Spatial correlation function assuming Laplacean distribution. Measured spatial correlation coefficients for all the microcells plotted per antenna separation.

Figure 9 presents the spatial power correlation versus the element separation at the MEA for both the SUNBEAM and the METRA measurements. On the same graph, the spatial correlation function assuming a Laplacean PAS function [26] is plotted. The AS is derived by matching the spatial correlation value to the PAS function.

The measurements performed as part of the SUNBEAM project exhibit 14 paths out of 15 with a low AS in the range of 1° to 5° , and one path having a higher AS equal to 20° . Large values of the *K-factor*, i.e., *K-factor* ≥ 2 , were observed for this measurement campaign when comparing with Figure 8.

The two METRA microcell environments indicate higher AS values in Figure 9, with some cases where the spatial power correlation is about 0.8 (for the parking measurement, due to the lower density of scattering), which is in agreement with the fluctuation of the range of the *K-factor* from 0 to 2.

5.3 Analysis of the Direction of Arrival

In addition to the knowledge of the statistical distribution of the radio channel, DoA analyses are performed at the MS. For the specific application of this document, the meaning of arrival in DoA is understood in a large sense and the term departure as Direction of Departure (DoD) could also have been used since the DoA analysis could be performed at only one end of the path. Recall that DoA could not be performed at the BS

since the spacing between the MEA elements was too large. There are several motivations for performing the DoA analysis at the MS:

- The possibility of verifying whether the radio channel satisfies the WSS condition in the investigated indoor environments. The DoA analysis can provide an illustration of the PAS at the MEA in order to test the implicit WSS assumption of the model.
- The nature of the incoming rays in an indoor environment when *indoor-to-indoor* and *outdoor-to-indoor* communication links are considered. Indeed, the results of the DoA analysis would confirm, or not, the usual assumption that for a picocell environment the rays are uniformly distributed in an angle around the MS. It was found in [50] that in an outdoor-to-indoor scenario the main contribution to the signal energy is in the direction of the windows.

DoA analysis has not been performed on any of the measured data collected during the SUNBEAM project due to the measured set-up employed. Only the vertically transmitted scenarios of the METRA measurement campaigns are considered in the DoA analysis.

5.3.1 Geometrical Constraint

There is a large variety of MEA structures used for the DoA estimation. The most common structures are the linear MEA, the square MEA [51], [42], and the circular MEA [52]. A recently proposed antenna structure using a spherical MEA [53] [15] was used to perform 3-D radio channel characterisation at the MS.

5.3.1.1 Far-Field and Spatial Nyquist Criteria

When performing practical measurements, two important constraints have to be considered in DoA analysis: the far-field and the spatial Nyquist criteria.

- The **far-field** [54] distance is to be respected if the received signal has to be assumed as composed of plane waves. This is particularly an issue when considering the measurements made in the small offices since the nearest scatterer is relatively close to the MEA. This constraint limits the size of the effective aperture and consequently the number of effective elements when equidistant separation is implemented.

As a rule of thumb [42] the far-field distance is equivalent to $2D^2/\lambda$ where λ is the wavelength and D is the largest linear dimension of the MEA, i.e., the effective aperture, as shown in Figure 10 for both linear and square MEAs.

- The **spatial Nyquist criteria** is to be considered when sampling the signal in the spatial domain. This is very similar to the sampling process in the time or frequency domain. As shown in [55] among others, the spatial Nyquist criteria is necessary to avoid aliasing and grating lobe effects. The duality, when the MEA elements are isotropic, can be presented as

$$f_0 = 2f_{\max} \leftrightarrow d_0 = \frac{\lambda}{2}$$

where f_0 is the Nyquist criteria with f_{\max} as the highest frequency component in the signal, and d_0 the spatial Nyquist criteria among the MEA elements. This means that the spacing d between the elements of the MEA should be less or equal than half a wavelength ($d \leq d_0$).

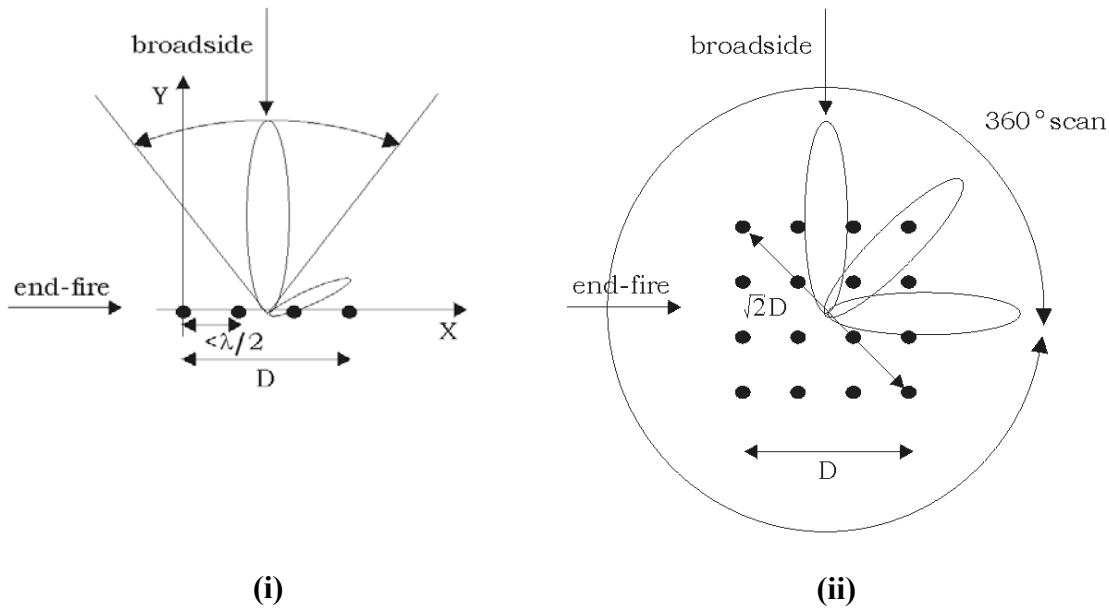


Figure 10: Illustration of the scanning possibilities of the (i) linear MEA and (ii) the square MEA.

5.3.1.2 Square over Linear MEA

In DoA estimation, the scanning range of a linear MEA, see Figure 10, is limited since any *end-fire*⁵ signal cannot be seen by the MEA with the same pattern as it would be if the signal were *broadside*; the radiation pattern gets worse when it is steered from broadside to end-fire therefore a linear MEA can not provide a full 360° scan. To overcome this problem, a synthetic planar square MEA was used. The term planar indicates that the MEA elements are all lying on the same horizontal plane. In the rest of the deliverable, it is simply referred to as the square MEA.

The square MEA configuration allows a full 360° scan in the azimuth plane. Furthermore, equidistant spacing between the antenna elements, i.e., 0.4λ , is selected so that signals

⁵ The term *end-fire* refers to the side of the MEA where the signal is impinging parallel to the MEA while *broadside* refers to the side where the signal is coming perpendicularly to the MEA [56] [42].

coming from the *back* can be distinguished from the *front* when they are either broadside or end-fire which is not the case when the spacing is equal to $\frac{\lambda}{2}$.

5.3.1.3 Spatial Filtering Artefacts

The complete 360° scan is not as trivial as it may appear. The beamwidth of an MEA depends on the effective aperture of the MEA. The beamwidth at half power, i.e., at 3dB, $BW_{[3dB]}$, is generally defined as [60]

$$BW_{[3dB]} = \arcsin\left(\frac{0.886\lambda}{\Omega d}\right)$$

where Ω is the number of linear elements in the MEA along broadside and $d \leq d_0$ is the spacing between the elements in wavelengths. The effective aperture D is defined as

$$D = \Omega d ,$$

meaning that the larger D , the narrower the beamwidth and vice versa.

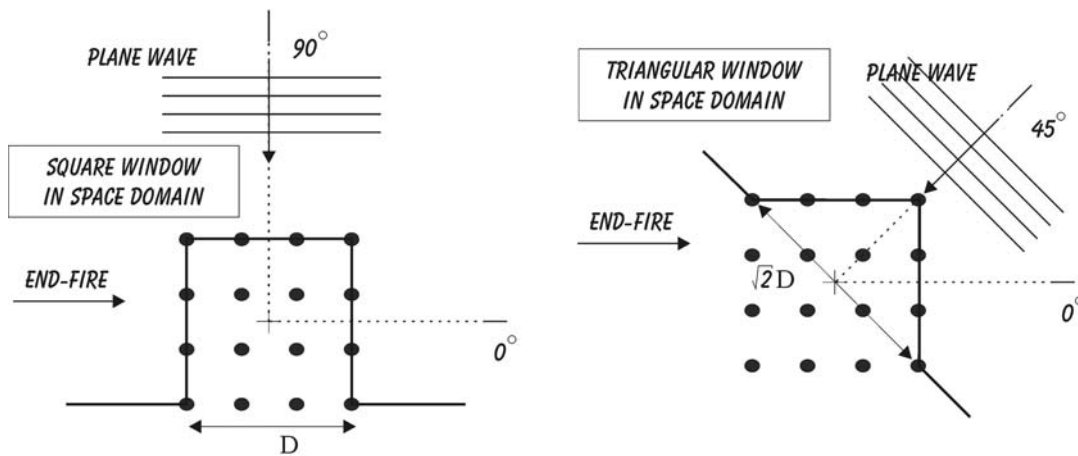


Figure 11: Illustration of the windowing effect of the square MEA in the DoA process.

Figure 11, illustrates that when the signal reaches the square MEA at broadside, or similarly end-side, the effective aperture of the antenna is D but at an incident angle of 45° the effective aperture becomes $\sqrt{2}D$. Consequently, the beamwidth at 45° of the MEA is supposedly narrower than the beamwidth at broadside; this is, however, not the case as explained below.

The windowing effect is a well known phenomenon in the frequency-time domain analysis [57] [58]. In the spatial domain, this effect occurs when using a square MEA as illustrated in Figure 11. At broadside, the measured complex signal is subject to a square

window while when arriving at 45° incident angle, it is subject to a Bartlett-or triangular-window.

The windowing effect is illustrated quantitatively in Figure 12 where the beamwidth of the square window for $\sqrt{2}D$ is narrower than the square window with D , but as soon as the Bartlett window is applied with $\sqrt{2}D$, the beamwidth is similar (within a 1° accuracy) to the beamwidth computed from a square window with D as an effective aperture. So despite a larger effective aperture at 45° incident angle, it is possible to keep the scanning beamwidth constant at about 33° in the whole azimuth plane.

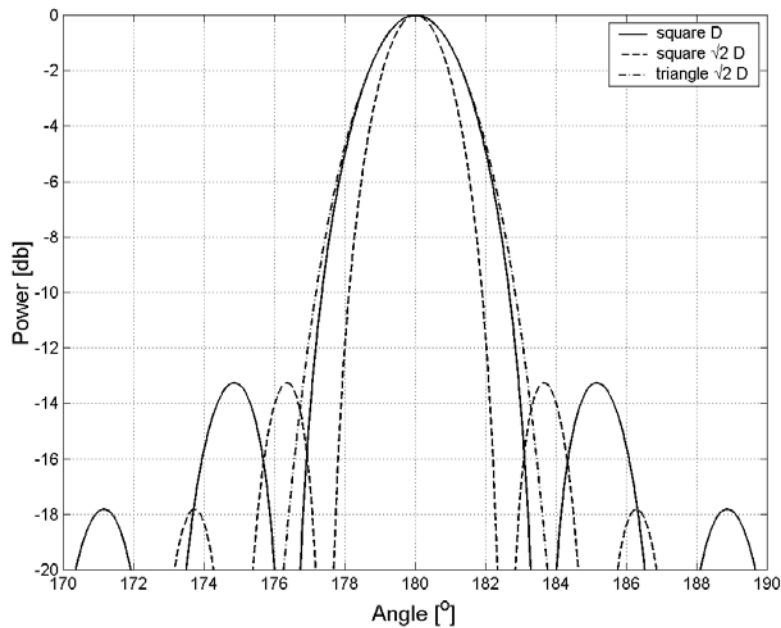


Figure 12: Quantitative illustration of the windowing effect of the square MEA in the DoA process.

The differences between the simulated radiation patterns of a linear MEA and square MEAs are illustrated in Figure 13 for the cases when an incoming wave is incident at 0° (*end-fire*), 35° , 90° (*broadside*) and 240° .

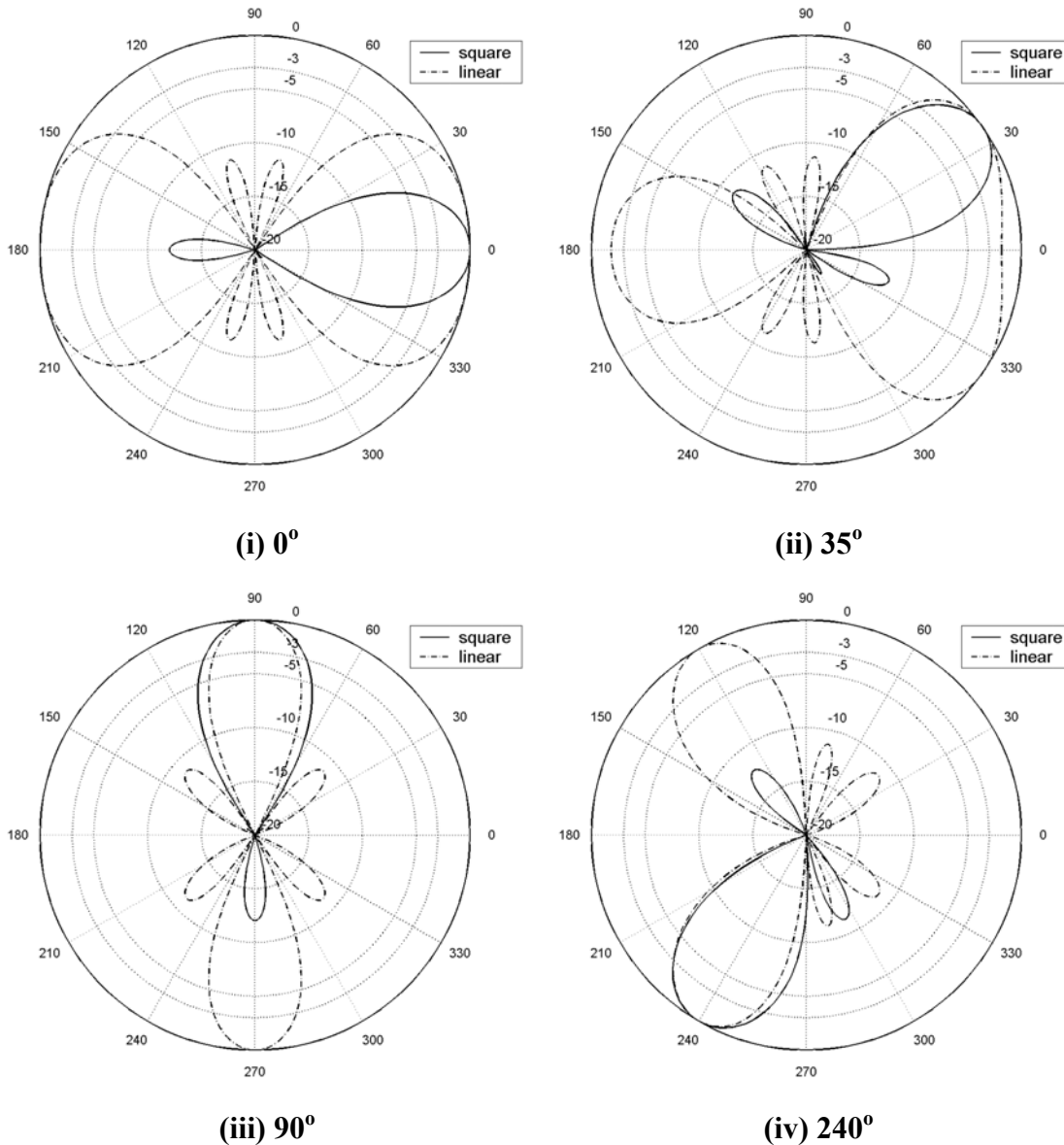


Figure 13: Four examples of simulated scanning possibilities when a ray is incident at 0°, 35°, 90° and 240°.

Figure 13 (i) presents the DoA results from linear and square MEAs when the wave are impinging with an incident angle of 0° which is equivalent to an end-fire situation. This figure indicates that the beam of the square MEA points to the desired direction with a half power beamwidth of 33° whereas the linear MEA does not distinguish whether the wave is coming from 0° or 180°, furthermore the beamwidth is much greater than the square MEA beamwidth.

In the case when the incident wave impinges at 35°, Figure 13 (ii) indicates that the square MEA points to the desired direction with the same beamwidth as before whereas the beam of the linear MEA is totally distorted.

For the 90° situation, i.e., a broadside, the beamwidth of the linear MEA is optimal but it can not distinguish a wave coming from the front (90°) to a wave impinging from the back (270°). The square MEA however still points to the desired direction with the same beamwidth as before.

And finally, for the 240° situation the square MEA still points to the desired direction with a constant beamwidth.

The characteristics of linear and square MEAs are summarized in Table 3.

| Geometrical configuration | Linear MEA | Square MEA | Square MEA |
|--------------------------------|------------------|------------------|------------------|
| d in X | 0.5λ | 0.5λ | 0.4λ |
| d in Y | - | 0.5λ | 0.4λ |
| number of elements | 4 | 16 | 16 |
| Element radiation pattern | omni-directional | omni-directional | omni-directional |
| Beamwidth [3dB] | 26° | 26° | 33° |
| Back-to-front determination | no | no | yes |
| Beam as a function of θ | variable | invariant | invariant |
| Far-field | 4.5λ | 9λ | 5.8λ |
| 360° scan | no | no | yes |

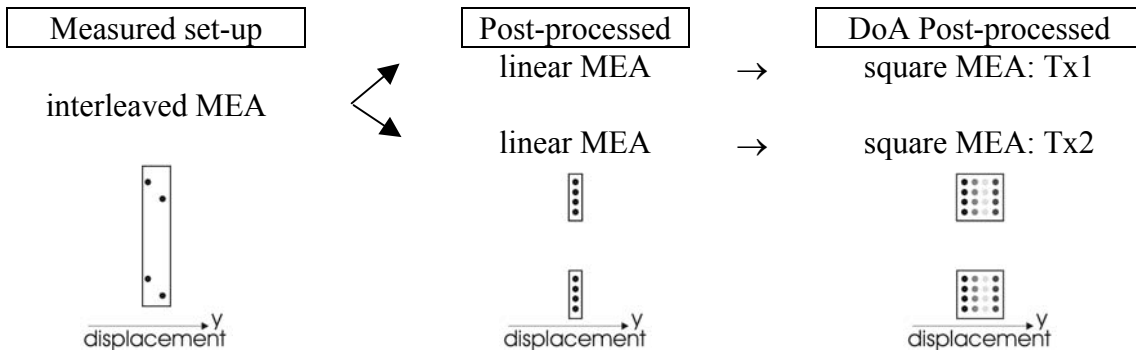
Table 3: Summary of the pros and cons of using linear and square MEAs.

5.3.2 A Conventional Beamforming DoA Algorithm

There is a large volume of literature devoted to the different types of DoA estimation algorithms, [59] [56] among others. The selection of the DoA algorithm is based on [60] where different methods like Fourier method, Capon Estimator, MUSIC algorithm, and Widrow algorithm are compared for the estimation of the angular power spectrum. It was found that the Fourier method (also known as the classical or conventional beamformer) was considered as the best trade-off between resolution, accuracy, and complexity.

Therefore, the Fourier method is selected in this work as a simple tool for the DoA study keeping in mind that the resolution of this technique is limited in the ray arrival angle resolution.

At the MS, the DoA was estimated from the processed NB signal for each measurement path. The procedure to obtain two linear MEAs from the interleaved MEA was presented in the IST METRA deliverable 2 [1]. From these linear MEAs, two square MEAs (separated by 3λ) were created synthetically from the snapshot along the displacement of the slide. For each of the two square MEAs, 8 DoA estimation analyses were produced for each of the 8 elements of the 2 linear MEAS at the BS.



5.3.3 DoA Results Characterisation

This section presents three important results of the DoA analysis. The first results present an example of the characterisation of the spatial nature of the radio channel for a measured environment with respect to the *K-factor* results presented earlier. The last two results give examples of the spatial nature of the radio channel during the measurement with respect to the WSS requirement.

5.3.3.1 Spatial Nature of the Radio Channel

An example of the spatial nature of the radio channel is given in Figure 14, i.e., the small office scenario of novi2 presented in [1]. The DoA analysis results are plotted on polar grids for each measurement path. The results are normalized to their maximum for each path and down limited to -13 dB so that the sidelobe contributions shown in Figure 12 are not considered.

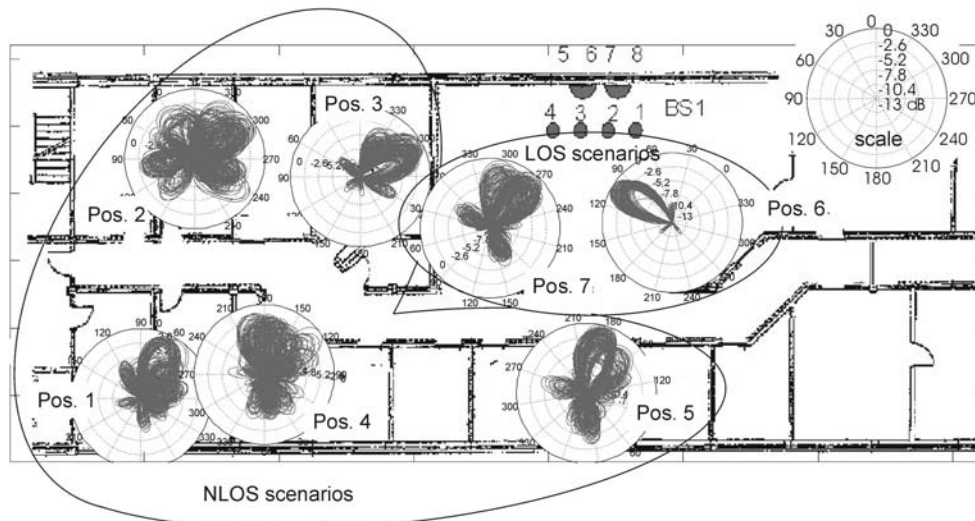


Figure 14: Illustration of the NLOS (Pos. 1 to 5) and LOS (Pos. 6 to 7) classification for novi2, small indoor offices.

At the MS, the first square MEA, Tx1, is considered and at the BS, BS1, one of the vertical dipoles of the MEA is chosen. Considering this example, the assumption of uniformly distributed scatterers does not hold for this indoor-to-indoor radio channel. It appears that in some cases the DoA presents a multi clustered behaviour and therefore, it is difficult to obtain a meaningful value of PAS.

Furthermore, Figure 14 presents an example of the classification of the measured paths, i.e., a LOS or NLOS situation. From the 7 different paths of the MS, different *K-factor* values were computed and the classification performed. Each path is presented in Table 4 along with the corresponding classification.

The DoA analysis, mapped on to the office plan, indicates that Pos.6 and Pos.7 are in a LOS situation and as expected exhibit the highest *K-factor*. Note that Pos.3 indicates high *K-factor* for a NLOS scenario since the wall does not provide a strong obstruction to the direct signal. For indoor environment, the *K-factor* cannot be expected to be of a very high value in a LOS situation since in the magnitude of the direct signal is only marginal to the magnitude of the reflected signal especially in environments with small offices.

| Paths | Propagation scenarios | <i>K-factor</i> | |
|--------|-----------------------|-------------------|-------------------|
| | | MEA: Tx1-BSdipole | MEA: Tx2-BSdipole |
| Pos. 1 | NLOS | 0.7 | 1.2 |
| Pos. 2 | NLOS | 0.6 | 0.9 |
| Pos. 3 | NLOS | 0.9 | 1.4 |
| Pos. 4 | NLOS | 0.5 | 0.6 |
| Pos. 5 | NLOS | 0.8 | 0.5 |
| Pos. 6 | LOS | 2 | 2.1 |
| Pos. 7 | LOS | 1.4 | 1 |

Table 4: Propagation selection (LOS, NLOS) with their respective *K-factor*.

5.3.3.2 Situation where WSS Hold

Figure 15 presents 16 illustrations of the DoA estimation versus the displacement of the square MEAs for a LOS scenario measured at the airport. The rows represent the DoA estimation from the two square MEAs at the MS (Tx1 and Tx2) and the columns represent the antenna elements of the two MEAs. Columns {1-4} are the vertical dipoles of the first linear MEA and columns {5-8} represent the patch antennas, i.e., {5,7}: vertical (90°) and {6,8}: horizontal (0°).

For each graphic, the Y-axis represents the angle of arrival in degrees, i.e., from 0° to 360° and the X-axis represents the distance d travelled by the square MEA in wavelengths, i.e., $0.6\lambda \leq d \leq 10.4\lambda$. The reference point is taken from the centre of the square MEA. The results of each graphic are normalized to the maximum value of the dipole and patch MEAs for column {1-4} and {5-8} respectively so that the difference in the BPR is taken into account. The results are limited down to -13 dB in the illustration.

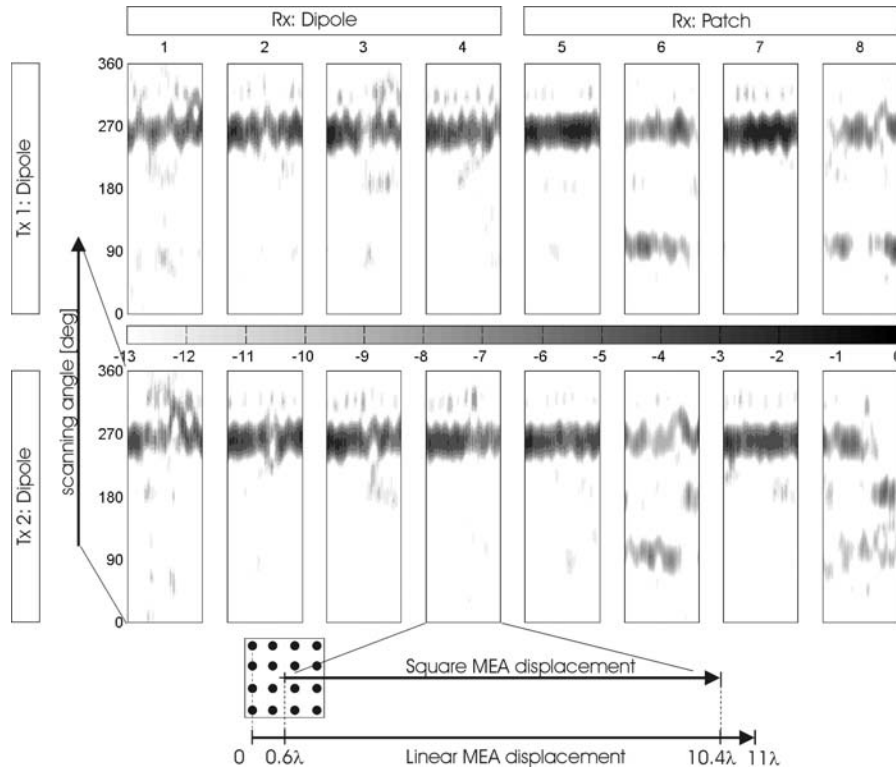


Figure 15: Example of a DoA estimation along the slide. WSS condition respected.

When considering the PAS for the Rx element $\{1-4\}$ and $\{5,7\}$, the energy is confined to a LOS scenario since both Tx and Rx elements have the same polarization. In the PAS seen from the elements $\{6,8\}$ more components contribute to the PAS since their polarization is different from the TX. The vertically transmitted signal needs to go through a richer scattering process to get cross-polarized for the horizontally polarized element $\{6,8\}$ and therefore the LOS is not sufficient in this case. Normal reflections on smooth surfaces preserve the polarization of the incident wave and to achieve cross-polarization oblique reflections and or irregular surfaces are necessary.

The WSS condition is respected since there are no differences in the DoA estimation and the fading statistics remain unchanged along all the displacements since all the energy is coming from a similar cluster. Also the PAS results from the first square MEA, Tx1, are similar to those obtained with the second square MEA, Tx2.

5.3.3.3 Situation where WSS does not Hold

In Figure 16, the PAS from Tx1 is not the same as the PAS from Tx2. Furthermore, when looking at Tx2, the PAS estimation at the Rx elements $\{1,2\}$ are different, even though they have the same polarization and are closely spaced.

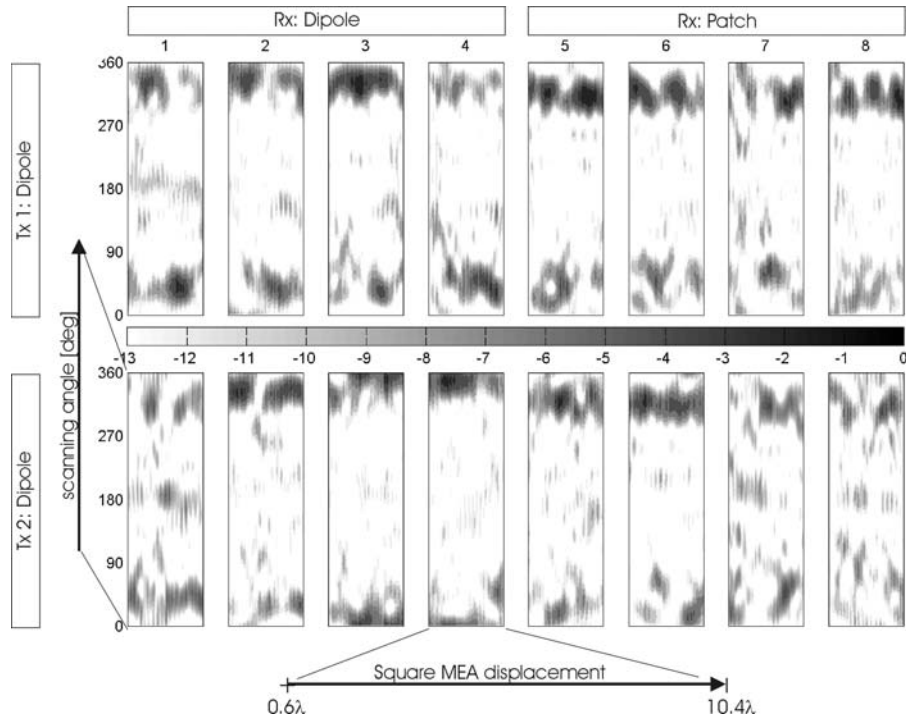


Figure 16: Example of a DoA estimation along the slide. WSS condition not respected.

Also, the Rx element {1} shows that for the same run the PAS is extremely variable meaning that different clusters contributes to the statistic of the signal within a run, which indicates that the WSS condition is not respected during that measurement.

5.4 Power Correlation Coefficient Analysis

Four different power correlation coefficients are investigated in this deliverable. They are defined and listed as follows

- The *spatial correlation coefficient* is the correlation coefficient between two elements of same polarization but separated by a spatial distance Δ_i . To facilitate the interpretation of the results, the spatial correlation between the elements is divided into three categories with different Δ_i . It is denoted $\left| \rho_{s\Delta_i} \right|$. Table 5 summarizes the three categories per project.
- The *polarization correlation coefficient* represents the correlation coefficient between two elements of different polarizations, but identical radiation patterns and no spatial separation. It is denoted $\left| \rho_p \right|$. The radiation patterns of dual-polarised antennas are assumed to be rotationally symmetric.

- The **joint spatial-polarization correlation coefficient** refers to the correlation coefficient between two elements of different polarizations, separated by a given spatial distance Δ_i , and identical radiation patterns. It is denoted $\left| \rho_{S\Delta_i+P} \right|$.
- The **joint pattern-spatial-polarization correlation coefficient** refers to the correlation coefficient between two elements of different polarizations, with two different radiation patterns and separated by a given spatial distance Δ_i . It is denoted $\left| \rho_{R+P+S\Delta_i} \right|$.

5.4.1 Spatial Domain

The spatial power correlation coefficient $\rho_{S\Delta_i}$ was computed for all the 79 picocell paths and 28 microcell paths. To provide a better overview of the correlation coefficient behaviour with respect to each cell type, i.e., microcell vs. picocell, the cdfs of the correlation coefficient are presented per cell and for several spatial element separations Δ_i . At the MS, the dipole element of the different MEA projects is considered and at the BS, the dipole and the +45° elements are used for the METRA and the SUNBEAM project respectively (see Table 5).





| Project Location | SUNBEAM | | METRA | |
|------------------|---|---|--|---|
| | MS | BS | MS | BS |
| Polarization | vertical | +45° | vertical | Vertical |
| Δ_1 | 0.5 λ | 0.45 λ | 0.4 λ | 1.5 λ |
| Δ_2 | 1.0 λ | 0.9 λ | 0.8 λ | 3.0 λ |
| Δ_3 | 1.5 λ | 1.35 λ | 1.2 λ | 4.5 λ |
| MEA set-up |  |  |  |  |
| | MS | BS | MS | BS |

Table 5: 3 categories of spatial correlation coefficient with respect to the spacing between elements.

Figure 17 presents the cdf of the spatial power correlation for the picocell environment. Figure 17 (i) illustrates the correlation coefficient behaviour at the MS and Figure 17 (ii) at the BS. Figure 18 illustrates the cdf of the correlation coefficient for the microcell environment for the METRA project and Figure 19 the SUNBEAM project. Conclusions based on the cdfs of the three figures are commented simultaneously.

The cdfs have to be read such that, for instance in Figure 17 (i), *for 50% of the measured paths, for the picocell environment, the spatial power correlation at the MS for elements separated by 0.4 λ is less than 0.38.*

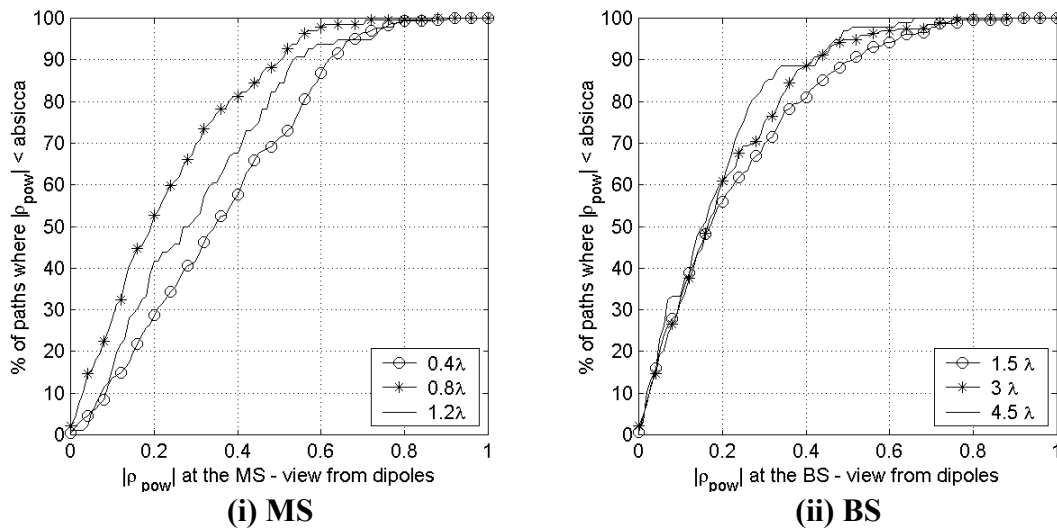
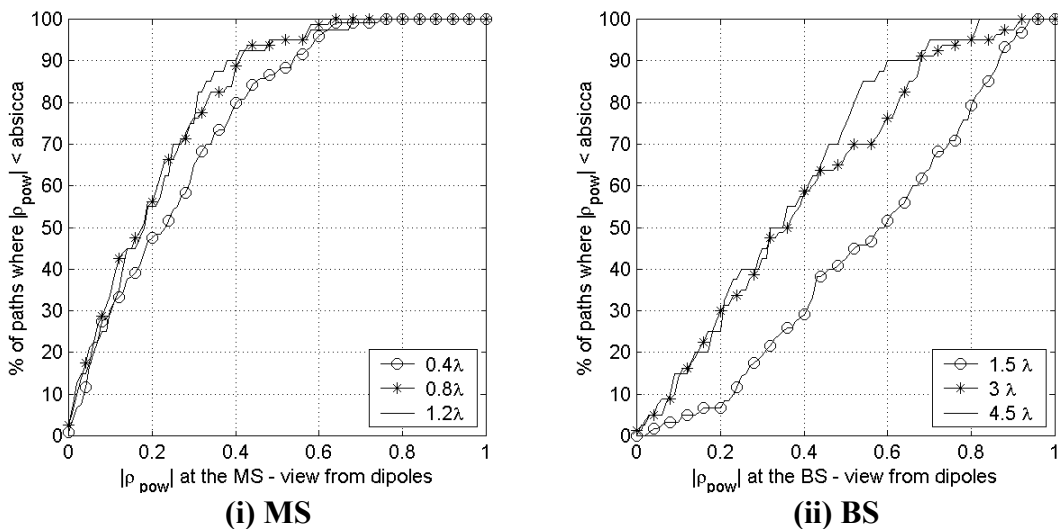


Figure 17: Empirical cdf of the power $|\rho_{S\Delta_i}|$ for the picocell environments.

At the MS, the correlation coefficient is low, $|\rho_{pow}| \leq 0.6$ for 90% of the measured paths for the picocell and microcell considering the small spatial separation, i.e., $\Delta_1 \leq 0.5\lambda$ to $\Delta_3 \leq 1.5\lambda$. The correlation coefficient behaviour either in the picocell scenario or in the microcell scenario is similar at the MS since the MS remains indoor and therefore illuminates the same scatterers.

At the BS, the correlation coefficient is low for the picocell, $|\rho_{pow}| \leq 0.6$ for 90% of the measured paths. This is to be expected with a larger separation between the elements of the MEAs ($1.5\lambda \leq \Delta_i \leq 4.5\lambda$) and the rich indoor scattering.



**Figure 18: Empirical cdf of the power $|\rho_{s\Delta_i}|$ for frb7 microcell environments-
 courtyard and parking-(METRA project).**

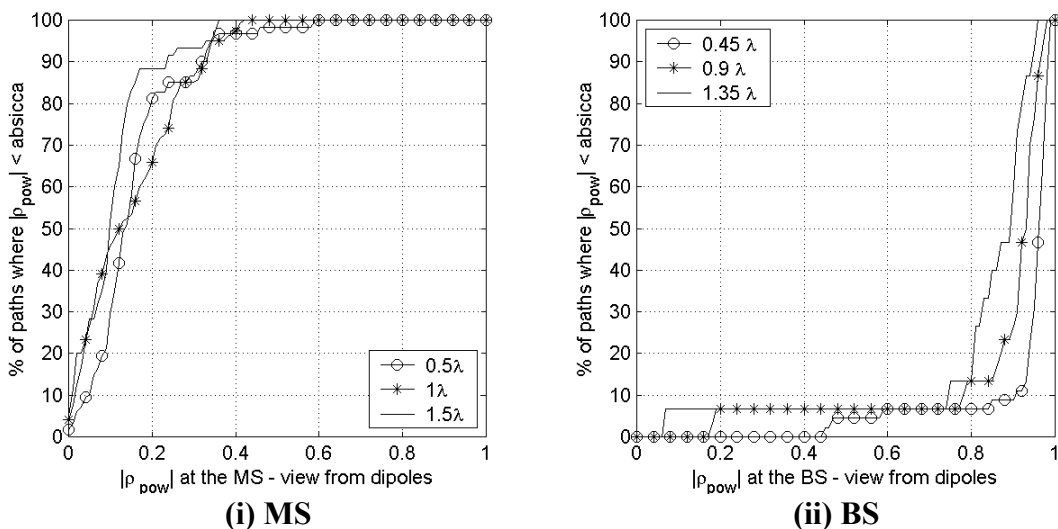


**Figure 19: Empirical cdf of the power $|\rho_{s\Delta_i}|$ for novi2 microcell environments
 (SUNBEAM project).**

For microcell environments investigated in the context of the METRA project, Figure 18, the smallest separation 1.5λ indicates a higher level of correlation than for the rest of the separation, i.e. $|\rho_{pow}| \leq 0.85$ for 90% of the measured paths for a spacing of 1.5λ whereas $|\rho_{pow}| \leq 0.65$ for 90% for $\Delta_1 \leq 3\lambda$.

For the microcell environments investigated in the context of the SUNBEAM project, the correlation at the BS is very high, $|\rho_{pow}| \leq 0.95$ for 90% of the measured paths, due to the low antenna separation and the low AS experienced in this environment.

Therefore, from a system perspective the deployment of spatial diversity at the BS is not recommended in this environment unless a separation larger than 4.5λ is used.

5.4.2 Polarization, Joint Spatial-Polarization and Joint Pattern-Spatial-Polarization Domain

The investigation of the spatial correlation behaviour of the MEA showed that spatial diversity technique could be easily employed in the indoor environment. However, when considering microcell environments, spatial diversity has to be obtained at the expense of a large antenna separation. This highlights the fact that when deploying the MIMO technology in wireless systems, the main question is *how to get enough decorrelation at both ends of the antenna system?* The alternative is to consider other diversity techniques to achieve low correlation values *all the time*.

Joint spatial-polarization diversity is interesting in the sense that the correlation coefficient is the product of the correlation coefficient in the polarization and the correlation coefficient in the spatial domain as reported in [61] for microcell environment so that

$$|\rho_{S_{\Delta_i}+P}| = |\rho_{S_{\Delta_i}}| \cdot |\rho_P|$$

An analysis of this property based on the measured data for picocell and microcell environment has been carried out to illustrate the work of [61].

To simplify the study, this section addresses the analysis of the power correlation coefficient considering vertically polarized dipole reference antennas, defined at the MS as

$$\rho_{n1n2,pow}^{MS} = \langle |\rho_{mn1}|^2, |\rho_{mn2}|^2 \rangle$$

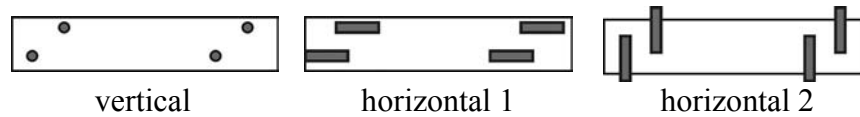
where m is the element vertically polarized and $n1$, $n2$ have different polarizations and radiation patterns and defined similarly at the BS as

$$\rho_{m1m2,pow}^{BS} = \langle |\rho_{m1n}|^2, |\rho_{m2n}|^2 \rangle$$

where n is the element vertically polarized and $m1$, $m2$ have different polarizations, and radiation patterns.

5.4.2.1 Analysis at the MS

This analysis is very similar to the one presented earlier in the spatial domain. This analysis focuses on the METRA measurement data only. Recall, that three different MEA configurations were deployed at the MS, namely vertical, horizontal 1 and horizontal 2.



Assuming that the radio channel was stationary for the duration of time spent in one path, it is possible to synthetically combine the MEA configurations to obtain hybrid MEAs. Table 6 presents the possible power correlation coefficients at the MS which are extracted from the hybrid MEA set-ups based on the measured data. This table is written in a symmetrical matrix format meaning that the upper triangular is only considered since the lower triangular is the same.

Figure 20 (i) and Figure 20 (ii) present the cdfs of all the correlation coefficient combinations for the picocell and microcell environments, respectively. The cdfs of all the combinations can be compared with the cdf of the spatial correlation coefficient analysed earlier.

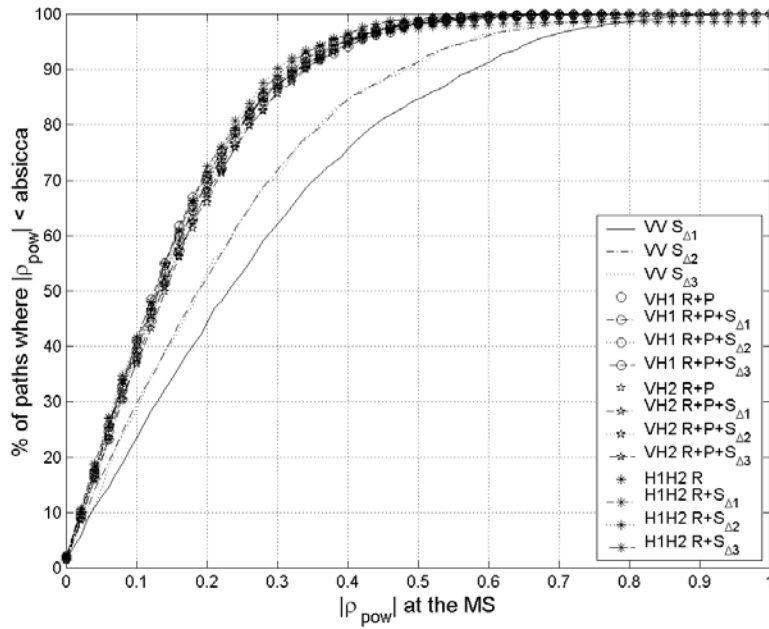
| $ \rho_{pow} $ | | vertical | | | | horizontal 1 | | | | ... |
|----------------|---|----------|----------|----------|----------|------------------|------------------|------------------|------------------|-----|
| | | 1 | 2 | 3 | 4 | 1 | 2 | 3 | 4 | ... |
| Vertical | 1 | 1 | S_{A1} | S_{A2} | S_{A3} | $R + P$ | $R + P + S_{A1}$ | $R + P + S_{A2}$ | $R + P + S_{A3}$ | ... |
| | 2 | | 1 | S_{A1} | S_{A2} | $R + P + S_{A1}$ | $R + P$ | $R + P + S_{A1}$ | $R + P + S_{A2}$ | ... |
| | 3 | | | 1 | S_{A1} | $R + P + S_{A2}$ | $R + P + S_{A1}$ | $R + P$ | $R + P + S_{A1}$ | ... |
| | 4 | | | | 1 | $R + P + S_{A3}$ | $R + P + S_{A2}$ | $R + P + S_{A1}$ | $R + P$ | ... |
| horiz. 1 | 1 | | | | 1 | S_{A1} | S_{A2} | S_{A3} | ... | |
| | 2 | | | | | 1 | S_{A1} | S_{A2} | ... | |
| | 3 | | | | | | 1 | S_{A1} | ... | |
| | 4 | | | | | | | 1 | ... | |
| horiz. 2 | 1 | | | | | | | | ... | |
| | 2 | | | | | | | | ... | |
| | 3 | | | | | | | | ... | |
| | 4 | | | | | | | | ... | |

| ... | horizontal 2 | | | |
|-----|------------------------|------------------------|------------------------|------------------------|
| ... | 1 | 2 | 3 | 4 |
| ... | $R + P$ | $R + P + S_{\Delta 1}$ | $R + P + S_{\Delta 2}$ | $R + P + S_{\Delta 3}$ |
| ... | $R + P + S_{\Delta 1}$ | $R + P$ | $R + P + S_{\Delta 1}$ | $R + P + S_{\Delta 2}$ |
| ... | $R + P + S_{\Delta 2}$ | $R + P + S_{\Delta 1}$ | $R + P$ | $R + P + S_{\Delta 1}$ |
| ... | $R + P + S_{\Delta 3}$ | $R + P + S_{\Delta 2}$ | $R + P + S_{\Delta 1}$ | $R + P$ |
| ... | R | $R + S_{\Delta 1}$ | $R + S_{\Delta 2}$ | $R + S_{\Delta 3}$ |
| ... | $R + S_{\Delta 1}$ | R | $R + S_{\Delta 1}$ | $R + S_{\Delta 2}$ |
| ... | $R + S_{\Delta 2}$ | $R + S_{\Delta 1}$ | R | $R + S_{\Delta 1}$ |
| ... | $R + S_{\Delta 3}$ | $R + S_{\Delta 2}$ | $R + S_{\Delta 1}$ | R |
| ... | 1 | $S_{\Delta 1}$ | $S_{\Delta 2}$ | $S_{\Delta 3}$ |
| ... | | 1 | $S_{\Delta 1}$ | $S_{\Delta 2}$ |
| ... | | | 1 | $S_{\Delta 1}$ |
| ... | | | | 1 |

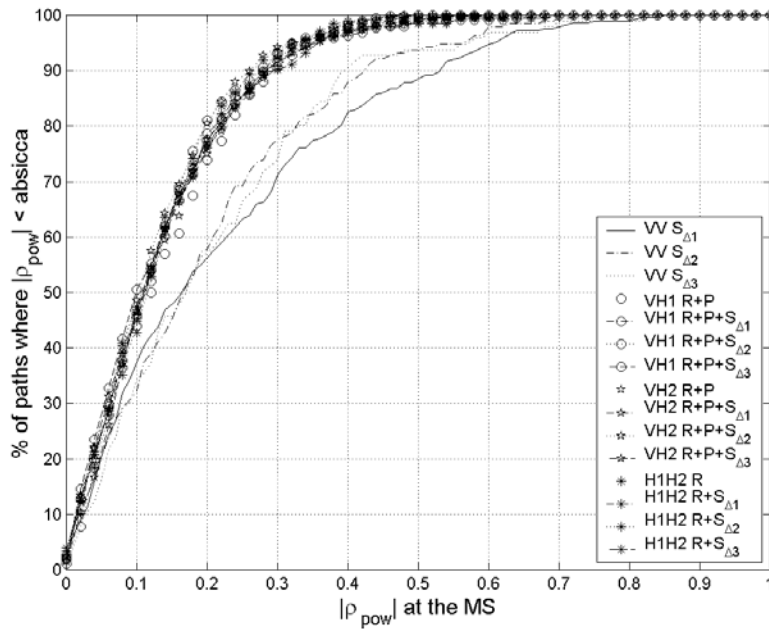
Table 6: Extraction of the possible $|\rho_{pow}|$ at the MS from the measured data. R: radiation pattern, P: polarization, $S_{\Delta i}$: spatial with separation Δ_i , $R + P + S_{\Delta i}$: joint pattern-polarization-spatial, $R + P$: joint pattern-polarization.

The results of Figure 20 show that even though spatial correlation values were low, introducing another polarization—with another radiation pattern—($\rho_{R+P+\Delta i}$) provides even lower values. Also when spatial diversity is combined with radiation pattern diversity ($\rho_{R+\Delta i}$), a low correlation value is provided. This conclusion is valid for both picocell and microcell environments. The cdfs of the different correlation combinations are very close to each other. Except for the spatial diversity, the values of correlation at 50% and 90% percentage levels extracted from Figure 20 are less than 0.15 and 0.35 respectively. This means that when the MIMO technology is to be deployed in indoor environment low correlation should be expected between the MEAs' elements.

The results of the correlation coefficient for the hybrid set {vertical + horizontal 1} and the hybrid set {vertical + horizontal 2} are similar. This is an interesting result since the outage correlation remains the same regardless of the orientation of the horizontal dipole in indoor.



(i) Picocell environments



(ii) Microcell environments

Figure 20: Empirical cdf of the power $|\rho_{pow}|$ at the MS for two cell type (METRA measurement data only).

5.4.2.2 Analysis at the BS

A direct comparison of the correlation coefficient between single polarized and dual polarized antenna configurations is presented here since dual polarized patch antennas with the same radiation pattern were employed at the BS.

Recall the two orientations of the patch antenna for the picocell measurement as illustrated in Figure 21. The patch is orientated $\pm 45^\circ$ for the picocell environment novi2, novi3, nokia and $90^\circ/0^\circ$ for fb7b2, and the airport. This difference in the patch orientation influences the correlation coefficient and also the BPR. This is very important and the consequences are treated in detail in Section 8.1.2. For the microcell measurement, two experimental set-ups are used with two orientations. The METRA measurement taken in fb7 used $90^\circ/0^\circ$ patch orientation and the SUNBEAM project (novi2) considered $\pm 45^\circ$ orientation as recalled in Figure 22 below.

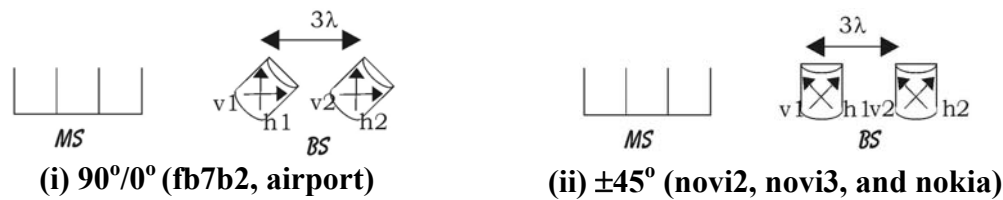


Figure 21: Rotation of the patch at the BS for the picocell environment (METRA).

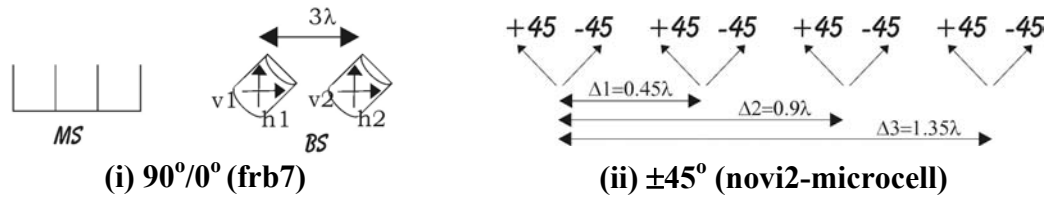


Figure 22: Rotation of the patch at the BS for the microcell environment (METRA+SUNBEAM).

Similar to the analysis performed at the MS, Table 7 describes the different combinations of power correlation coefficients which can be extracted from the measured data at the BS.

Figure 23 presents the cdfs for the different correlation coefficient combinations for the picocell environment. Figure 23 (i) presents the situation where the BS has the $90^\circ/0^\circ$ configuration, and the vertically transmitted polarized waves need to propagate through a rich scattering environment to be seen by the horizontal elements of the patch antenna. As a consequence, the correlation coefficient between the vertical and the horizontal element is low but the BPR is unequal (BPR = -8 dB).

In the case of Figure 23 (ii), the BS has the $\pm 45^\circ$ configuration. When the MS transmits vertical polarized waves, the waves do not need to go through rich different scatterers to be seen by the $+45^\circ$ and the -45° subsequently, the correlation coefficient between the

+45° and the -45° is high ($|\rho_{pow}| \leq 0.8$ at 90% of the measured paths), but the BPR is equal (BPR=0.9 dB).

| $ \rho_{pow} $ | v1 | h1 | v2 | h2 |
|----------------|----|-----|--------------------|--------------------|
| v1 | 1 | P | $S_{3\lambda}$ | $P + S_{3\lambda}$ |
| h1 | | 1 | $P + S_{3\lambda}$ | $S_{3\lambda}$ |
| v2 | | | 1 | P |
| h2 | | | | 1 |

Table 7: Extraction of the possible $|\rho_{pow}|$ at the MS from the measured data. P: polarization, S_{Δ_i} : spatial with separation Δ_i . $P + S_{\Delta_i}$: joint polarization-spatial.

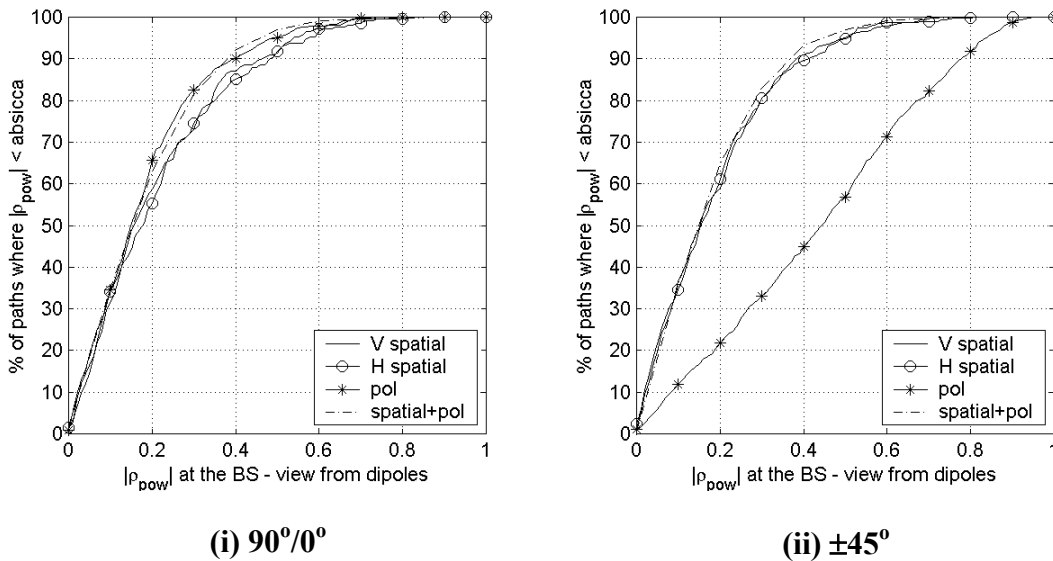


Figure 23: Empirical cdf of the power $|\rho_{pow}|$ at the BS for picocell scenario with respect to the two antenna orientations.

In both graphs, Figure 23 (i) and Figure 23 (ii), the range of correlation values in the spatial domain are identical irrespective of the orientation of the patches. From these results it can be concluded that at the BS, for the picocell environments, the orientation of the antenna when considering polarization diversity is of crucial importance if low correlation is necessary between the ports of the MEA.

Figure 24 presents the results for the microcell environments. In Figure 24 (i), the elements are 90°/0° orientated (Figure 22 (i)), i.e., based on the measurements taken in the context of the METRA project, whereas Figure 24 (ii) presents the microcell investigated during the SUNBEAM project where the elements are ±45° orientated.

As expected the power spatial correlation coefficient for the SUNBEAM project in Figure 24 (ii) is high due to the low spatial separation between the elements of the MEA and the existence of a low AS in more than 90% of the measured paths. The spatial power correlation coefficient for the frb7 environment is not as high as for the SUNBEAM, at 90% of the measured paths $|\rho_s| \leq 0.75$. The important conclusion is that in both graphs of Figure 24, the polarization diversity is a solution to achieve low correlation values compared to spatial diversity for microcell environments irrespective of the orientation of the patches. The joint spatial-polarization diversity technique represents the ultimate solution to obtain the lowest correlation values.

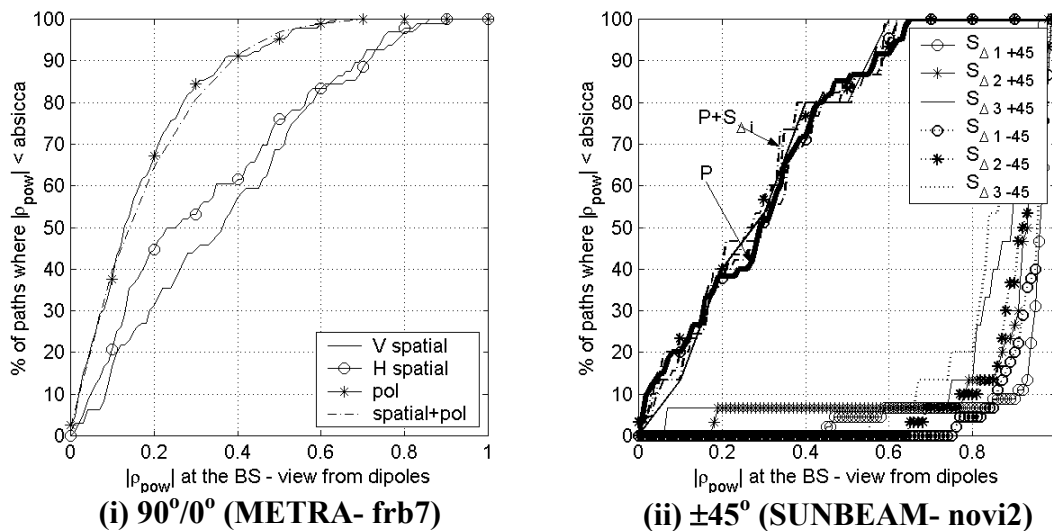


Figure 24: Empirical cdf of the power $|\rho_{pow}|$ at the BS for microcell scenario with respect to the two measurement set-up.

5.5 Reference Propagation Paths

In the rest of the deliverable six specific paths have been selected and used to present the behaviour of the MIMO technology performance. The selection of these six paths is motivated by their differences in terms of their propagation properties.

5.5.1 Example 1

Example 1 is a **partially decorrelated** scenario. At both the MS and the BS the correlation coefficient values are low. This is one of the paths from the picocell novi2 environment (several small offices environment).

5.5.2 **Example 2**

Example 2 represents the opposite situation to Example 1. The propagation scenario is **partially correlated**: this appears in one of the paths of the novi2-microcell environment extracted during the SUNBEAM project. The AS, at the BS, is about 3° ; as a result, the correlation coefficients between elements of same polarization are very high since all the energy received at the BS is confined to a narrow beam. The correlation coefficient at the MS is very low since the scattering in the indoor environment is rich enough so that only a small antenna separation of the order of 0.5λ is required to decorrelate signals. The measured signals from this example are Rayleigh distributed.

5.5.3 **Example 3**

Example 3 is a **partially correlated** scenario taken from the same environment as Example 2. However, contrary to Example 2, the measured signals indicate a Rice distribution with a *K-factor* of 3.

5.5.4 **Example 4**

Example 4 is a **partially decorrelated** scenario, extracted from the same set of measured data as for Example 2 and Example 3 (microcell novi2). An AS of approximately 20° has been identified; as a result, the correlation coefficient values are very low. The large AS experienced is explained by the presence of buildings located near the measurement paths. At the indoor MS, the situation is similar than for Example 2 and Example 3, i.e., low correlation.

5.5.5 **Example 5**

Example 5 is a **partially decorrelated** scenario, extracted from the nokia environment (a modern open office). The spatial correlation coefficients at both the BS and MS are very low. This particular example provides information for patch MEA being $\pm 45^\circ$ orientated. The measured signal are Rayleigh distributed.

5.5.6 **Example 6**

Example 6 exhibits the same spatial correlation and statistical distribution characteristics as Example 5 (**partially decorrelated** and Rayleigh distributed). It has been extracted from the Airport environment (a large open area). This particular example provides information for patch MEA being $90^\circ/0^\circ$ orientated.

5.6 Summary and Interim Conclusion

In this section a large number of topics related to the propagation aspect of the MIMO technology has been addressed.

Description of the post-processing of the measured data has been presented. It was shown that due to the low dispersivity of the radio channel and the time resolution of the measurement system, the measured data were exploited in their NB post-processed format.

The statistical distribution of the NB signal has been investigated in terms of the *K-factor*. At the same time a DoA analysis was performed. The two information sources were used together to categorise the environment investigated in terms of their LOS/low AS or NLOS/high AS characteristics.

Based on the DoA analysis applied to the measured data it was concluded that the angular distribution of the wave in indoor does not necessarily follow a uniform distribution but more a clustered type. From this, a meaningful PAS value could not be easily calculated. Furthermore, the DoA analysis enabled to decide whether the WSS requirement would hold for the measured data. It was shown that some measured paths did not hold such a requirement.

A detailed analysis of the power correlation coefficient has been performed in this section so that the performance of the MIMO technology developed in the next section can be explained. The analysis considered the spatial correlation coefficient, the polarization correlation coefficient, the joint spatial-polarization correlation coefficient, and the joint pattern-spatial-polarization correlation coefficient. The results are based on measured data for different cell environment, i.e., picocell and microcell, and different antenna configuration.

It was concluded that at the MS and the BS, for picocell environments, elements separated by 0.4λ would provide low correlation. For microcell environments, the correlation coefficient at the MS is also low. This is however not the case at the BS. Large separation would be required to achieve low correlation coefficient when spatial diversity is to be implemented. When polarization diversity is implemented, the orientation of the elements is of critical importance since for a low correlation between elements an unequal BPR may be occurring which results in a drastic deterioration of the MIMO technology performance. It is also shown that the joint spatial-polarization diversity technique represents the optimum solution to obtain the lowest correlation value for picocell and microcell.

6 UPGRADED VERSION OF THE IST METRA MIMO RADIO CHANNEL MODEL

The MIMO radio channel model was first presented in [18] and in the IST METRA Deliverable 2 [1] using the power correlation coefficient definition. To comply with the evolution of the 3GPP standardisation, a complex correlation coefficient definition of the radio channel model is presented and validated in both the spatial and the polarization domain. The philosophy of the model presented in IST METRA Deliverable 2 remains mostly unchanged.

Upgrade

- Complex correlation coefficient definition
- Consideration of BPR imbalance between MEA elements

A description on how to use the model (with the latest update) is presented below.

The limitation of the model will be discussed along the validation of the upgraded version of the stochastic MIMO radio channel model in the spatial and polarization domain.

6.1 How to Apply the Model

The purpose of the model is to simulate partially correlated MIMO channel coefficients α_{mn} from zero-mean complex i.i.d. random variables a_{mn} using the Cholesky decomposition procedure reported in [62]. The practical procedure to obtain α_{mn} , in a MIMO perspective, is sketched in a flow chart in Figure 25.

The degree of correlation is defined by the correlation matrix of the MIMO channel \mathbf{R}_{MIMO} derived from the complex average correlation matrix at the MS and the BS

$$\mathbf{R}_{MIMO} = \mathbf{R}_{MS} \otimes \mathbf{R}_{BS} . \quad (6.1)$$

The original zero-mean complex i.i.d. random variables a_{mn} have their amplitudes shaped in the frequency domain by the average measured Doppler spectrum and their phases uniformly distributed over $[0, 2\pi]$ such that MN independent and identically distributed variables are generated.

Originally, it was assumed that each α_{mn} is a complex variable with identical average power. This assumption can easily be relaxed and BPR imbalance in BPR between elements can be mapped into a matrix \mathbf{P} whose elements are the product of the standard deviations $\sigma_{\alpha_{mn}}$ of the channel radio links α_{mn} . The matrix of the complex covariance coefficient $\mathbf{\Gamma}$ is defined as

$$\mathbf{\Gamma} = \mathbf{R}_{MIMO} \times \mathbf{P} , \quad (6.2)$$

where \times represents the element by element multiplication. Consequently, $\mathbf{\Gamma}$ contains the correlation properties of the MIMO radio channel as well as the magnitude of each single radio link.

The symmetrical mapping matrix \mathbf{C} , also called the Cholesky triangle, results from the standard Cholesky factorization of the matrix

$$\mathbf{\Gamma} = \mathbf{C}\mathbf{C}^T , \quad (6.3)$$

provided that $\mathbf{\Gamma}$ is non-singular and the generation of correlated signals can be written as

$$\mathbf{A} = \mathbf{C}\mathbf{a} , \quad (6.4)$$

where $\mathbf{A}_{MN \times 1} = [\alpha_{11}, \alpha_{12}, \dots, \alpha_{M1}, \alpha_{M2}, \dots, \alpha_{MN}]^T$ and $\mathbf{a}_{MN \times 1} = [a_1, a_2, \dots, a_{MN}]^T$.

Subsequently, the generation of the simulated MIMO channel matrix $\tilde{\mathbf{H}}$ is a rearrangement of the vector \mathbf{A} so that

$$\mathbf{A}_{MN \times 1} \Rightarrow \tilde{\mathbf{H}}_{M \times N} , \quad (6.5)$$

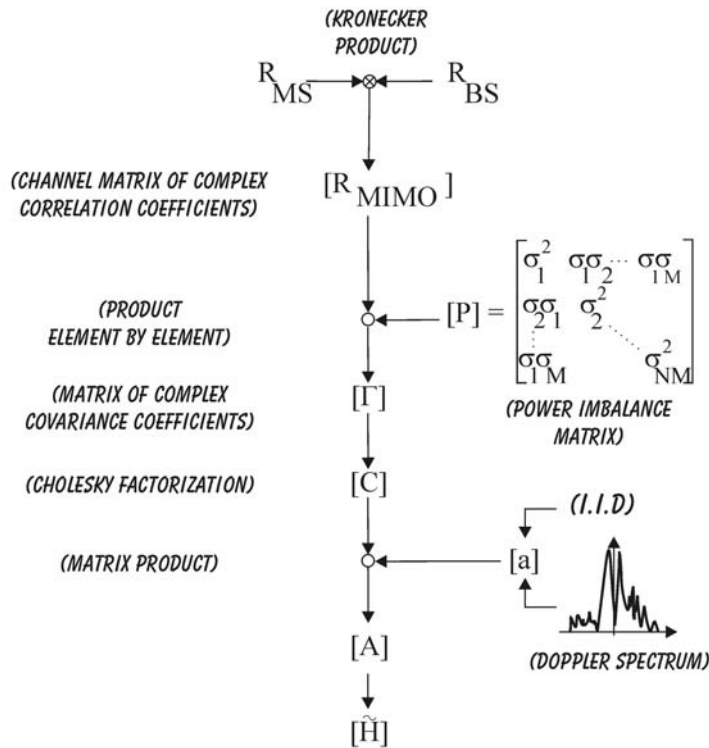


Figure 25: Flow chart of the MIMO model for the spatial domain

6.2 Limitations to the Model

The pin-hole scenario has its defenders; they argue that it exists and therefore should be modelled. However, it still remains the exception to the rule [17]. The aim of the model proposed in [18], redefined here in his NB format, and empirically validated in this study, is primarily aimed towards a professional audience who seeks to employ MIMO technology in realistic scenarios.

The proposed stochastic MIMO radio channel model cannot reproduce the pin-hole effect. The channel transfer matrix of the pine-hole is described in [29] as a dyad with one degree of freedom, where each channel coefficient α_{mn} writes as the product of two independent zero-mean complex Gaussian random variables. Therefore, the linear generation process described by (6.4) can not account for the product of random variables. Note, however, that even though measured data were collected in a wide variety of environments, the pin-hole effect was not observed.

6.3 Experimental Validation in the Spatial Domain

The purpose of this section is to present the validation results for the updated MIMO radio channel model. The principle of the local and the global validation has already been introduced in the IST METRA Deliverable 2. Therefore this section will briefly present the results of the global validation.

A global analysis encompassing all the measurement paths has been performed to measure the error between the measured and the simulated eigenvalue results. The analysis is based on the difference between $\lambda_{meas\ k}$ and $\lambda_{sim\ k}$ at 50% cdf level for each path and for each eigenvalue such that

$$\Delta_{error\ k} = \left[\lambda_{meas\ k} - \lambda_{sim\ k} \right]_{50\%}, \quad (6.6)$$

Figure 26 illustrates the cdf of $\Delta_{error\ k}$ calculated over the 107 investigated paths. Some discrepancies between the empirical and the simulated are present due to the fact that the simulated results are based on the average complex correlation matrix and average Doppler spectrum while the measured data are a set of real instantaneous realisations. Therefore, discrepancies may be likely to occur between measured and simulated data in the cases where the measured radio channels do not fulfil the WSS. Finally, the strength of the *K-factor* may contribute to the discrepancy between the measured and the simulated results.

For more clarity in the graph, the absolute value $|\Delta_{error\ k}|$ is considered since the distribution of $\Delta_{error\ k}$ is bound to be symmetrical around zero. The error generated by the proposed model is bounded for 80% of the paths within ± 0.6 dB for the first simulated eigenvalue λ_1 , within ± 1.6 dB for λ_2 , ± 2.2 dB for λ_3 , and ± 2.6 dB for λ_4 . As expected the higher the order of the eigenvalue the bigger is the discrepancy since they become more and more affected by the noise.

These $|\Delta_{error\ k}|$ values are considered to be reasonably small and enable to conclude that the proposed stochastic MIMO radio channel model is validated in the spatial domain.

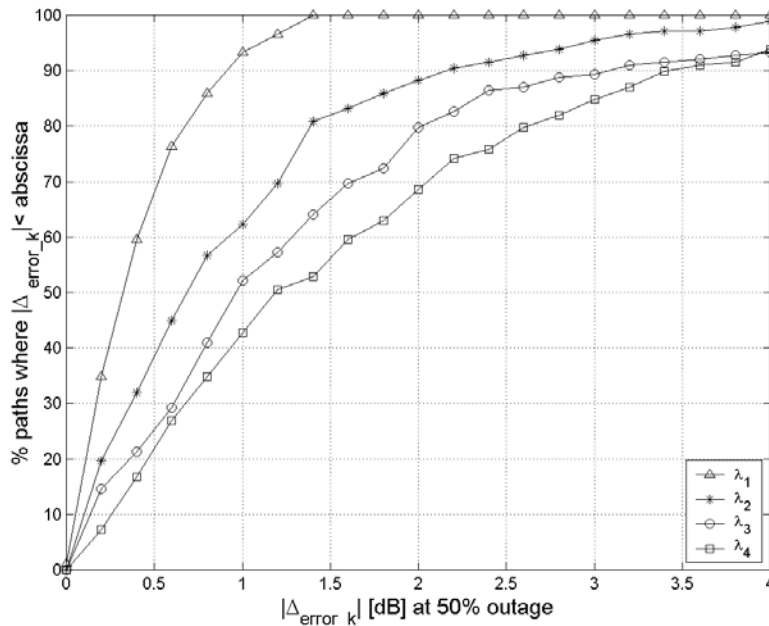


Figure 26: Global validation. Cdf of $|\Delta_{error_k}|$ over all the measurement paths.

6.4 Experimental Validation in the Polarization Domain

The dimensions of a large physical MEA is a general issue of concern for MIMO technology. A solution to mitigate this problem could be the use of dual-polarized antennas hence reducing the size of the MEA compared to only using spatial diversity. Therefore it is important, when modelling the MIMO radio channel, to also consider the validity of the model with respect to the polarization domain.

For clarity in the reading of the deliverable, the outcome of the validation procedure in the polarization domain is presented here only, whereas the validation procedure is presented in Appendix A. Two different methods of implementing the modelling of the radio channel in the polarization domain are described depending on the nature of the propagation scattering. These two methods treat the question whether the correlation coefficient, ρ , is dependent, or not, of the polarization of the reference element.

In the spatial domain, it was found that ρ is independent of the reference element. In the polarization domain, the first model option considers a *polarization-independent* definition of ρ and the second option a *polarization-dependent* definition. The dependency in the polarization would occur in a strong LOS situation. It was found that the scattering nature of the measured data limited the polarization investigation to only one method, therefore only the first option has been considered in the validation.

Figure 27 illustrates the local validation in the polarization domain. At both the MS and BS, the polarization diversity is considered. For this path, $BPR = -7.5 \text{ dB}$ and $BPR = -1.6 \text{ dB}$ were measured at the MS and BS respectively. The eigenvalues are normalized to the mean power of the elements $|h_{v|vj}|^2$, where V is implicitly the vertical polarization and i, j the index of the vertical elements.

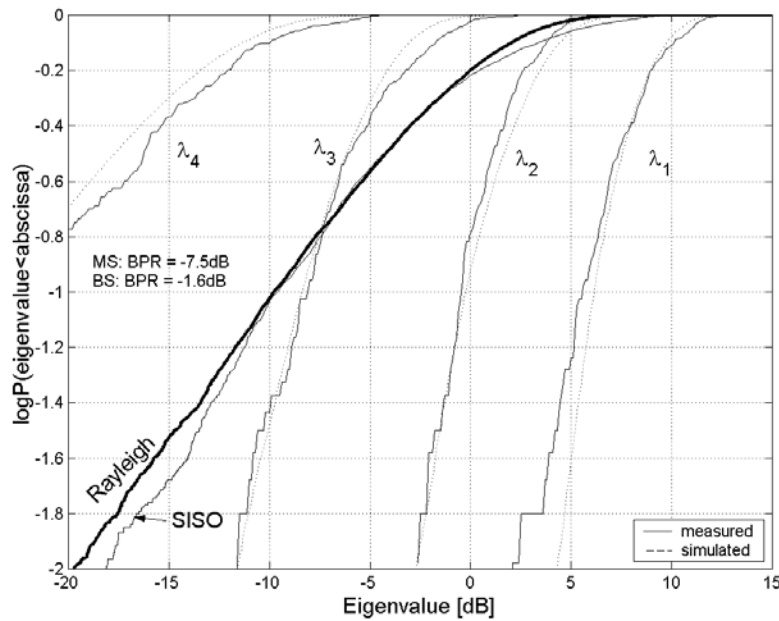


Figure 27: Local validation of the model. The cdfs of the 4 eigenvalues are presented for simulated and measured data. It can be seen that the set of simulated eigenvalues match the measured eigenvalues well.

The inspection of the measured and simulated curves of Figure 27 indicates that the cdfs of the eigenvalues generated from the stochastic model match the measured eigenvalues well.

A global analysis over all the measured paths of the METRA campaign has also been performed in order to measure the match between the measured and the simulated results. The $|A_{error\ k}|$ is presented in Figure 28 and indicates that at 50% cdf level the error is bounded for 80% of the investigated paths within $\pm 0.4 \text{ dB}$ for λ_1 , $\pm 1.5 \text{ dB}$ for λ_2 and λ_3 , and $\pm 2.4 \text{ dB}$ λ_4 . The $|A_{error\ k}|$ generated from $Array_1$ and $Array_2$ ⁶ are almost identical.

⁶ see Appendix A

These results allow concluding that the model reproduce realistic MIMO radio channels appropriately when considering polarization diversity for the 1st method.

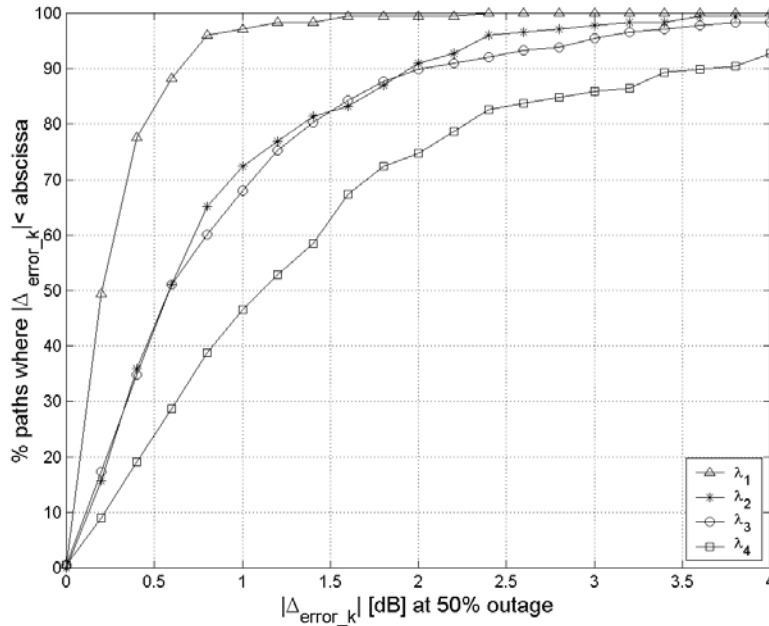


Figure 28: Global validation of the model. The cdfs of $|\Delta_{error_k}|$ when using *Array₁* quantitatively present the ability of the model to reproduce realistic MIMO radio channel.

6.5 Summary and Interim Conclusion

An updated version of the first METRA MIMO radio channel model [18] [1] has been presented

The validation procedure of the MIMO model consisted on the comparisons between measured eigenvalues and simulated eigenvalues. The model validation was performed in both the spatial and polarization domains. Local (investigation of one path at a time) and global (investigation all the paths treated at the same time) validation were considered. Their outcome indicates that the stochastic MIMO radio channel model renders the correlated propagation mechanisms appropriately for the spatial domain, and therefore has been validated in the NB condition. For the polarization domain, two different methods of implementing the model were described depending on the nature of the propagation scattering. The scattering nature of the measured data limited the polarization investigation to only one method. This method used to model the polarization domain was positively validated.

7 MATLAB IMPLEMENTATION OF THE MIMO RADIO CHANNEL

7.1 Foreword - Motivations

Before starting with the actual description of the MATLAB[®] implementation of the MIMO radio channel proposed by I-METRA, it is worthwhile spending some time explaining why this step has been regarded as beneficial, considering that another implementation of a previous version of the same model had already been provided by METRA.

The benefits of the new implementation are the following:

- Popularity of the simulation platform

The METRA implementation of the radio channel model is designed for Synopsys' COSSAP[®] platform, whereas I-METRA has selected Mathworks' MATLAB[®]. The main rationale for this change of approach is the fact that the latter platform is much more widespread than the former, what has been confirmed by the requests received for the shipping of the model (See section 7.7).

- Computation of the correlation matrices

The I-METRA MATLAB[®] package proposes an additional feature with respect to the METRA implementation, namely the computation of the correlation matrices corresponding to ULAs deploying an arbitrary number of omnidirectional antenna elements, arbitrarily spaced, and impinged by clustered PASs (uniform, truncated Gaussian or truncated Laplacian). This new feature enables to start the simulation of MIMO channels from a high-level description of the scenario under study, namely the geometrical description of the MEAs and the characteristics of the PASs. At the end of the pre-processing phase, the MATLAB[®] package derives the corresponding correlation matrices, which are then ready to be fed to the model.

- Up-to-date implementation

The design of a new implementation of the MIMO radio channel model has benefited from the refinements of the model described in Section 6. It has also been an incentive to keep this implementation as much as possible inline with the evolution of the standardisation, first in 3GPP, and more recently, in SCM AHG.

7.2 Introduction

This section describes the content of the MATLAB[®] implementation of the MIMO radio channel proposed by I-METRA. The package contains two directories

Correlation_Multiple_Cluster and *UMTS_Testbed* where one can find the MATLAB[®] scripts enabling to

- Derive the spatial correlation properties of a Uniform Linear Array (ULA) impinged by a variety of PAS, namely uniform, truncated Gaussian and truncated Laplacian, where the waves are gathered in a single or in multiple clusters. The relations applied to derive these properties are detailed in [63].
- Simulate a MIMO radio channel at link-level in compliance with 3GPP specifications [64]. The simulated model is of stochastic type. It is fully described in [65][66].

Figure 29 summarises the interactions between the scripts of the two directories.

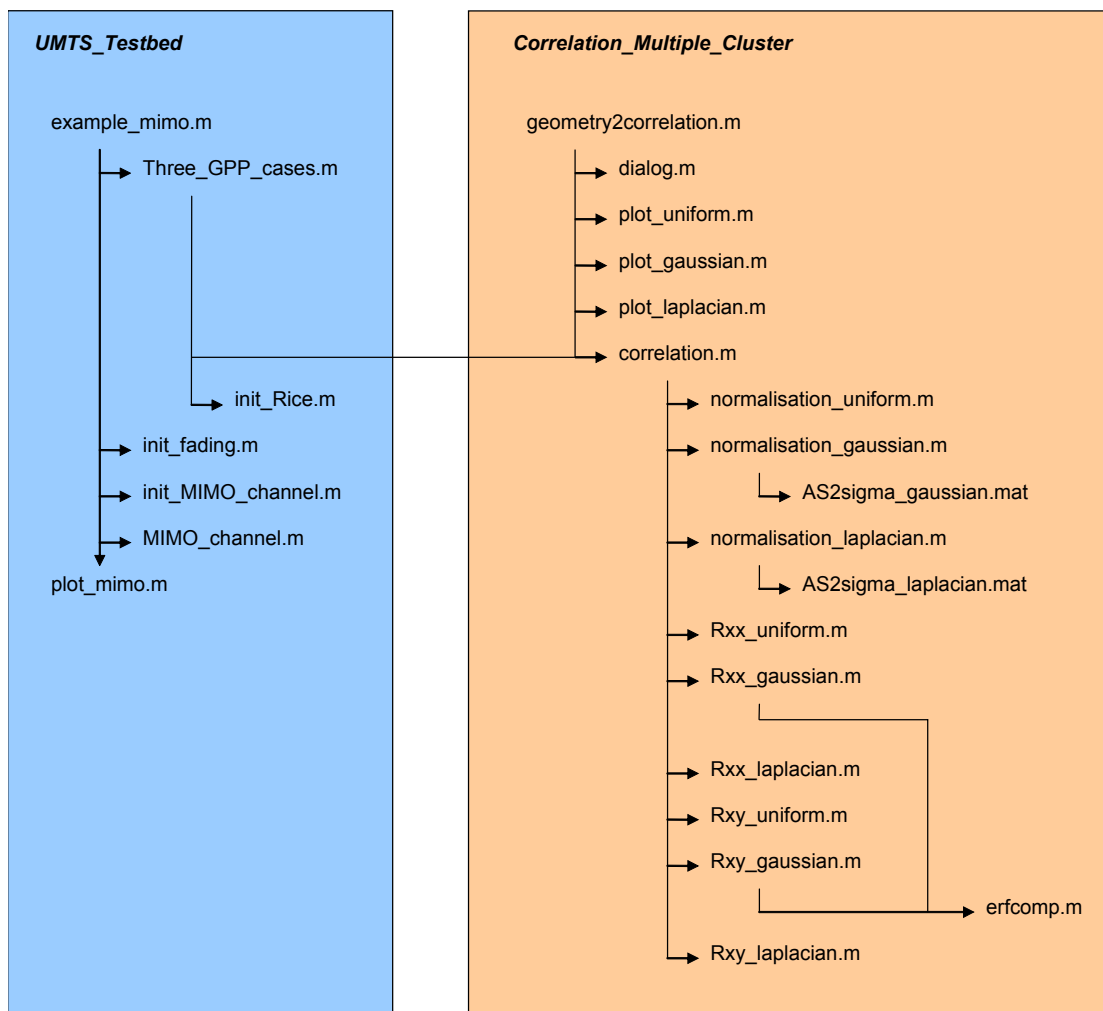


Figure 29: Interactions between the MATLAB[®] scripts

Following the description of the package, validation results are presented. The distribution terms are stated at the end of the document, along with statistics of the diffusion so far. Finally, the limitations of the current implementation are listed.

7.3 Spatial correlation – Directory *Correlation_Multiple_Cluster*

The main script is *geometry2correlation.m*. Through a dialogue with the user, this script first collects all the information requested to fully characterise the scenario, namely the number of antenna elements of the ULAs at the MS and at the BS, their spacings, the PAS types of the impinging waves, their AS, and their AoD/AoA.

In a second phase, the spatial correlation properties are derived by the script *correlation.m*.

The first step of this phase is to normalise the PAS such that it can be regarded as a probability distribution, which means that

$$\int_{-\pi}^{\pi} PAS(\varphi) d\varphi = 1 \quad (7.1)$$

On the other hand, this normalisation step, performed in *normalisation_*.m* scripts, serves to derive the standard deviation of this pdf, based on the AS defined by the user, as there is not necessarily an identity between them.

Being normalised, the PAS is then integrated over its definition domain according to the relations established in [63] to derive the spatial correlation coefficients. The coefficients of the homogeneous products between real (imaginary) parts are derived in *Rxx_*.m* scripts, while the mixed products between real and imaginary parts are handled by *Rxy_*.m* scripts. Their outcome is combined to produce either complex field spatial correlation coefficients or real power ones, depending on the value of a calling variable of the *correlation.m* script.

Finally, the correlation coefficients fill two matrices defined at the UE and at the Node B, respectively \mathbf{R}_{MS} and \mathbf{R}_{BS} . These spatial correlation matrices are combined through a Kronecker product as described in Section 6. The structure of the Kronecker product depends whether one wants to simulate a downlink transmission

$$\mathbf{R}_{MIMO} = \mathbf{R}_{BS} \otimes \mathbf{R}_{MS} \quad (7.2)$$

or an uplink one

$$\mathbf{R}_{MIMO} = \mathbf{R}_{MS} \otimes \mathbf{R}_{BS} \quad (7.3)$$

Note that the correlation matrix \mathbf{R}_{MIMO} defined here above differs from the matrix \mathbf{R} defined in (4.5) since $\mathbf{R}_{\text{MIMO}} = \text{vec}(\mathbf{H})\text{vec}(\mathbf{H})^H$ where the operator $\text{vec}(\cdot)$ reshapes a matrix into a column vector.

As a matter of illustration, Figure 30 shows 2-cluster PASs⁷, where both clusters are constrained within $[-60^\circ, 60^\circ]$ around their AOAs $\{-90^\circ, 90^\circ\}$ and exhibit an AS of 30° . Note that the second cluster has half the power of the first one. The envelope correlation coefficient of two distant antennas impinged by these PASs is shown in Figure 31 as a function of the distance between the antennas. It exhibits oscillations which have also been reported in [67]. In [67], it is claimed that the more different the mean AoA of the two clusters, the higher the spatial frequency of these oscillations. One can also notice the wider oscillations obtained with the truncated Laplacian PAS. They could be due to the strong confinement of the Laplacian PAS.

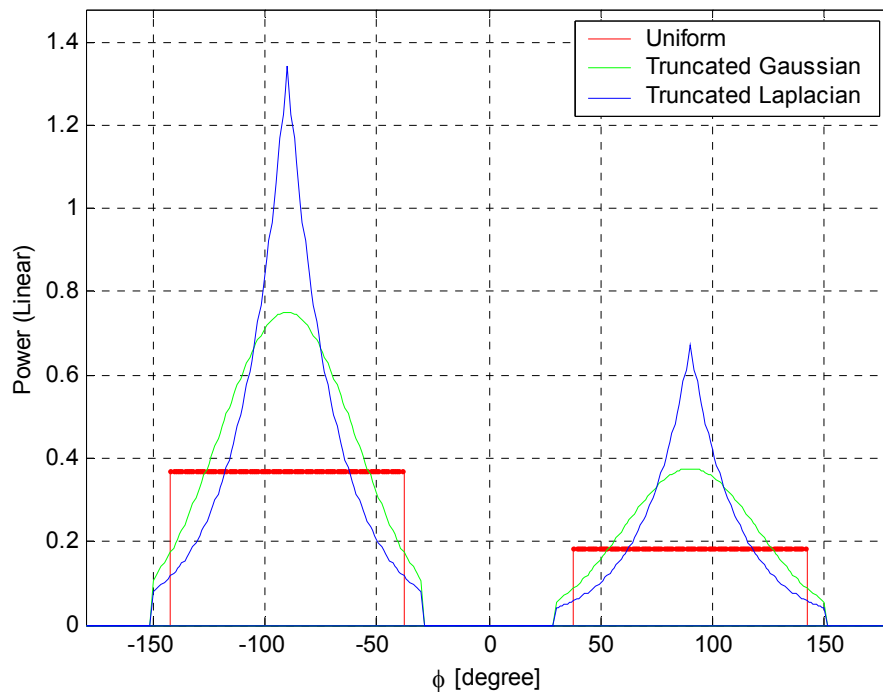


Figure 30: Examples of 2-cluster PASs

⁷ Also known as "bimodal PAS", see for instance [67].

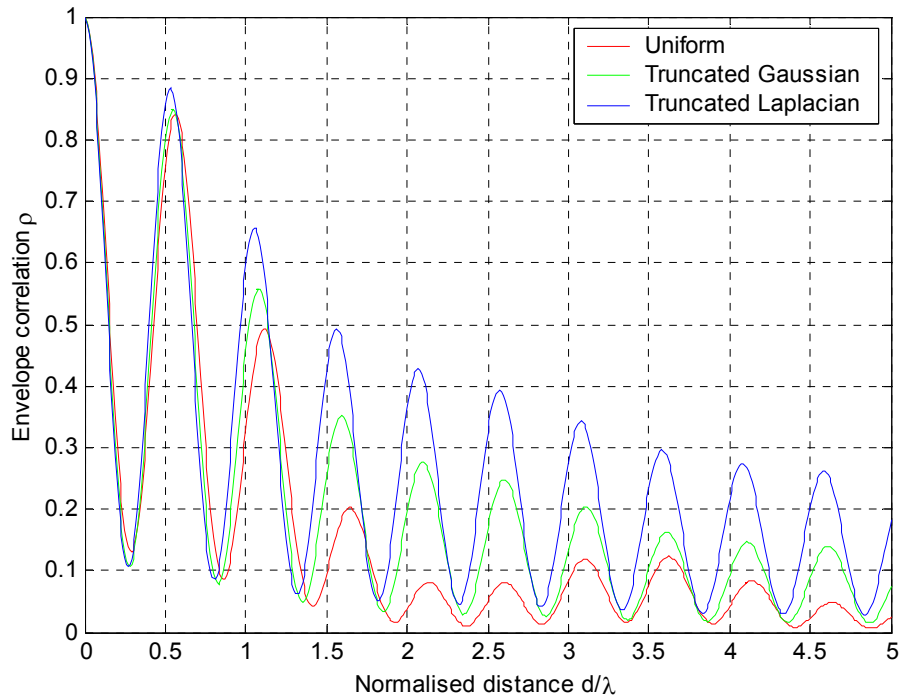


Figure 31: Envelope correlation coefficient of the PASs shown in Figure 30

7.4 MIMO radio channel – Directory *UMTS_Testbed*

The main script is *example_MIMO.m*. It shows how the scripts written to generate a MIMO radio channel can be embedded in a broader link-level simulation.

Following the approach of Synopsys' COSSAP/CCSS (CoCentric System Studio) [68], the script distinguishes an initialisation phase, during which parameters are read and global variables are initialised, and a processing phase, during which the actual simulation runs.

7.4.1 Initialisation phase

At initialisation, the parameters of the set-up (PAS, AoD/AoA, AS, Power Delay Profile-PDP, etc.) are initialised in the *Three_GPP_Cases.m*. This is the script that ought to be updated with the new parameter set-ups to be approved by SCM AHG. This question is discussed in Section 7.5.

Since all the geometric information required to derive the spatial correlation properties is available in the *Three_GPP_Cases.m* script, the computation of the spatial correlation matrices at Tx and Rx is performed from that script, by a call to the *correlation.m* script described in the previous section. Its outcome, two spatial correlation matrices, are combined in the main loop through a Kronecker product into matrix \mathbf{R}_{MIMO} , and a spatial

correlation shaping matrix \mathbf{C} is derived from \mathbf{R}_{MIMO} by Cholesky or Square-Root Matrix decomposition [70], depending whether one is willing to deal with complex field correlation coefficients or real power ones. Whatever decomposition is selected, its argument should be positive definite. Matlab's implementation of the Cholesky decomposition tests by default the positive definition of its argument. As far as the Square-Root Matrix decomposition is concerned, such a test has been implemented in the code.

Additionally, a Rice steering matrix is computed from the outer product of the steering vectors defined in Appendix B of [64], which writes as follows

$$\begin{bmatrix} \exp\left\{2j\pi \frac{d_{Rx}}{\lambda} \sin(AoA_{Rx})\right\} \\ \vdots \\ \exp\left\{2j\pi \frac{d_{Rx}}{\lambda} (n_{Rx} - 1) \sin(AoA_{Rx})\right\} \end{bmatrix} \begin{bmatrix} \exp\left\{2j\pi \frac{d_{Tx}}{\lambda} \sin(AoD_{Tx})\right\} \\ \vdots \\ \exp\left\{2j\pi \frac{d_{Tx}}{\lambda} (n_{Tx} - 1) \sin(AoD_{Tx})\right\} \end{bmatrix}^T \quad (7.4)$$

where λ is the wavelength, n_{Tx} and d_{Tx} represent respectively the number and the spacing of the antenna elements for the transmit ULA, n_{Rx} and d_{Rx} represent respectively the number and the spacing of the antenna elements for the receive ULA, AoD is the angle of Departure and AoA the angle of Arrival. This steering matrix is to be used later to shape the Rice component of Case 2 of [64].

Having initialised the parameters of the set-up, especially the ones related to the fading properties, the script *init_fading.m* is called to generate $n_{Paths} \cdot n_{Tx} \cdot n_{Rx}$ vectors of *FadingNumberOfIterations* fading samples, sampled every $\lambda / 2 \cdot FOF \cdot v$ second, where n_{Paths} is the number of taps of the PDP, *FOF* is the oversampling factor of the fading process and v is the speed. The $n_{Paths} \cdot n_{Tx} \cdot n_{Rx}$ vectors of *FadingNumberOfIterations* independent fading samples are generated by performing the inverse Fourier transform of an oversampled Doppler spectrum whose shape has been defined in the *Three_GPP_Cases.m* script. A random phase is applied to each vector in the frequency domain so as to generate independent fading processes in the time domain from a single, common Doppler pattern. This procedure is explained in full detail in [1] and is illustrated in Figure 32.

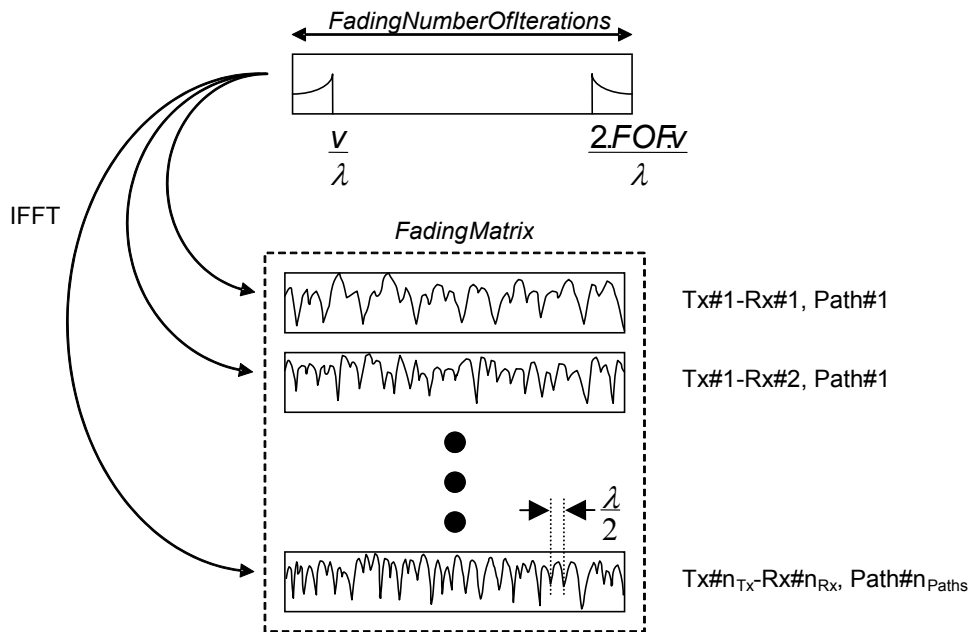


Figure 32: Generation of *FadingMatrix*

These vectors are then gathered into a single matrix, *FadingMatrix*, which is correlated using the spatial correlation shaping matrix C derived earlier. The whole philosophy of the process is to provide the main loop with a reference library of correlated fading samples in which the actual tap coefficients to be used during the simulation will be derived by simple linear interpolation. Therefore, one should make sure that these fading vectors span at least a distance of 40λ , such that, when wrapping around, the last samples of the fading vector can be regarded as uncorrelated in the time domain with respect to the first ones.

Finally, the lines of *FadingMatrix*, where each line correspond to a tap coefficient, are scaled according to the PDP and the Rice component is added, if necessary.

7.4.2 Processing phase

As a foreword, it should be mentioned that the main loop of the *example_MIMO.m* script has been written having in mind the formalism presented in [71]. However, a user willing to use the MATLAB[®] package for the sole purpose of generating a MIMO radio channel could create his/her own link-level simulations, using the spatially correlated *FadingMatrix* generated at the end of the initialisation phase. In that perspective, the main loop of *example_MIMO.m* is just an example of the way to use this channel generator in the broader scope of a link-level simulation.

Anyway, the main loop of *example_MIMO.m* is designed to process one burst of *NumberOfChipsPerIteration*, possibly oversampled chips per iteration. A global variable keeps track of the running time instant, for book-keeping purposes, but also to enable the simulation of burst transmissions. As it is, the running time instant is incremented by the

length of *NumberOfChipsPerIteration* chips at each iteration. This could be easily changed, in order to simulate burst transmissions. The incremental step could then be defined according to a given probability distribution function depending on the corresponding traffic model.

For each iteration, the script *MIMO_channel.m* performs two linear interpolations in the spatially correlated *FadingMatrix*. The first interpolation is applied in the time domain. It consists in collecting (possibly fractionally if oversampling) chip-spaced fading samples in *FadingMatrix*. The second interpolation is performed in the tap domain. It consists in distributing every tap of the PDP on the two closest sampling instants of the simulation, according to the time distance with respect to them, as described in [72]. This second interpolation is required by the fact that the PDP is not necessarily sampled at the simulation rate. Figure 33 illustrates these two interpolation processes, in the case of a chip-spaced simulation of the ITU Pedestrian A profile. Note that the weights of the second interpolation are the square-roots of the time differences, in order to preserve the correlation properties.

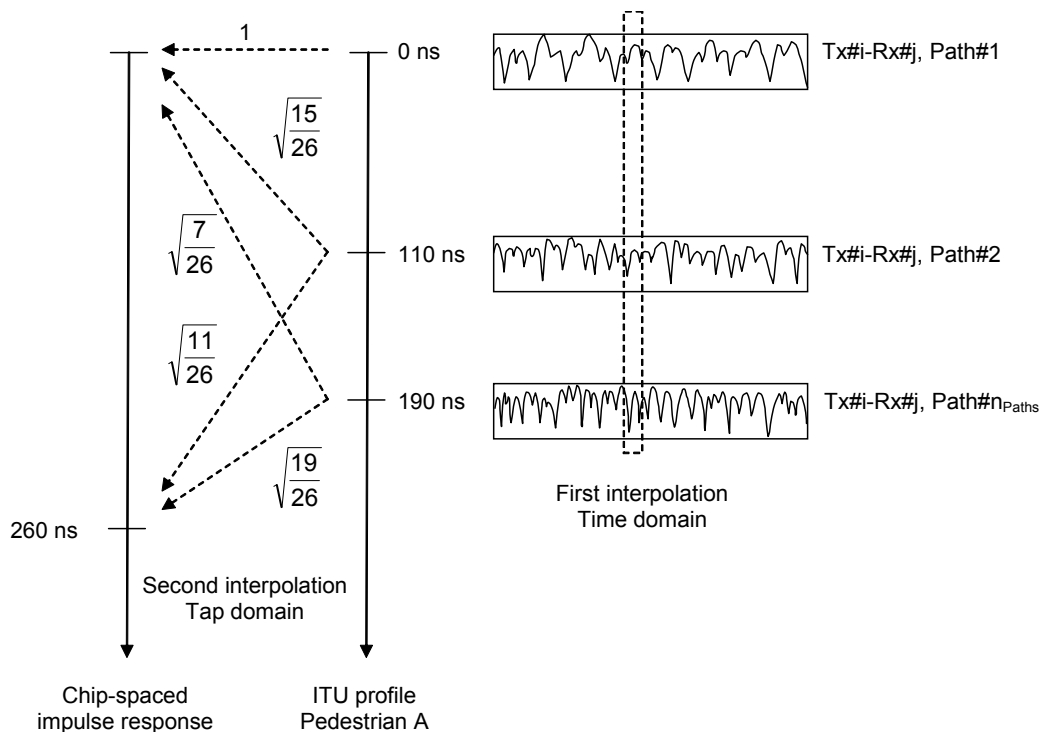


Figure 33: Double interpolation of the correlated fading process in the main loop

The outcome of *MIMO_channel.m* is two matrices containing the same information, namely the MIMO channel to be applied to the current burst. One of these two matrices, the *Channel* variable in *example_MIMO.m*, has a sliding structure compliant with the formalism of [71] illustrated in Figure 34. The second matrix, *CorrelatedFading*, has the same row structure than *FadingMatrix*. However, its columns span the simulation sampling space instead of the fading one.

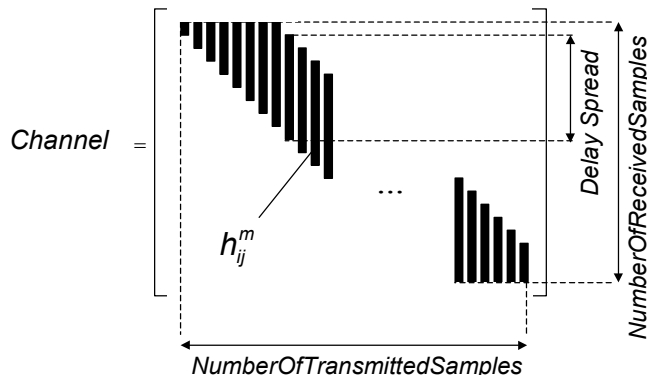


Figure 34: Sliding structure of Channel

7.4.3 Post-processing phase

As a matter of post-processing, the package contains the script *plot_MIMO.m*. It plots the $n_{\text{Paths}} \cdot n_{\text{Tx}} \cdot n_{\text{Rx}}$ impulse responses generated by *example_MIMO.m*, the $n_{\text{Tx}} \cdot n_{\text{Rx}}$ PDPs, the n_{Paths} spatial correlation functions and the $n_{\text{Paths}} \cdot n_{\text{Tx}} \cdot n_{\text{Rx}}$ Doppler spectra. Whenever possible (PDP, correlation, Doppler spectrum), the characteristics of the simulated MIMO channel are compared to the desired ones. Note that *plot_MIMO.m* uses a downsampled version of the *CorrelatedFading* matrix mentioned here above.

The following pages present the PDP, the spatial correlation properties and the Doppler spectra of a 2x2 MIMO set-up in 3GPP Cases 2, 3 and 4 as defined in [64]. Dashed red curves/circles are the original values, blue curves/circles are the simulated ones. The shift of Taps 2 to 4 in the PDP of Case 2 (Figure 35) is due to the additional 3-dB Rice component on Tap 1. Figure 40 shows Doppler spectra of impinging waves constrained within a Laplacian PAS. Finally, note the changing spatial correlation properties of Case 4 in Figure 43, reflecting the changing propagation conditions from one tap to the other.

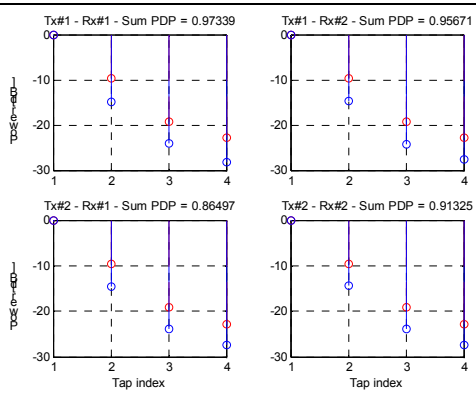


Figure 35: PDP of 3GPP Case 2 (4 taps)

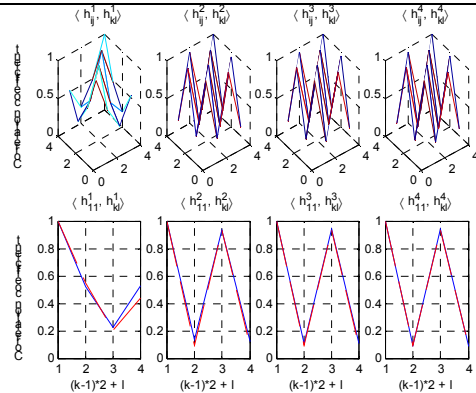


Figure 36: Spatial correlation properties of 3GPP Case 2

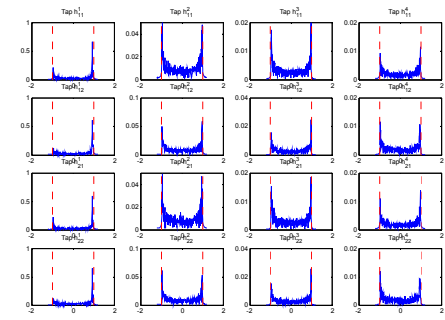


Figure 37: Doppler spectra of the 2*2*4 = 16 taps of a 3GPP 2x2 MIMO channel Case 2

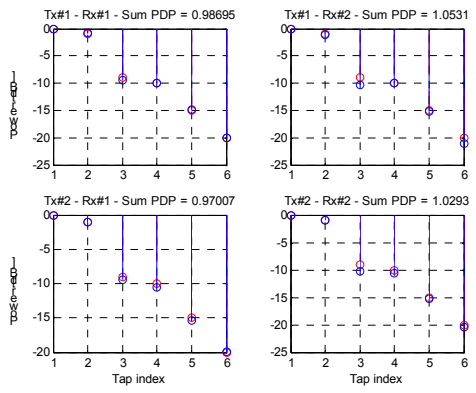


Figure 38: PDP of 3GPP Case 3 (6 taps)

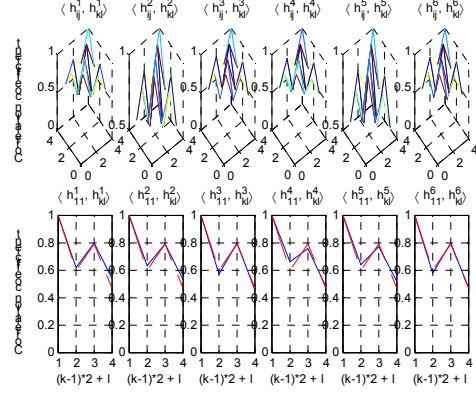


Figure 39: Spatial correlation properties of 3GPP Case 3

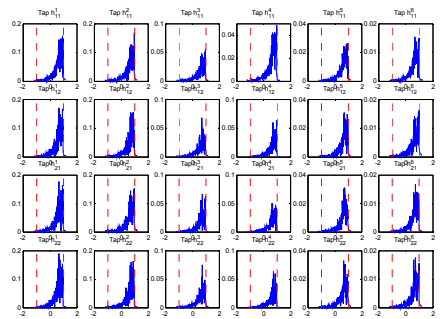


Figure 40: Doppler spectra of the 2*2*6 = 24 taps of a 3GPP 2x2 MIMO channel Case 3

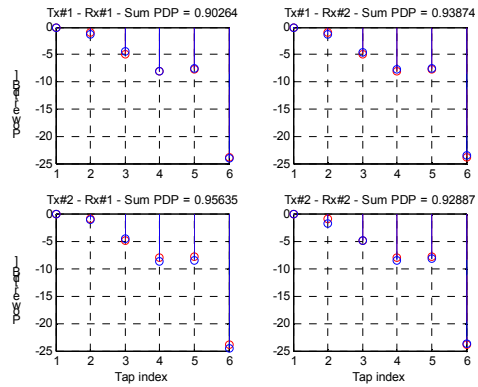


Figure 41: PDP of 3GPP Case 4 (6 taps)

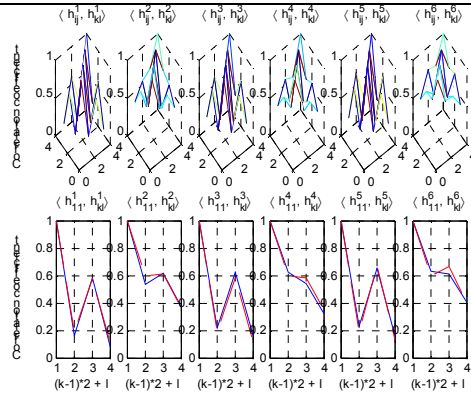


Figure 42: Spatial correlation properties of 3GPP Case 4

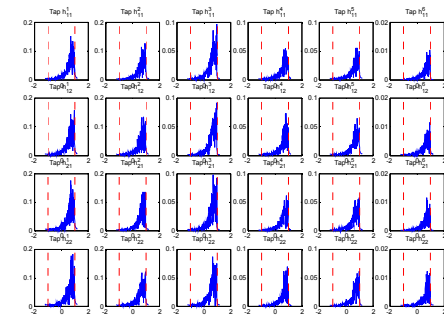


Figure 43: Doppler spectra of the $2 \times 2 \times 6 = 24$ taps of a 3GPP 2×2 MIMO channel Case 4

7.5 Limitations of the implementation

The current version of the implementation suffers from some limitations that are discussed here after:

➤ Support limited to 2-D linear array geometries

For the time being, only ULAs are supported by the implementation, as the building of the correlation matrices implicitly assumes such kind of geometry. This means that the support of other regular geometries like Uniform Circular Arrays (UCA) for instance can be considered, through the writing of a specific module

- deriving the spacings and the AoAs/AoDs for pairs of elements placed at the vertices of a UCA,
- computing the corresponding correlation coefficients with the help of the current implementation,
- finally inserting the results in a correlation matrix.

➤ Support of non omnidirectional antennas

As mentioned earlier, the standardisation of the MIMO radio channel for UMTS scenarios has been taken over by an ad-hoc group, the Spatial Channel Model Ad Hoc Group, since April 2002. With respect to the latest proposal from 3GPP, the link-level proposal of SCM AHG is very similar, see [74]. However, SCM AHG has introduced directional radiation patterns. The support of such patterns require an update of the closed-form expressions used by the package to derive the correlation values of a given pair of elements.

7.6 Distribution terms

The MATLAB[®] packages developed by CSys⁸ are free of use to any party having approved beforehand and on an individual basis the terms of the following agreement:

1. The receiving party agrees to acknowledge CSys'parenthood on the MATLAB[®] package by referencing in every publication it may produce in the future based on the use of these packages the JSAC paper [65] or CSys'newer related publications.
2. The receiving party agrees to acknowledge cooperation with IST project IST-2000-30148 I-METRA [73] in every publication it may produce in the future based on the use of this package.
3. The receiving party agrees not to distribute the source code to third parties.

⁸ "CSys" stands for the Cellular Systems professional group of the KOM department of Aalborg University, Denmark.

4. In order to ensure that any enhancement might benefit to the whole community using the package, the receiving party agrees to notify CSys of any change and/or improvement of the source code, and to document it.

As soon as the approval of a party on these terms will have been received, the MATLAB[®] package will be sent to this party.

7.7 Distribution statistics

As of October 29, 2002, the two implementations of the MIMO radio channel model had been shipped to 57 different third parties not involved in the I-METRA consortium. 48 requests had been sent for the MATLAB[®] implementation, while the COSSAP[®] one had interested 17 parties⁹. The detailed distribution statistics are as follows:

| IST Project | | METRA | I-METRA |
|---------------------|---------------|---------------------|---------------------|
| Simulation platform | | COSSAP [®] | MATLAB [®] |
| Industry | | 6 | 11 |
| Non profit | Europe | 6 | 13 |
| | North America | 0 | 8 |
| | Asia | 2 | 11 |
| | Oceania | 1 | 2 |
| | Total | 9 | 34 |
| Individuals | | 2 | 3 |
| Grand total | | 17 | 48 |

7.8 Summary and Interim Conclusion

This section has described the content and the working of two MATLAB[®] packages, *Correlation_Multiple_Cluster* and *UMTS_Testbed*, aimed at deriving the spatial correlation properties of a MIMO radio channel and at simulating it. These packages have been validated by showing their outcome in the case of the 3GPP cases described in [64]. The limitations of the current implementation have been documented. Finally, the terms of the distribution of the package have been stated, as well as the status of their diffusion at the time of writing the current document.

⁹ There are more distributed implementations than third parties, since some of them requested both implementations.

8 PERFORMANCE EVALUATION OF THE MIMO RADIO CHANNEL

In this section, the impact of the propagation properties of the radio channel on the parallel subchannelling concept is presented. Having understood the basic concept of MIMO, a number of factors which influence the number of eigenvalues and thereby the optimisation of the MIMO technology can be listed below

- Number of elements in the MEA configuration
- Correlation properties of the MIMO radio channel
- BPR between the MEA ports

The conclusions and recommendations are supported by capacity results, based on measured and simulated data, to emphasize the consequences of these parameters on MIMO system performance. The estimation of the spectral efficiency is based on the calculation of the Shannon capacity formula (see Section 4.5.4). This study is limited to a single-user scenario where two power allocation strategies are compared; water-filling and uniform power allocation.

Recall that the capacity results presented here are theoretical values for error-free transmission in the presence of background noise and provide an idea of the MIMO performance. To reach these values, in real life, coding (e.g. turbo coding) detection, constellation size among others should be considered in the system implementation. For an isolated MIMO system, i.e., single user scenario, the results presented here are a theoretical upper limit to the achievable data rate.

8.1 Impact of the Radio Channel on the MIMO Performance

This section presents the impact of the correlation properties of the radio channel on the parallel subchannels offered by the MIMO concept. This is addressed for the spatial, polarization and joint spatial-polarization domains. These results are based from the measured radio channel data.

Mainly two paths were identified for their propagation properties and used in the analyses of this section unless otherwise mentioned. The measured data are extracted from the indoor-to-outdoor microcell of the SUNBEAM project measurement campaign. They have been introduced in Section 5.5 on page 54 for their two distinctive ASs and are reminded below:

- **Example 3**: AS of about 3° ; as a result, the correlation coefficients between elements of same polarization are very high ($\rho \leq 0.9$). This is a partially correlated scenario with a Rice distribution.
- **Example 4**: AS of approximately 20° , as a result, the correlation coefficient values are low ($\rho \leq 0.5$). This is a partially decorrelated scenario.

Recall that in both cases, the correlation coefficient at the MS is very low ($\rho \leq 0.3$) since the scattering in the indoor environment is rich enough so that only a small element separation of the order of 0.5λ is required to decorrelate signals.

8.1.1 Spatial Domain

The results illustrate very well the influence of the radio channel in the spatial domain on the concept of parallel subchannelling (Figure 44) and its consequences for the capacity (Figure 45).

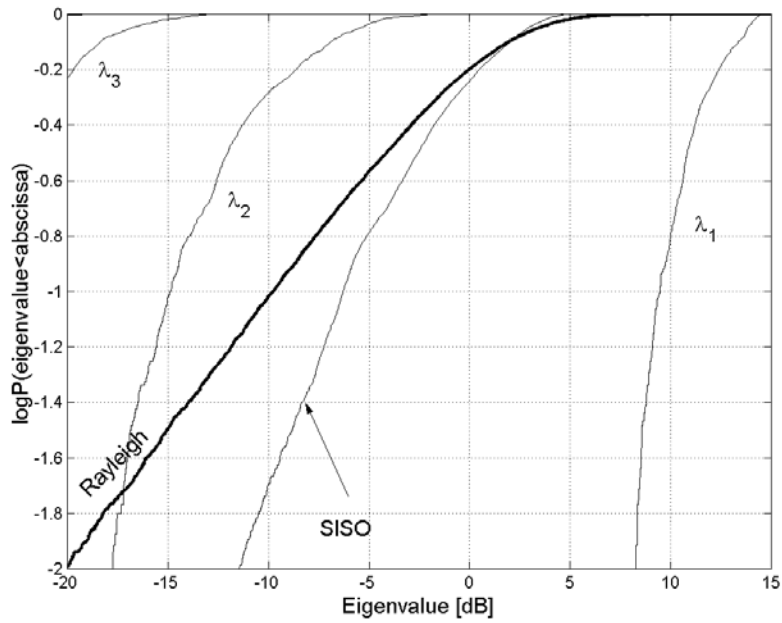
The eigenvalue analysis of the measurement data is performed on a 4×4 MEA configuration; results of the eigenanalysis are presented in Figure 44. The MS consists of four vertical polarized elements with 0.5λ separation and the BS consists of the same number of element with 0.45λ separation. The cdfs are computed over the full run of the Tx mast, 20λ in this case.

Figure 44 (i) illustrates the partially correlated scenario only. The high gain of the MEA at the BS due to the low AS results in one strong eigenvalue, λ_1 , while the second strong eigenvalue λ_2 is 25 dB lower than λ_1 . For the partially decorrelated scenario, illustrated in Figure 44 (ii), λ_2 and λ_3 become more significant. The cdf of the measured eigenvalues in the partially decorrelated scenario is in relatively good agreement with the theoretical study presented in [14] where fully decorrelated i.i.d. radio links were assumed.

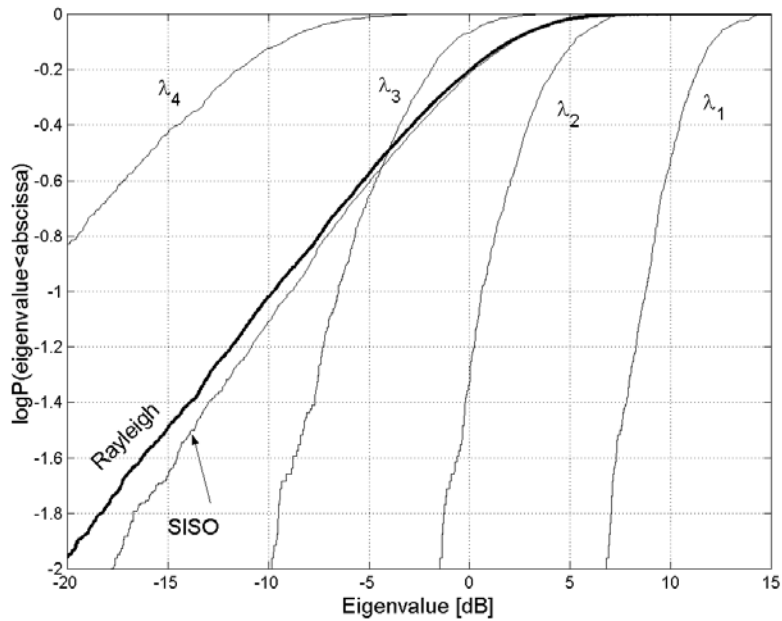
The difference in the number of parallel subchannels within the same microcell emphasizes the need for a more robust MIMO technique to counteract the environmental fluctuations. This may be achieved either by increasing the spacing between the elements of the MEA or by using polarization diversity as shown later in this section.

Figure 45 illustrates the impact of each subchannel, identified in Figure 44, upon the total capacity available, assuming a mean SNR per Rx element of 30 dB. The total capacity $\sum C_i$ at the 10% level, for the correlated case in Figure 45 (i), is 17 b/s/Hz due to the fact that only two channels, identified by λ_1 and λ_2 , are contributing. When the MIMO radio channel is decorrelated, i.e., the contribution of λ_1 , λ_2 and λ_3 is significant, a tremendous total capacity of 27.9 b/s/Hz is achievable.

The comparison between the two power allocation strategies on the total capacity indicates that the difference is very small when the elements of the MEA are sufficiently decorrelated. However, it must be emphasized that the water filling strategy always provides a higher capacity than the uniform strategy, which is in good agreement with results reported in [19].

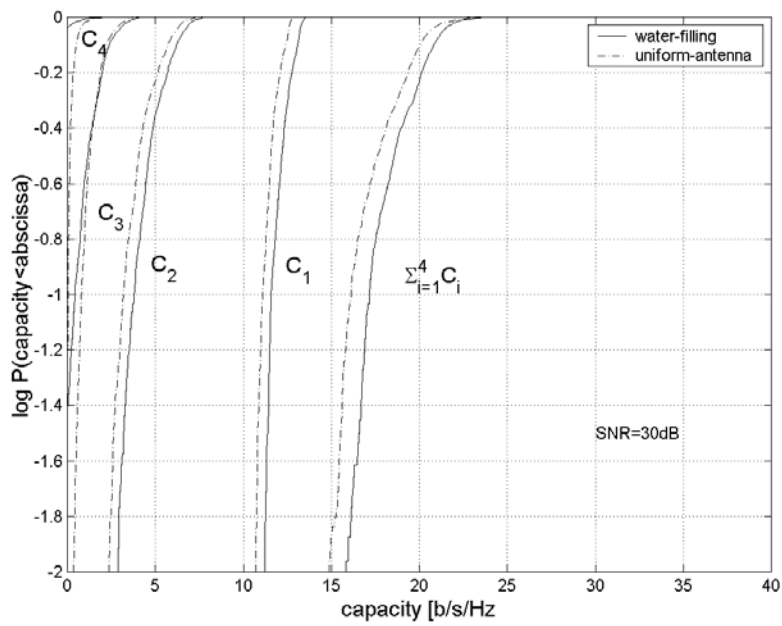


(i) Example 3, partially correlated scenario in the spatial domain, $AS \approx 3^\circ$ at the BS.

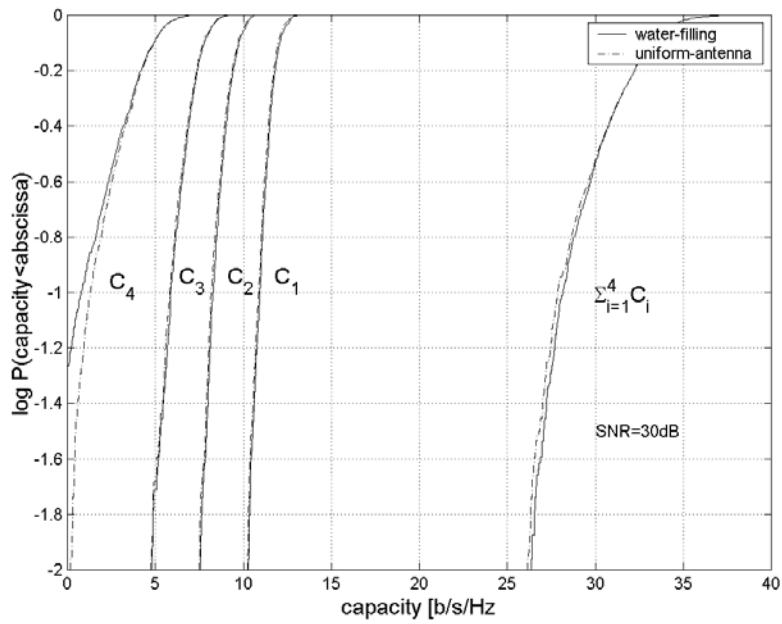


(ii) Example 4, partially decorrelated scenario in the spatial domain, $AS \approx 20^\circ$ at the BS.

Figure 44: Cdfs for the eigenvalues for two distinct radio channel properties within the same microcell environment.



(i) Capacity results for Example 3



(ii) Capacity results for Example 4

Figure 45: Empirical example of the mapping between the eigenvalue and the capacity within the same microcell environment (SNR=30 dB).

8.1.2 Impact of the MEA Topology

A convenient comparison of the performance of different MIMO system is the total spectral efficiency of different MEA topologies. The spatial domain is only considered here and the two spatial environments presented above are investigated.

Table 8 and Table 9 summarize the total capacity achievable for all the $M \times N$ configuration topologies possible ($M, N \leq 4$) based on measured channel data. The values are presented for a mean SNR per Rx element of 30 dB and at 10% level.

Table 8 shows that in a partially correlated propagation scenario, when considering the correlation between the MEA elements at the BS, the capacity achieved by a 1×4 system is 11.1 b/s/Hz which is greater than for a 4×1 system (9.9 b/s/Hz). The difference between the two topologies is about 1 b/s/Hz, which is explained by the 3 dB difference in gain shown in Figure 5 on page 22 for the partially correlated scenario ($\log_2(2)=1$).

| $M \times N$ | | Water filling | | | | Uniform | | | |
|----------------|---|-----------------|------|------|------|----------------|------|------|------|
| | | M elements (BS) | | | | M element (MS) | | | |
| | | 1 | 2 | 3 | 4 | 1 | 2 | 3 | 4 |
| N element (MS) | 1 | 7.9 | 8.9 | 9.5 | 9.9 | 7.9 | 8.9 | 9.5 | 9.9 |
| | 2 | 9.7 | 11.1 | 12.2 | 13.6 | 8.7 | 10.8 | 12.1 | 13.5 |
| | 3 | 10.5 | 12.5 | 14.1 | 15.7 | 8.9 | 11.5 | 13.3 | 15.2 |
| | 4 | 11.1 | 13.6 | 15.4 | 17.2 | 9.1 | 11.9 | 13.9 | 16.1 |

Table 8: Capacity (b/s/Hz) comparison at 10% level for different MEA topologies with a mean SNR per Rx element of 30 dB. Example 3, Partially correlated scenario, $AS \leq 3^\circ$ at the BS.

| $M \times N$ | | Water filling | | | | Uniform | | | |
|----------------|---|-----------------|------|------|------|----------------|------|------|------|
| | | M elements (BS) | | | | M element (MS) | | | |
| | | 1 | 2 | 3 | 4 | 1 | 2 | 3 | 4 |
| N element (MS) | 1 | 6.7 | 8.5 | 9.5 | 10.3 | 6.7 | 8.5 | 9.5 | 10.3 |
| | 2 | 8.9 | 13.7 | 16.6 | 18.4 | 8.0 | 13.7 | 16.6 | 18.4 |
| | 3 | 10.1 | 16.8 | 20.8 | 24.4 | 8.5 | 15.7 | 20.7 | 24.4 |
| | 4 | 10.5 | 18.3 | 23.9 | 28.2 | 8.9 | 16.3 | 22.7 | 27.9 |

Table 9: Capacity (b/s/Hz) comparison at 10% level for different MEA topologies with a mean SNR per Rx element of 30 dB. Example 4, Partially decorrelated scenario, $AS \leq 20^\circ$ at the BS.

Table 9 also shows that since the channel is partially decorrelated, i.e., the correlation between the MEA elements at the BS and the MS are decorrelated, the number of elements at both ends of the link are interchangeable without significant changes in the capacity results i.e. a 1×4 system gives $10.9 \text{ b/s/Hz} \approx 10.3 \text{ b/s/Hz}$ achieved by a 4×1 system.

When the MIMO MEAs configuration is symmetrical, i.e., $M=N$, the difference between the water filling and the uniform power allocation is marginal in the considered scenario. However, in the case when the MEA configuration is asymmetrical, i.e., $M \leq N$, the total capacity considering the uniform power allocation is different with respect to the MEAs set-up so that $C_{M \times N} \neq C_{N \times M}$ and subsequently, the difference with the water filling become more significant depending on the selected MEA set-up. In the case where there are more MEA elements at the Rx than the Tx, i.e., $N \leq M$, the uniform power allocation does not waste any power since the potential number of subchannels is equal to the number of Tx MEA elements. However in the case where $N \geq M$, i.e., more Tx elements than at the Rx, the potential number of achievable subchannels is the same and the Tx power is wasted, consequently $C_{N \geq M} \leq C_{N \leq M}$. When $N \geq M$ the difference between the water-filling and the uniform power allocation is significant. In the rest of the deliverable the optimum power allocation, i.e. the water filling scheme, is used to present total capacity results since they are not affected when $M \neq N$.

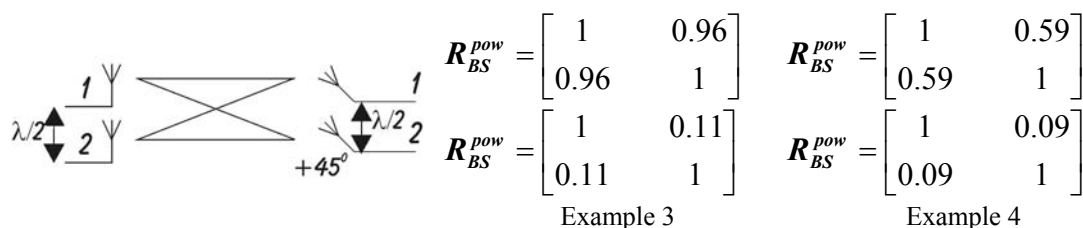
8.1.3 Polarization Domain

To remedy the weakness of the spatial diversity technique with respect to the variation of the propagation properties of the radio channel in the spatial domain, two methods can be used. The first method is to increase the spatial separation between the elements and therefore consider a larger MEA somewhat cumbersome. The second method is the use of polarisation diversity which is considered in this section.

The results presented here consider the same radio channel as described earlier in Example 3 and Example 4, a partially correlated ($AS \approx 3^\circ$ at the BS) and a partially decorrelated ($AS \approx 20^\circ$ at the BS) scenario respectively.

Two 2×2 MIMO MEA topologies are compared. They differ at the BS: one system uses spatial diversity and the second system employs polarization diversity only, i.e., dual polarized collocated elements with no spatial separation.

- 2×2 spatial: The MS consists of two vertical polarized elements with a spacing of 0.5λ and the BS consists of two $+45^\circ$ elements with a spacing of 0.5λ . An illustration of the MIMO setup is given below along with the mean power correlation coefficient matrix at both the BS and MS.



- 2x2 pol: The MS consists of two vertical polarized elements with a spacing of 0.5λ and the BS consists of two dual polarized $\pm 45^\circ$ collocated elements, i.e., with no spacing. An illustration of the MIMO setup is given below along with the mean power correlation coefficient matrix at both the BS and MS.

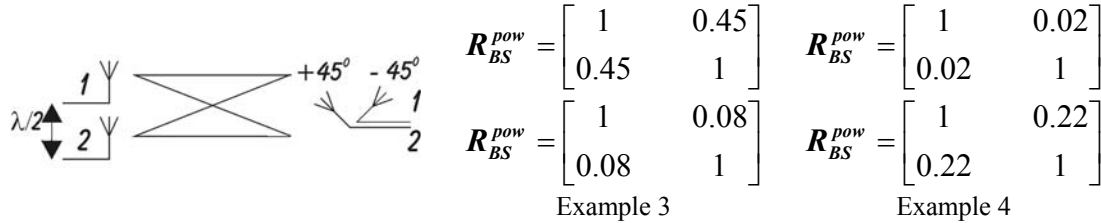
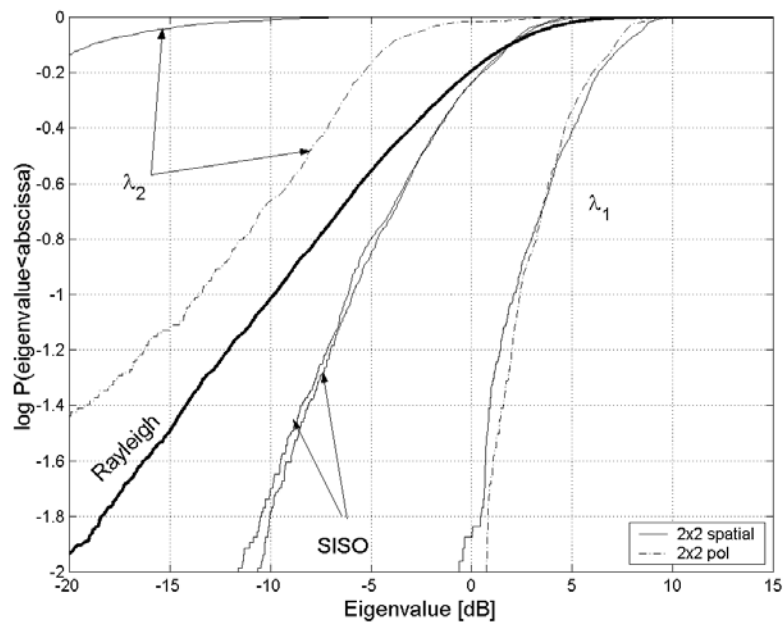
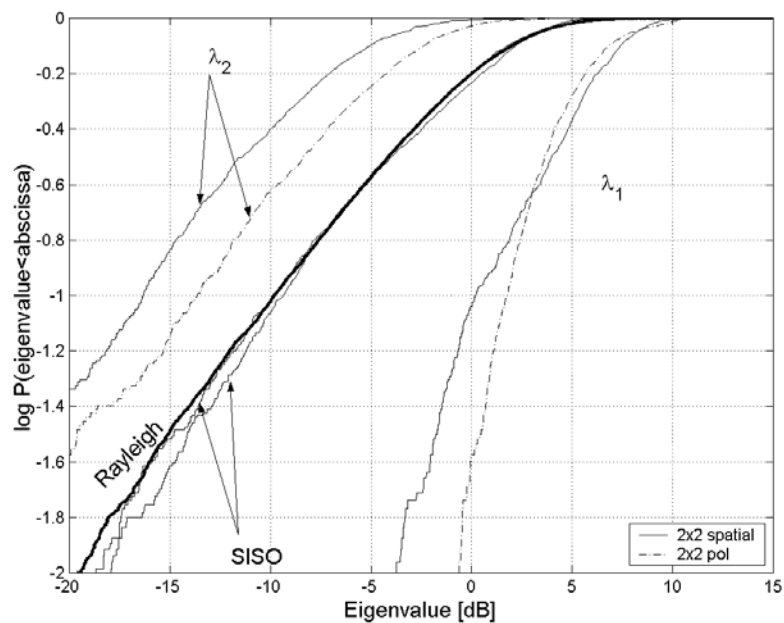


Figure 46 (i) presents the radio channel classified as partially correlated in the spatial domain for the two MEA set-ups. The power gain of the second subchannel, λ_2 , is improved when polarization diversity is employed. This was to be expected since the correlation coefficient showed lower correlation when polarization diversity was employed than using spatial diversity.

Therefore polarization diversity can be used as a remedy to make MIMO systems more robust with respect to the radio channel. However the use of polarization diversity on its own limits the number of MEAs elements. Combining polarization diversity with spatial diversity could be performed to increase the number of elements and subsequently increase the MIMO technology performance. This is addressed in the next section.



(i) Example 3, partially correlated scenario in the spatial domain, but partially decorrelated in the polarization domain.



(ii) Example 4, partially decorrelated scenario in the spatial and polarization domain.

Figure 46: Comparison of the spatial and the polarization diversity technique using 2x2 MIMO MEA configuration for two distinct radio channel spatial correlation classes.

8.1.4 Joint Spatial-Polarisation Domain

In this section, two advantages of using the joint spatial-polarisation domain in MIMO technology are addressed: robustness and compactness.

Recall that the joint spatial-polarization correlation coefficient is the product of the polarization and the spatial correlation coefficients as it was shown earlier in a microcell environment. Therefore, it is unlikely that both diversity techniques fail simultaneously.

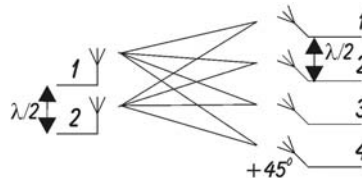
8.1.4.1 Robustness Advantage

To provide a quantitative order of performance when applying joint spatial-polarization diversity to the MIMO concept, capacity results based on measured data are presented hereafter which illustrate the impact of such diversity techniques. The MEA elements at the BS are all polarized to $+45^\circ$. This orientation is due to physical measurement limitation. A comparison between the following MEAs topology is performed.

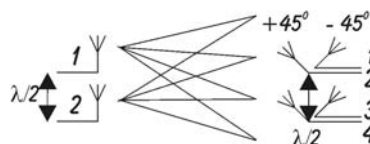
- 1×1 spatial: The MS consists of a vertical polarized element and the BS consists of one $+45^\circ$ element.



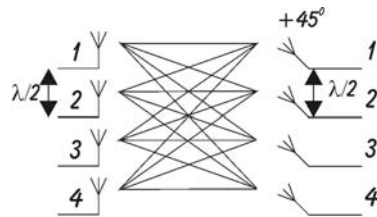
- 2×4 spatial: The MS consists of two vertical polarized elements with a spacing of 0.5λ and spatial diversity is only introduced at the BS with also a spacing of 0.5λ between the 4 elements.



- 2×4 spatial+pol: The MS consists of two vertical polarized elements with a spacing of 0.5λ and combines two $\pm 45^\circ$ elements with spatial diversity, i.e. 0.5λ , between the two pairs.



- 4×4 spatial: The MS consists of four vertical polarized elements with a spacing of 0.5λ and spatial diversity is only introduced at the BS with also a spacing of 0.5λ between the 4 elements.



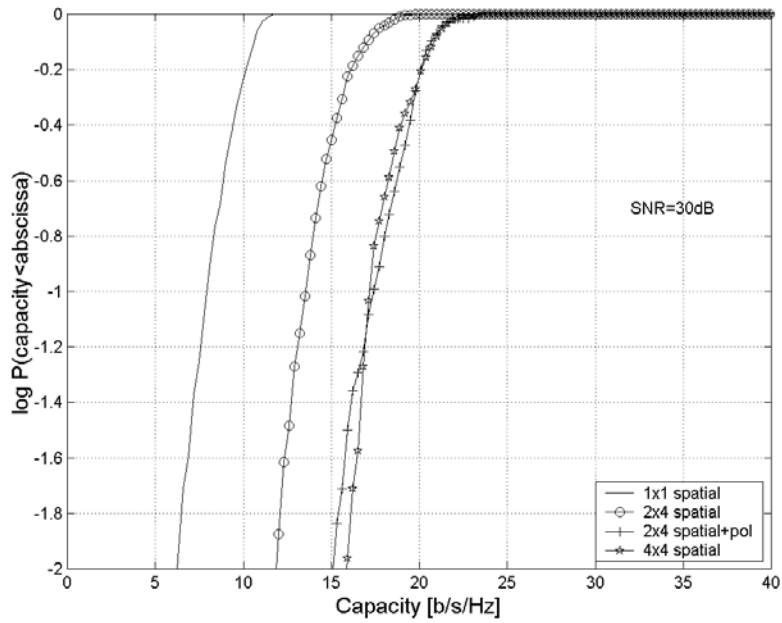
The analysis considers the same microcell environments as earlier, Example 3 and Example 4, the partially correlated and decorrelated propagation scenarios in the spatial domain investigated during the SUNBEAM measurement campaign respectively. The total capacity achievable with such a set of MIMO topology is presented in Figure 47 (i) for the partially decorrelated scenario and Figure 47 (ii) for the partially correlated propagation scenario in the spatial domain.

It is believed that a 2x4 set-up is a reasonable configuration for a practical implementation of the MIMO technology for a UMTS system, i.e., two elements can be fitted at the handset and four elements at the BS and therefore the analysis is focused on these 2x4 systems.

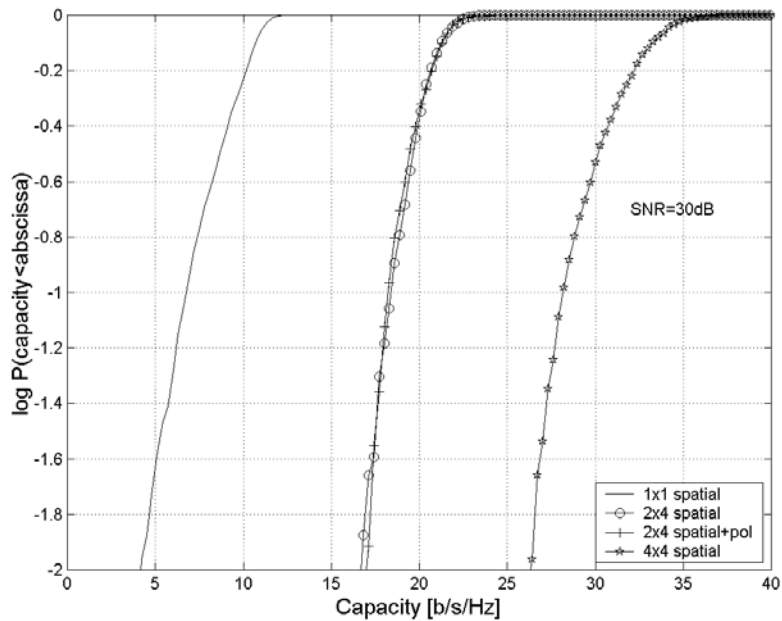
For the partially decorrelated situation in Example 4, the combined 2x4 spatial-polarization diversity system provides a higher total capacity than the 2x4 spatial diversity system. Using the polarization diversity, the correlation at the BS is low and as a consequence, two effective parallel channels are created, which are similar in performance to the 4x4 spatial diversity system. The capacity gain achieved by the 2x4 and 4x4 spatial set-up compared to the 1x1 system is the result of a Tx diversity gain since the elements of the MEA indoors are partially decorrelated. The parallel subchannelling is not exploited.

However, in Figure 47 (ii) the propagation channel is already partially decorrelated in the spatial domain, therefore the added decorrelation due to the polarization diversity is not significant. This results in the same total capacity, with or without polarization diversity for the 2x4 MEA set-up. Here, the 4x4 system takes advantage of the four parallel subchannels hence a large achieved capacity.

Once again, it confirms the fact that the use of the joint spatial-polarization diversity is an attractive solution to achieve high decorrelation between the MEA elements when the radio channel is partially correlated in the spatial domain, and subsequently provides a more robust system in terms of spectral efficiency for microcell environments.



(i) Example 3, partially correlated in the spatial domain.



(ii) Example 4, partially decorrelated in the spatial domain.

Figure 47: Capacity comparison for different MEA set-ups.

8.1.4.2 Compactness Advantage

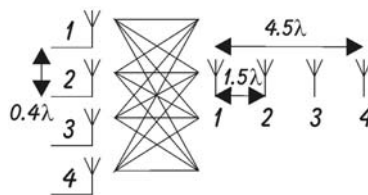
For indoor picocell environments, large number of element MEAs are likely to be implemented for WLAN application so high bit rate data transfer can be performed. Physical size becomes an issue if only spatial diversity is considered. The use of collocated dual polarised MEA can provide low correlation for a reasonable MEA physical size when large number of element is considered.

In this section, the analysis focuses on picocell scenarios. The investigation is based upon measured data collected during the METRA project. One path is considered here with two 4x4 MIMO systems since the measured data obtained in such a environment indicated equal BPR at both the MS and the BS. This path has been introduced in Section 5.5 on page 54 and is reminded below:

- **Example 5**: partially decorrelated scenario in the spatial domain from the nokia environment, where the patch MEA are $\pm 45^\circ$ orientated.

The two MIMO systems differ in the type of MEA configuration used at the BS as presented in the following.

- 4x4 spatial: The MS consists of four vertical polarized elements with a spacing of 0.4λ and the BS consists also of four vertical polarized elements but with a spacing of 1.5λ .



- 4x4 spatial+pol: The MS consists of four vertical polarized element and the BS consists of two dual polarised $\pm 45^\circ$ patch MEAs with 3λ separation.

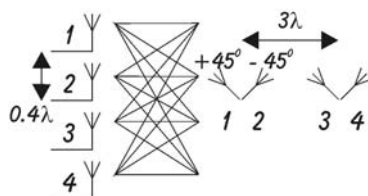


Figure 48 illustrates the performances of the first 4x4 {spatial} MIMO system. The MIMO system takes full advantage of the spatial propagation channel since it is shown in Section 5.4 that for picocell environments the spatial separation employed during the measurement was relatively low. Four eigenvalues can be identified, 2 of them being significant ($P > 0$ dB at 10% level).

When considering the second MIMO system employing joint spatial-polarization diversity in Figure 49, the results are similar. Recall that the graphs present the normalized eigenvalue therefore the two graphs can be compared.

Using four dipoles or two dual polarised patch MEAs at the BS provides the equivalent results in terms of subchannel gain in the measured MIMO radio channel. This also emphasizes that using joint spatial-polarisation diversities permits the use of more compact MEA set-ups when a large number of elements is to be deployed.

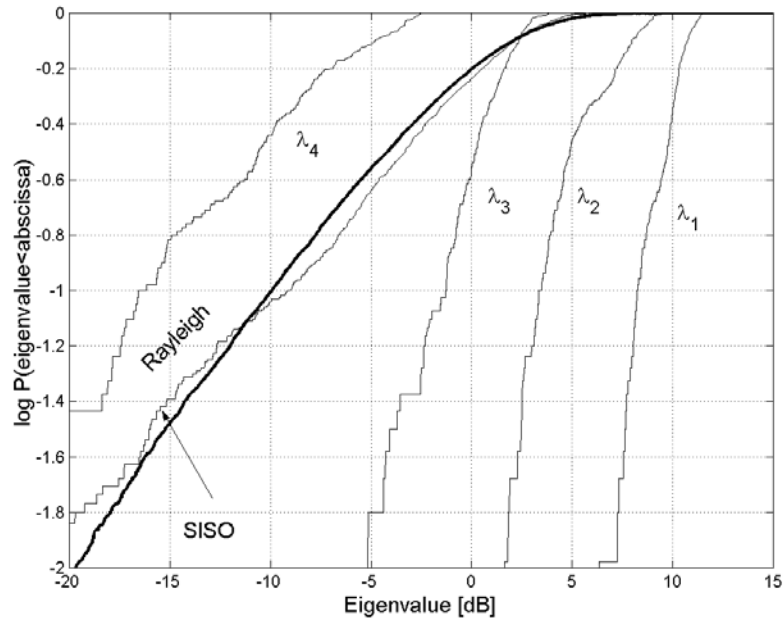


Figure 48: MIMO Eigenvalue distributions result for 4 dipoles at the MS and 4 dipoles at the BS for Example 5.

The above results were presented for a single path. In order to have a global overview of the performance of the MIMO system when employing joint spatial-polarization diversity, an analysis has been performed over all the measurement positions of the picocell environments Novi2, Novi3 and Nokia. The reason for selecting these three picocell environments is that the patch elements at the BS had the same orientation, i.e., $\pm 45^\circ$, in all three and as a result, the branches had equal BPR.

The power gain of each subchannel was extracted for each measurement path (see Figure 49) at 10% level and cumulated so that the cdf was computed. The empirical cdf of the power gain of each subchannel is presented in Figure 50.

The first two subchannels offer little variance in the power gain for the various measurement paths for the three investigated picocells. For the weaker eigenvalues, the slope is less steep. However, they have practically no significant impact on the MIMO performance. This indicates that for a picocell environment, with a BS employing $\pm 45^\circ$ patch MEA, almost identical power gain is to be expected for the joint spatial-polarization technique for all the measurement paths.

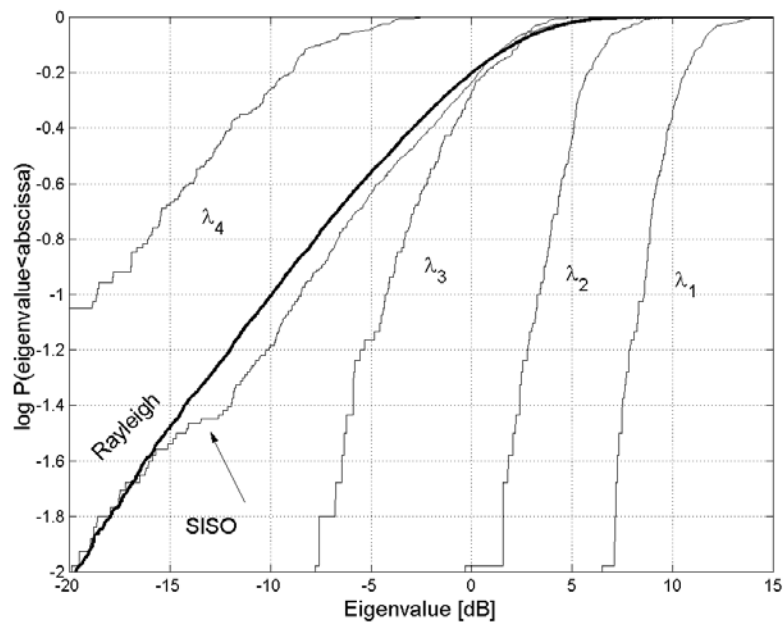


Figure 49: MIMO Eigenvalue distributions result for 4 dipoles at the MS and 2 dual polarised $\pm 45^\circ$ patches for Example 5. Very similar behaviour to Figure 48 for the dipole configuration.

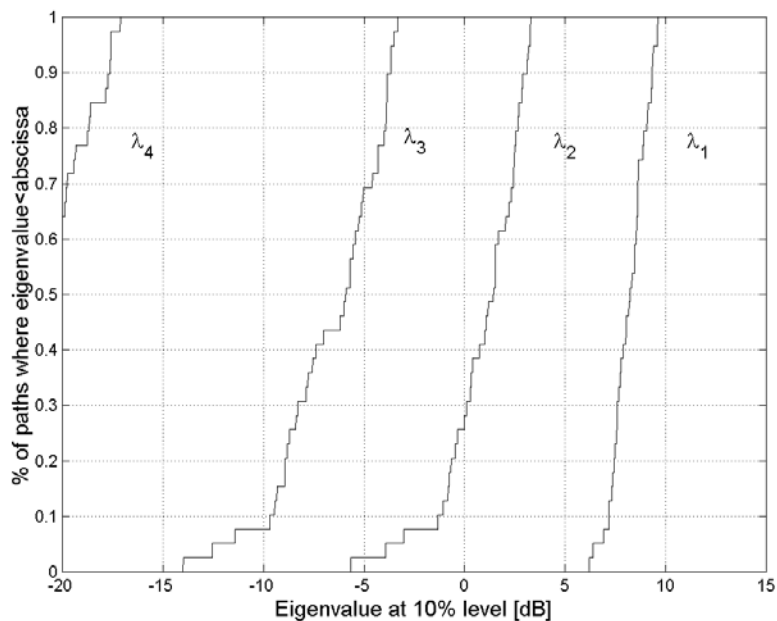


Figure 50: Power gain of the parallel subchannels for 4(dipoles) \times 2($\pm 45^\circ$ patch) MIMO configuration. The power gain is extracted from the 10% outage level of the eigenvalue (Figure 49) for each measurement paths in Novi2, Novi3 and Nokia where the $\pm 45^\circ$ patch orientation is employed.

8.2 Branch Power Ratio: A Practical Issue

In this deliverable, the correlation coefficient behaviour has been analysed to investigate the performance of a MIMO system assuming an equal BPR as defined in Section 4.7.

This section addresses the scenario where the BPR is unequal, which is a real implementation issue when using dual polarised MEAs. The investigation is based upon measured data collected during the METRA project and considers two distinct picocell environments where the dual polarized patch MEAs at the BS are set differently, $\pm 45^\circ$ and $90^\circ/0^\circ$, therefore exhibiting different BPRs. They have been introduced in Section 5.5 on page 54 and are reminded below:

- **Example 5**: partially decorrelated scenario in the spatial domain from the nokia environment, where the patch MEA are $\pm 45^\circ$ orientated.
- **Example 6**: partially decorrelated scenario in the spatial domain from the airport environment, where the patch MEA are $90^\circ/0^\circ$ orientated.

Table 10 summarises the element configurations with their associated BPR and power correlation coefficients for one measured path of each of the two picocell environments. The value of $|\rho_{S_A}|$, $|\rho_P|$, $|\rho_{S_A+P}|$ and the BPR for the two examples are averaged over the 8 possible elements of the MS. The correlation values are very low in both scenarios, whereas the BPR is very different. One should note that, in practice, for a same environment, tilting the antenna would affect not only the BPR but also the correlation coefficient [35].







| Path | Environmer | MEA set-up at the BS | BPR [dB] | $ \rho_{pow} $ |
|-----------|------------|--|----------|----------------|
| Example 5 | Nokia | P  | 0.9 | 0.22 |
| | | $S_A + P$  | 1.4 | 0.23 |
| | | S_A  | 0.7 | 0.22 |
| Example 6 | Airport | P  | -8 | 0.16 |
| | | $S_A + P$  | -8 | 0.12 |
| | | S_A  | 0.3 | 0.11 |

Table 10: Summary of the MEA configurations with their associated BPR and correlation coefficient for a 1×2 scenario where the element at the MS is vertically polarised.

In this section, the analysis follows three steps. A first study case focuses on a SIMO configuration to understand the propagation mechanism involved when the BPR varies from low to high values. Next, a second study case is presented using a 2×2 MIMO configuration for the two extreme BPRs. Finally the capacity performance is investigated and the impact of the BPR is outlined.

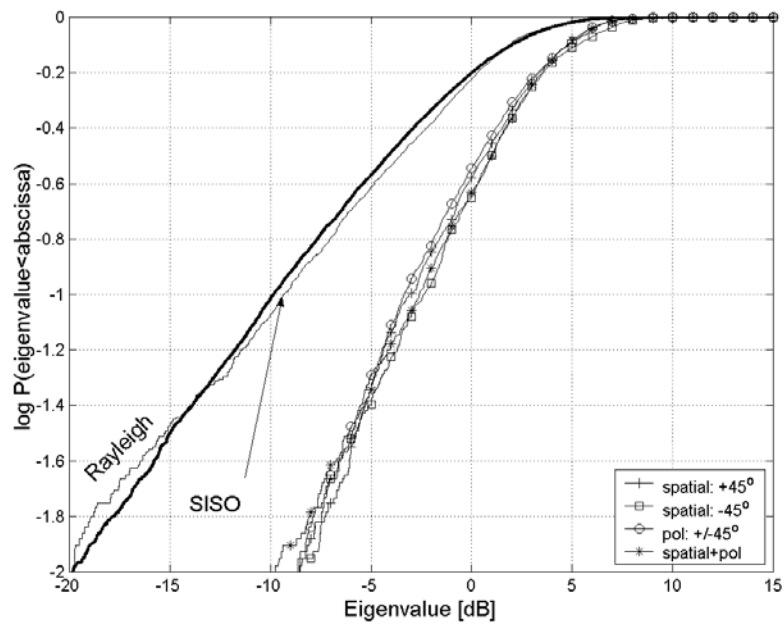
8.2.1 SIMO Approach

Figure 51 presents the cdfs of the eigenvalue computed for a 1×2 MEA configuration for $\pm 45^\circ$ and $90^\circ/0^\circ$ element patches orientation. A vertically polarised dipole at the MS and a dual polarised patch at the BS are considered. In order to increase the statistical significance, the cdfs were computed over all the 8 elements at the MS. The cdfs are normalized to the strongest 1×1 radio channel due to the imbalance in the average received power. For the $\pm 45^\circ$ case, the mean received power would be up to 3 dB lower than in the $90^\circ/0^\circ$ case.

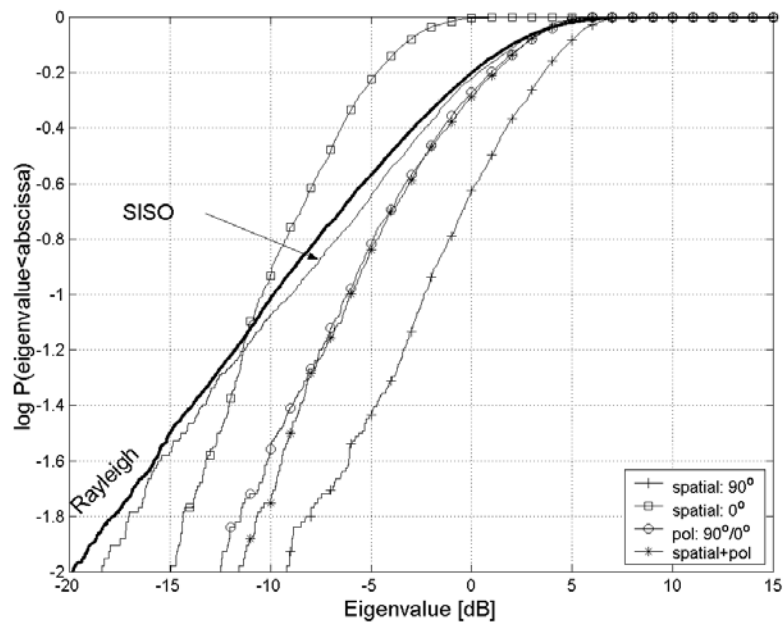
Figure 51 (i) presents the Example 5 where the patch MEA is set such that it exhibits a $\pm 45^\circ$ polarisation. It illustrates that the power gain from using two elements spatially separated but with a low BPR, is the same whether the $+45^\circ$ or the -45° element is used. There is no gain added to the spatial diversity technique by using polarisation diversity since $\rho_{s\Delta}$ is already low. Note the diversity gain compared to the SISO scenario.

In Figure 51 (ii), i.e., the Airport environment, the patch is rotated by 45° in the elevation plane such that a vertical (90°) and horizontal (0°) polarisation is achieved. It shows an imbalance in the available power gain depending on which branch is used. The 1×2 (0°) spatial set-up is 8 dB lower than the 1×2 (90°) spatial set-up. The polarization ($90^\circ/0^\circ$) and the spatial-polarization set-up have a higher gain compare to the 1×2 (0°) spatial MEA since the (90°) branch can still capture more energy than the (0°), but this gain remains negligible compared to the power gain of the 1×2 (90°) spatial set-up.

On the lowest power branch, i.e., 0° , a gain is noticeable due to the use of polarisation diversity but it remains negligible compared to the power gain of the 90° branch.



(i) Example 5: the nokia environment with the $\pm 45^\circ$ MEAs set-up



(ii) Example 6: the airport with the 90° and 0° MEAs set-up. Note the imbalance in the power gain compared to the above figure.

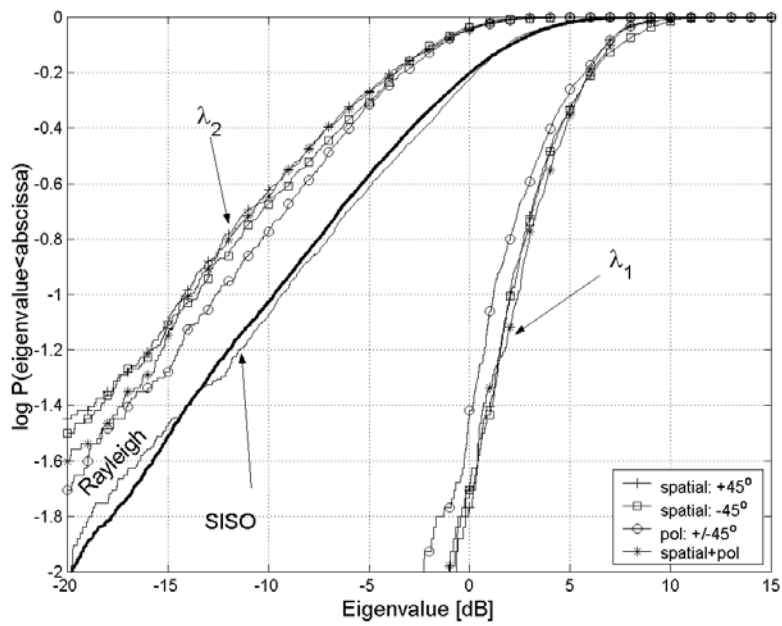
Figure 51: Illustration of the influence of the BPR on the power gain for a 1×2 SIMO configuration.

8.2.2 MIMO Approach

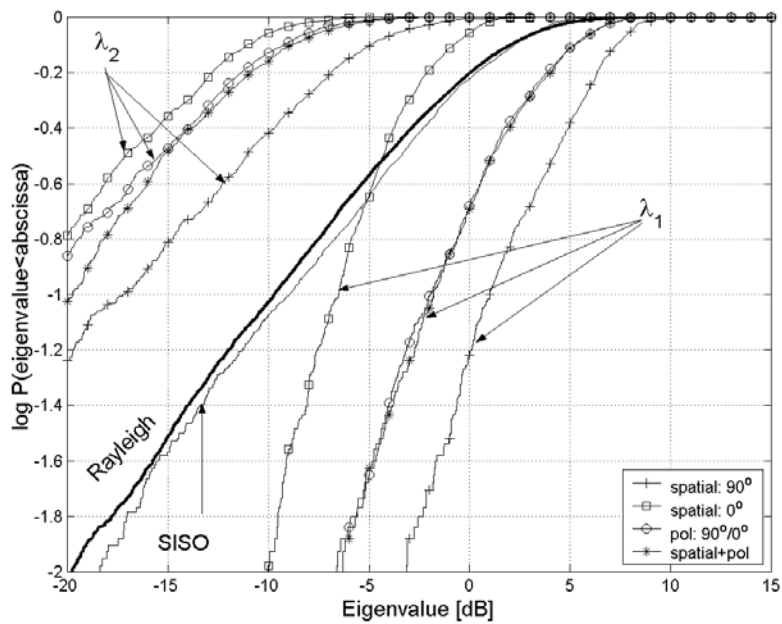
Figure 52 presents the MIMO extension of the previous SIMO analysis. The same picocell paths, MEA topology and eigenvalues normalization are used at the BS as in the example of Figure 51. Two vertical polarised elements are considered now at the MS.

Figure 52 (i), equal BPR scenario, shows that the two eigenvalues λ_1 and λ_2 exhibit a similar behaviour whether using spatial diversity $+45^\circ$, spatial diversity -45° , polarization diversity $\pm 45^\circ$, or joint spatial-polarization diversity.

Figure 52 (ii), BPR = -8 dB scenario, shows that the imbalance exhibited in the BPR drastically degrades the MIMO performance. λ_1 and λ_2 remain the same as in Figure 52 (i) when spatial diversity uses 90° since the transmitted signal is vertically polarised whereas when the $+0^\circ$ branches are used, λ_1 and λ_2 drop down to -8 dB. The performance of the eigenvalues is also influenced by the BPR when considering the polarization and the joint spatial-polarization diversity even though $|\rho_P|$ and $|\rho_{S\Delta+P}|$ are very low.



(i) Example 5: $\pm 45^\circ$



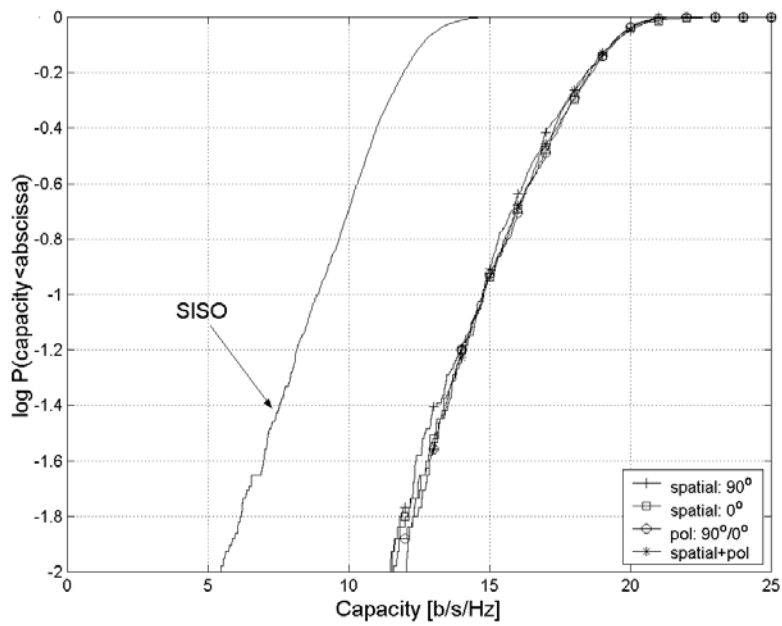
(ii) Example 6: 90° and 0°

Figure 52: Illustration of the influence of the BPR on the eigenvalue for a 2x2 MIMO configuration.

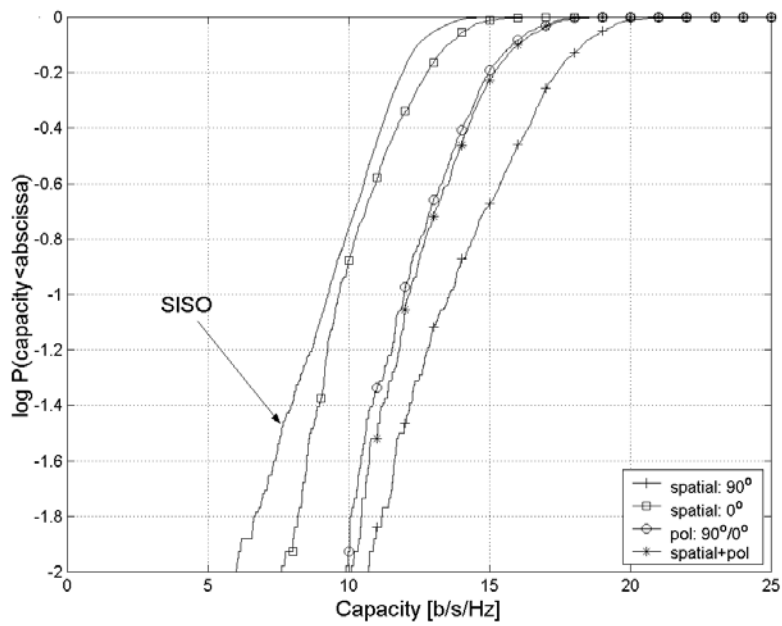
8.2.3 Capacity Results

Figure 53 presents the total capacity computed from the measured data for the two situations for a mean SNR per Rx element of 30 dB. When an equal BPR is present, Figure 53 (i), a total capacity of 15 b/s/Hz is achieved at 10% level for all three diversity techniques. Figure 53 (ii) shows that with an unbalanced BPR, the capacity performance of the polarization and the joint spatial-polarization diversity drops to 12 b/s/Hz, although the power correlation values are the same. When spatial diversity is employed, the drop is even more pronounced when the opposite polarization is considered since a drop to 10 b/s/Hz is noticeable.

To conclude, although the correlation coefficient indicates strong decorrelation, no optimal MIMO configuration, in the robust sense, can be achieved when the BPR is unbalanced. Therefore when designing a MIMO system, it is recommended to deploy simultaneously equal BPR and low correlation coefficient MEA system.



(i) Example 5: $\pm 45^\circ$, equal BPR.



(ii) Example 6: 90° and 0° . Note the impact of the unequal BPR.

Figure 53: Illustration of the influence of the BPR on the total capacity for a 2×2 MIMO configuration.

8.3 Capacity Results for Microcell and Picocell

This section addresses the performance of the MIMO system in a more general perspective and the total theoretical capacity to be achieved by a MIMO system is presented for cell-specific situations for a single user scenario.

Making use of the model, Figure 54 illustrates the simulated total capacity at 10% outage level for different SNRs per Rx element when the water filling power allocation scheme is used. Two MEA set-ups, a 4×4 and a 2×4, are compared using spatial diversity only. The simulations are performed by extracting the input parameters from the measured data of the two paths introduced in Section 5.5 on page 54 and are reminded below:

- **Example 1**: partially decorrelated scenario in the spatial domain selected from a picocell path.
- **Example 2**: partially correlated scenario in the spatial domain selected from a microcell path

The simulated capacity vs. SNR, on a logarithmic scale, increases in a linear manner, but its slope is proportional to the number of subchannels being taken into account in the summation of equation (4.13) on page 23 reminded below

$$C = \sum \log_2 \left(1 + \lambda_k \frac{P_k}{\sigma_n^2} \right)$$

At low SNR, the contribution of the first subchannel, i.e., λ_1 , is dominant. For higher SNRs, all the subchannels are present in equation (4.13) and consequently, the summation process takes over so that all four subchannels contribute to the total capacity. As a consequence, for a high SNR, the slope of the 4×4 MEA set-up capacity versus SNR is twice the slope of the capacity plot for the 2×4 MIMO set-up. Only 2 parallel subchannels are achieved in the second MEA set-up compared to the 4 parallel subchannels achieved by the 4×4 MIMO set-up. This means that when taking a SNR of 50 dB for instance, an increase in SNR of 3 dB provide 4 b/s/Hz for a 4×4, 2 b/s/Hz for a 2×2 and only 1 b/s/Hz for a conventional 1×1 wireless system.

Four conclusions can be drawn from these examples:

- The total capacity increases with the SNR.
- The partially decorrelated situation provides more capacity than the partially correlated scenario at the same SNR and with the same MEA set-up.
- In the partially decorrelated scenario, the 4×4 MEA configuration takes full advantage of its additional available subchannels compared to the 2×4 set-up at high SNR.
- At low SNRs, MIMO systems only provide a combined Tx and Rx diversity and at high SNRs, the MIMO topology benefits from parallel subchannelling.

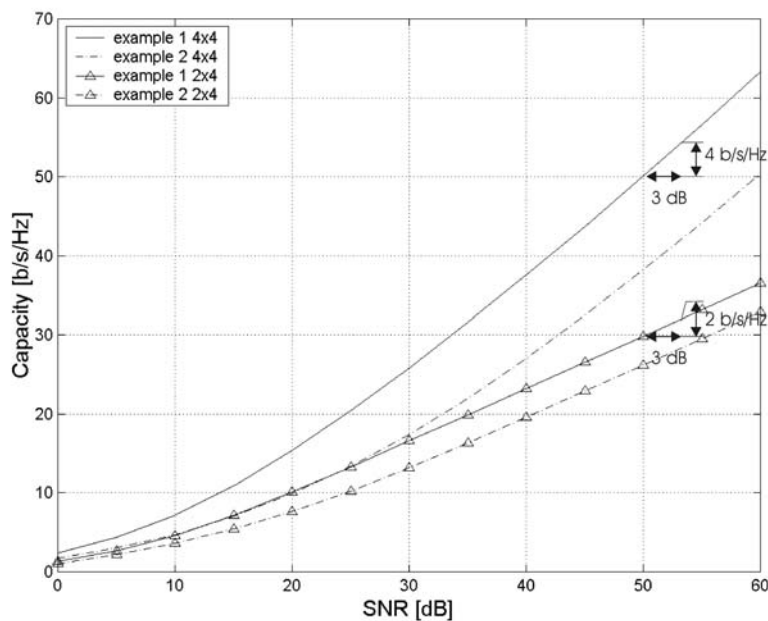


Figure 54: Simulated capacity (10% level) vs. SNR for Example 1 (Picocell - Partially decorrelated) and Example 2 (Microcell - Partially correlated). Use of the water filling power allocation strategy.

Figure 55 presents the cdf of the simulated capacity calculated with a mean SNR per Rx element of 30 dB and the input parameters extracted from all the 79 measured picocell paths. The simulated capacity results are robust for the picocell environments since the capacity results are less than 25 b/s/Hz and 27 b/s/Hz at the 10% and 90% percentage level respectively for a 4×4 MEA configuration, if water filling is used. This fluctuation of 2 b/s/Hz is explained by the fact that the elements of the MEAs at both the BS and the MS are sufficiently decorrelated for a sufficient amount of paths in picocell environments as previously demonstrated in this deliverable. In the context of a MIMO scenario this is interesting since multiple parallel subchannels are available. It can therefore be concluded that even in situations where LOS is present in picocell environment, a MIMO topology using spatial diversity with small spacing is favourable. The difference between the two power allocation schemes is insignificant for a 2×4 MIMO set-up since the number of parallel subchannels is low. The difference becomes more significant as the number of potential parallel subchannels increases.

Figure 56 presents the cdf of the simulated capacity which input parameters are derived from the 28 measured microcell paths. The simulated capacity exhibits much larger variation than for picocell environment (Figure 55) from 16 b/s/Hz to 27 b/s/Hz at the 10% and 90% cdf level respectively. This is explained by the use of two different element spacings. The variation from 20 b/s/Hz to 27 b/s/Hz is attributed to the set-up using 1.5λ while the low capacity contribution from 16 b/s/Hz to 20 b/s/Hz is obtained when applying only 0.5λ .

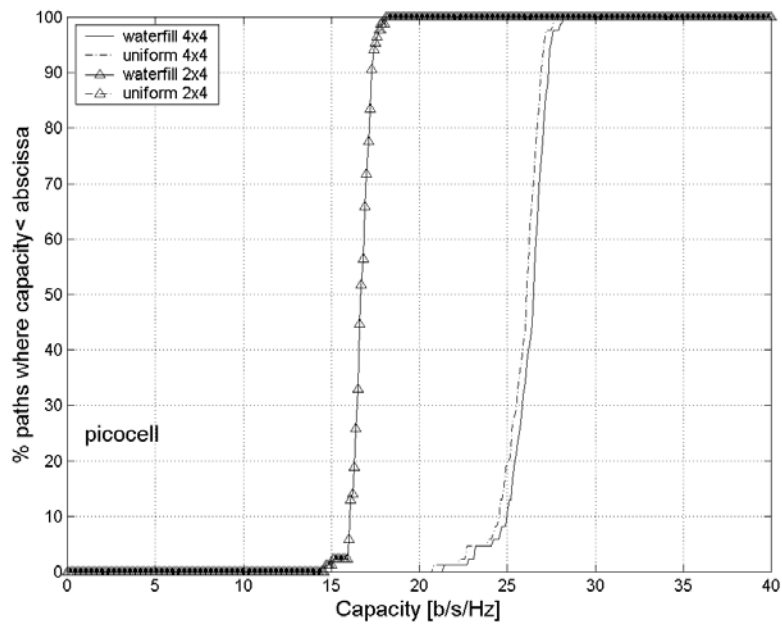


Figure 55: Cdf over the 79 picocell paths of the total capacity from capacity vs. SNR at SNR=30dB for 4x4 and 2x4 MEA configurations.

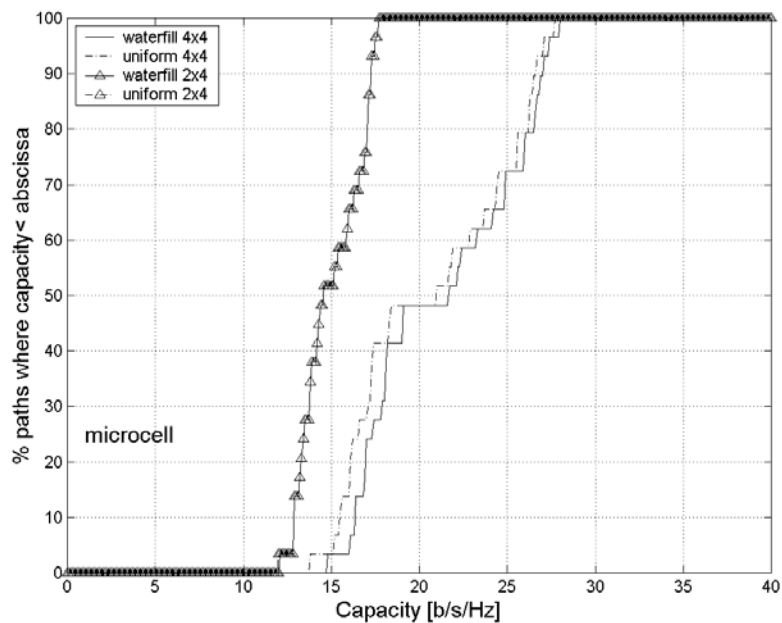


Figure 56: Cdf over the 28 microcell paths of the total capacity from capacity vs. SNR at SNR=30dB for 4x4 and 2x4 MEA configurations.

In microcell environments, the correlation, and subsequently the capacity, is strongly influenced by the nature of the surrounding scatterers and also by the element separation in the MEA. Scenarios with high correlation between MEA elements degrade the

potential high bit rate of the MIMO set-up. Therefore, the use of spatial diversity technique, on its own, is not recommended for a MIMO topology when using 0.5λ element spacing at the BS. However, when 1.5λ is employed, microcell capacity results are similar to those measured in the picocell environments.

8.4 Summary and Interim Conclusion

In this section, the impact of the propagation properties of the radio channel on the parallel subchannelling concept has been presented emphasizing on the spectral efficiency achievable when using the MIMO technology.

The quality of the MIMO technology is dependent on the number of elements in the MEA employed, the correlation properties of the MIMO radio channel, and the BPR between the elements of the MEA system.

Two opposite propagation paths were selected as examples of a partially decorrelated and partially correlated paths. For the picocell environment, it was found that spatial diversity, with spatial separation as low as 0.4λ can provide low correlation and thereby high bit rate. However, this is not the case for the microcell environment. Simulated capacity results calculated with a mean SNR per Rx element of 30 dB indicates 25 b/s/Hz and 27 b/s/Hz at the 10% and 90% level respectively for a 4×4 MEA configuration, if water filling is used in the picocell environment. For the microcell environment, for the same percentage level 16 b/s/Hz to 27 b/s/Hz can be achieved when spatial diversity is used. Therefore polarization diversity can be used as a remedy to make MIMO systems more robust with respect to the radio channel. However the use of polarization diversity on its own limits the number of MEAs elements.

Combining polarization diversity with spatial diversity is recommended to design a robust and compact MIMO system with large number of element at the MEAs. This can only be achieved if equal BPR and low correlation coefficient are both present when designing a MIMO system.

9 CONCLUSIONS

The main objective of Workpackage 2 was to perform a thorough characterisation of the MIMO propagation channel based on measured data collected during the ACTS SUNBEAM and the IST METRA projects. The outcome of this analysis was supposed to be sets of propagation parameters characterising the properties of MIMO channels in order to reproduce them with the help of an improved channel model. On the other hand, the potential capacity enhancement through MIMO channels was to be assessed with the help of Shannon's theoretical capacity formula, in order to present recommendations on the optimal ways to benefit from MIMO systems, keeping in mind that the potential benefits lie in the creation of orthogonal subchannels, the combination of Tx and Rx diversity and an increase in the antenna gain.

First of all, this deliverable has documented the extraction of propagation parameters based on the measured data obtained from the ACTS SUNBEAM and the IST METRA projects. This analysis helps to understand the propagation radio channel and to further elaborate on the interpretation of the behaviour of MIMO systems.

The statistical distribution of the NB signal and the analyses of *K-factor* and DoA have been used together to categorise the environment investigated in terms of their LOS/NLOS and low/high AS characteristics. Based on the information of the DoA, it has been concluded that the angular distribution of the waves indoor is typically not uniform, but rather exhibits a clustered (or multimodal) distribution. Hence a meaningful PAS could not easily be obtained. Additionally, the DoA analysis lead to the conclusion that the WSS requirement did not hold along some measurement routes.

Furthermore, a detailed investigation of the power correlation coefficient indicated that elements separated by 0.4λ would provide low correlation ($\rho \leq 0.6$ for 90% of the measured paths) in picocell environments. For microcell environments, the correlation coefficient at the MS is also low for 0.4λ -spacing, whereas larger spacings would be required at the BS to achieve a low correlation coefficient with spatial diversity only. When polarization diversity is implemented, the orientation of the elements is of critical importance, since an unequal BPR can lead to a drastic deterioration of the MIMO technology performance despite the antenna elements are weakly correlated. It has also been shown that the joint spatial-polarization diversity technique represents the optimum solution to build compact MEA set-ups which exhibit low correlation values in both picocell and microcell environments.

On the other hand, an upgrade of the stochastic MIMO radio channel model presented in Deliverable 2 of the IST METRA project has been performed. It can handle power imbalanced and dual-polarised antenna elements, and deliver complex field correlation coefficients as outcome. This upgrade has also been an opportunity to implement the channel model on the MATLAB[®] platform, in compliance with 3GPP standardisation as of April 2002. Already validated in the spatial domain, the proposed stochastic channel model has also been assessed in polarization diversity scenarios. In this case, two different implementations have been described, depending on the nature of the scattering. Since only one of the two families of scattering scenarios has been observed during SUNBEAM and METRA measurement campaigns, the validation has been limited to that family.

To conclude the analysis of the measured MIMO scenarios, the theoretical Shannon capacity has been computed from measured and simulated data in order to quantify the impact of the propagation properties on the performances of MIMO systems. It was outlined that their performances depend on the type of antenna elements employed in the MEA, on their BPR, and on the scattering characteristics of the MIMO radio channel. Simulated capacity results at a mean SNR per receive element of 30 dB indicate a high bit rate up to 25 b/s/Hz and 27 b/s/Hz at 10% and 90% of the measured picocell paths respectively for a 4×4 MEA configuration. For microcell environments, for the same percentage level, a strong fluctuation of 16 b/s/Hz to 27 b/s/Hz can be observed when only spatial diversity is used. Therefore, combining polarization diversity with spatial diversity is recommended to design a robust and compact MIMO system. However, this can only be achieved with equal BPRs and low correlation coefficients. It is also important to stress that at low SNRs, MIMO systems only provide a combined Tx and Rx diversity gain whereas parallel subchannelling is the main benefit at high SNRs.

Based on radio propagation results, theoretical results indicate that significant capacity enhancements are achievable thanks to the MIMO technology, for large numbers of decorrelated elements at both the MEAs, with equal BPRs and large SNRs. In the case of UMTS applications, the lack of space on the handset could be an issue when commonly proposed MEAs (4 and more antenna elements) are considered. Multimode MEAs [75], [76] are an interesting approach to alleviate this issue. However, another issue is the typically low operating SNR of UMTS applications (10-15 dB). At first sight, one could argue that the conditions listed here above, e.g. many uncorrelated antenna elements, equal BPRs and large SNRs, could be more easily fulfilled in the case of WLAN applications, since better SNRs would be experienced in smaller cell sizes and since larger numbers of antenna elements could be placed on the back of typical WLAN terminals like laptops. However, it should be stressed here that the analysis performed in Workpackage 2 focused on UMTS scenarios, not WLAN ones. Other choices would have been made for the collection of measurement data and their post-processing, should WLAN have been the main topic, for instance to address the frequency selectivity of WLAN applications due to their larger bandwidths. Therefore, the comments here above on the applicability of MIMO for WLAN are mostly speculative.

10 APPENDIX A - EXPERIMENTAL VALIDATION IN THE POLARIZATION DOMAIN

This appendix presents the validation procedure of the stochastic MIMO radio channel in the polarization domain. The outcome of the validation is presented in Section 6.

10.1 MIMO Structure Considering Polarization Diversity

The NB MIMO radio channel matrix \mathbf{H}_{pola} including polarization diversity is constructed such that

$$\mathbf{H}_{pola} = \begin{bmatrix} \mathbf{H}_{VV} & \mathbf{H}_{HV} \\ \mathbf{H}_{VH} & \mathbf{H}_{HH} \end{bmatrix} \quad (10.1)$$

where \mathbf{H}_{IJ} is a subchannel matrix considering the polarization I and J at the MS and at the BS, respectively. It is implicit that the index V represents the vertical polarization and H the horizontal polarization so $I, J \in \{H, V\}$.

\mathbf{H}_{IJ} is defined as

$$\mathbf{H}_{IJ} = [\alpha_{i,j}]_{i,j \in \{1,2\}} \quad (10.2)$$

where $\alpha_{i,j}$ is the complex NB transmission coefficient from element I_i at the MS to element J_j at the BS, as illustrated in Figure 57. The implementation of the polarization diversity technique in the model is described in the flow chart in Figure 58.

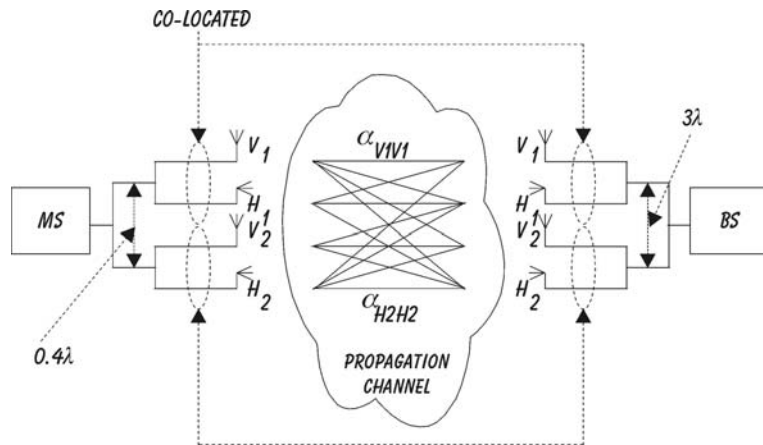
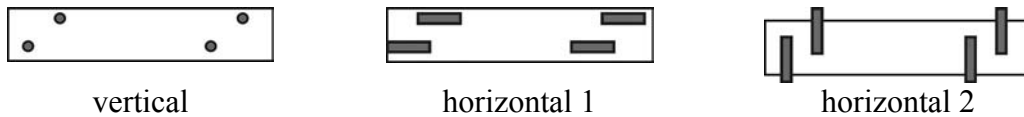


Figure 57: Illustration of the MIMO radio channel case study considering collocated dual polarized elements.

10.2 Experimental Implementation of MIMO in the Polarization Domain

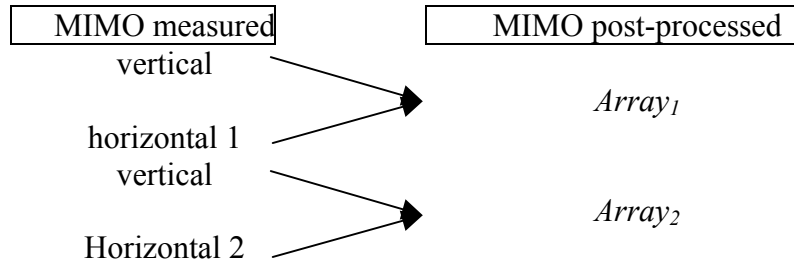
The validation of the model in the polarization domain was based on the METRA measurement data. At the MS, the measurement of one path was repeated using three sets of MEAs: vertical (V_{set}), horizontal 1 (H_{set1}) and horizontal 2 (H_{set2}).

In the validation presented here, two linear MEA set-ups with 4-element each, later denoted as $Array_1$ and $Array_2$, are derived from these three measurement set, after post processing. $Array_1$ and $Array_2$ respectively combine V_{set} with H_{set1} and V_{set} with H_{set2} as shown below.



For each 4-element MEA, two dual polarized elements are collocated and the pairs are separated with 0.4λ as illustrated in Figure 57.

At the BS, two dual polarised patch MEAs with a separation of 3λ were considered for the analysis. Recall that depending of the investigated environment, the patch MEAs were employed with different orientations.



10.3 The Correlation Assumption with respect to Polarization

The correlation properties in the spatial domain of the MIMO radio channel are obtained by the Kronecker product of two independent correlation matrices defining the correlation properties at the MS and BS ends respectively. The underlying assumption is that the correlation properties at a given end does not depend on the element used as reference at the other end, because all elements of a given end are experiencing the same power azimuth spread.

This assumption can be questioned when dual-polarized MEAs are considered. However, if the double dual-polarized set-up (dual-polarized MEAs at both ends) is split into four single-polarized MEAs, where a single polarization is considered at a time at each end, this philosophy can be applied again as explained in the following.

Therefore, the channel correlation matrix can be expressed as

$$\mathbf{R} = \begin{bmatrix} \mathbf{R}_{VV} & \mathbf{R}_{HV} \\ \mathbf{R}_{VH} & \mathbf{R}_{HH} \end{bmatrix} \quad (10.3)$$

where

$$\mathbf{R}_{IJ} = \begin{bmatrix} \mathbf{R}_{IJ}^{ms,V} \otimes \mathbf{R}_{VV}^{bs} & \mathbf{R}_{IJ}^{ms} \otimes \mathbf{R}_{HV}^{bs} \\ \mathbf{R}_{IJ}^{ms} \otimes \mathbf{R}_{VH}^{bs} & \mathbf{R}_{IJ}^{ms,H} \otimes \mathbf{R}_{HH}^{bs} \end{bmatrix} \quad (10.4)$$

with $\mathbf{R}_{IJ}^{ms,Q}$ being the matrix of the correlation coefficients $\rho_{ms,iiJj}^{bs,Qq}$ between elements I_i and J_j of the MS seen from an element of polarization Q and index q at the BS. $\mathbf{R}_{IJ}^{bs,Q}$ is equivalent at the BS. Q is omitted when the correlation coefficient mixes the polarizations at both ends.

The independence assumption per polarization can be expressed as follows

$$\rho_{ms,ViVj}^{bs,Vq} = \langle \alpha_{Vi,Vq}, \alpha_{Vj,Vq} \rangle \quad (10.5)$$

$$\equiv \rho_{ms,ViVj}^{bs,Vl} = \langle \alpha_{Vi,Vl}, \alpha_{Vj,Vl} \rangle \quad (10.6)$$

and

$$\rho_{ms,ViVj}^{bs,Hq} = \langle \alpha_{Vi,Hq}, \alpha_{Vj,Hq} \rangle \quad (10.7)$$

$$\equiv \rho_{ms,ViVj}^{bs,Hl} = \langle \alpha_{Vi,Hl}, \alpha_{Vj,Hl} \rangle \quad (10.8)$$

Similar expressions can be written by switching the terms ms and bs in the previous relations.

At this stage, the question is whether this assumption can be extended to apply on elements differently polarized. This gives birth to two options:

- First option: **polarization-independent** definition

Mathematically, this option leads to the following relations

$$\rho_{ms,iiJj} = \rho_{ms,iiJj}^{bs,Vq} = \rho_{ms,iiJj}^{bs,Hq} \quad (10.9)$$

$$\equiv \rho_{bs,iiJj} = \rho_{bs,iiJj}^{ms,Vq} = \rho_{bs,iiJj}^{ms,Hq} \quad (10.10)$$

In this case, the generalised model described by relations (10.3) and (10.4) collapses to the original $\mathbf{R}_{MIMO} = \mathbf{R}_{MS} \otimes \mathbf{R}_{BS}$ since any correlation coefficient is independent of the polarization of a given reference element.

- Second option: **polarization-dependent** definition

Such a dependency in the polarization would occur in a strong LOS situation; for instance, in the case where ideal dual polarized MEAs exhibiting high discrimination between the two polarizations are used then the correlation coefficient ρ_{II}^I between elements of similar polarization is estimated from an element which has the same

polarization. A Rice type distribution occurs and therefore strong correlation exists ($\rho_{II}^I \cong 1$).

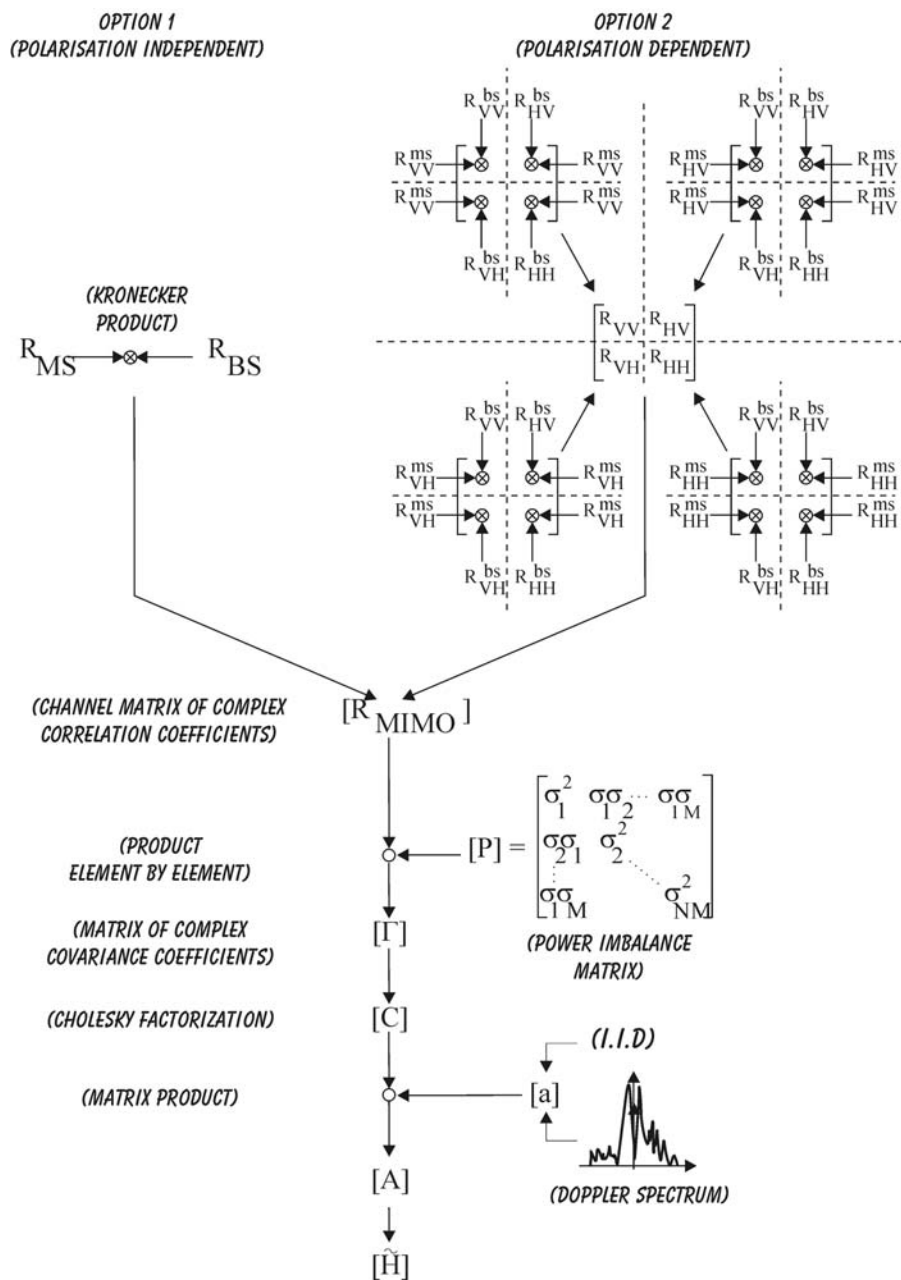


Figure 58: Flow chart of the MIMO model considering polarization diversity.

However, in a case where the correlation coefficient is still computed between elements of same polarization, but is estimated from an element which has a different polarization, then the distribution is more of a Rayleigh type because the signal needs to be significantly scattered in order for the opposite polarized element to receive the energy from the element using another polarization. As a result, low correlation occurs ($\rho_{II}^J \rightarrow 0$).

This difference in the result, i.e., ρ_{II}^J either $\rightarrow 0$ or $\cong 0$, indicates that the correlation depends on the polarization, and (10.9) and (10.10) are thus no longer valid. Moreover, in this case, correlation coefficients ρ_{IJ} (for $I \neq J$) tend to zero as well.

Consequently, the matrix \mathbf{R} would have a block structure where each block is defined as

$$\mathbf{R}_{II}^{ms,J} = \mathbf{R}_{JJ}^{bs,I} \quad (10.11)$$

The rest of the model is identical to that of Section 6.1 as it is seen in Figure 58.

10.4 Determination of the Model Option

In order to determine which option of the model to consider with respect to the METRA measurement data, the relations (10.9)-(10.10) are assessed.

The correlation coefficients $\rho_{ms}^{bs,ref}$ between the elements at the MS (or BS) have been estimated with respect to the elements (*ref*) at the BS (or MS). Then the difference

$$\Delta(\rho_{ms}^{bs,ref1}, \rho_{ms}^{bs,ref2}) = \rho_{ms}^{bs,ref1} - \rho_{ms}^{bs,ref2}, \quad (10.12)$$

has been computed and its cdf generated over all the measurement paths where the elements at the BS are $+90^\circ/0^\circ$ polarized. For the sake of simplicity this equation is calculated at the MS, but it is similar at the BS.

Figure 59 presents the dependency of the correlation coefficient at the MS with respect to

- the vertical element only, i.e., $\left| \Delta(\rho_{ms,v1v2}^{bs,V1}, \rho_{ms,v1v2}^{bs,V2}) \right|$, (legend ‘o’),
- the horizontal element only, i.e., $\left| \Delta(\rho_{ms,v1v2}^{bs,H1}, \rho_{ms,v1v2}^{bs,H2}) \right|$, (legend ‘□’), and
- both the vertical and horizontal element at the BS, i.e., $\left| \Delta(\rho_{ms,v1v2}^{bs,V}, \rho_{ms,v1v2}^{bs,H}) \right|$, (legend ‘+’).

All the cdfs exhibit a median smaller than 0.15 which is considered to be a positive result and supports the first option of the model, i.e., *polarization-independent*. This indicates that based on empirical results, the determination of the correlation coefficient is independent of the polarization employed at the other end of the path. Therefore **option 1** is considered for evaluating the validity of the MIMO channel model in the polarization domain.

This analysis is performed with the METRA measured data which indicated a low *K-factor* (see Figure 8). It has not been possible to extract a path with a strong LOS which would illustrate option 2 and hence option 1 is still valid even in a LOS situation with the

measured data. If high K -factor values had been present the conclusion could have been different.

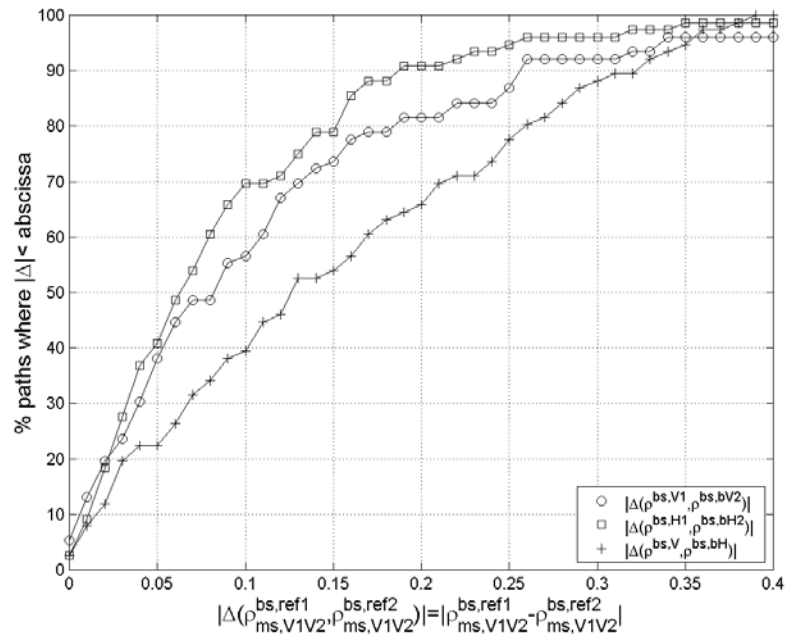


Figure 59: Assessment of relations (10.9)-(10.10). The cdfs present the dependency of the empirical correlation coefficient at the MS with respect to the BS elements.

11 REFERENCES

- [1] L. Schumacher, J. P. Kermoal, F. Frederiksen, K. I. Pedersen, A. Algans and P. E. Mogensen, "MIMO Channel Characterisation", IST Project IST-1999-11729 METRA Deliverable 2, February 2001.
- [2] P. E. Mogensen, K. I. Pedersen, J. P. Kermoal and T. B. Sørensen, "2D Radio Channel Study", ACTS SUNBEAM AC347 Deliverable 411, July 1999
- [3] J.P. Kermoal, "Measurement, Modelling and Performance Evaluation of the MIMO Radio Channel", Ph.D. thesis, Aalborg University, Denmark, 2002.
- [4] <http://www.umts-forum.org/>
- [5] <http://www.wlan.org/>
- [6] Sir W. Stewart (chairman), "Mobile Phones and Health", Independent Expert Group on Mobile Phones, 2000.
- [7] K.I. Pedersen, "Antenna Arrays in Mobile Communications: Channel Modeling and Receiver Design for DS-CDMA Systems", Ph.D. thesis, Aalborg University, Denmark, 2000.
- [8] R.B. Ertel, P. Cardieri, K.W. Sowerby, T.S. Rappaport, and J.H. Reed, "Overview of Spatial Channel Models for Antenna Array Communication Systems", IEEE Personal Communications, pp. 10-22, February 1998.
- [9] H. Holma and A. Toskala, "WCDMA for UMTS Radio Access for Third Generation Mobile Communications", Revised Edition, John Wiley & Sons, LTD., 2001.
- [10] I.E. Telatar, "Capacity of Multi-Antenna Gaussian Channels", AT&T-Bell Labs Internal Tech. Memo. (see <http://mars.belllabs.com/cm/ms/what/mars/index.html>), June 1995.
- [11] <http://www.ist-metra.org/>
- [12] <http://www.3gpp.org/>
- [13] <http://cpk.auc.dk/schum/MIMO/index.html>
- [14] J.B. Andersen, "Array Gain and Capacity for Known Random Channels with Multiple Element Arrays at Both Ends", IEEE Journal on Selected Areas in Communications-Wireless Communication Series, vol. 18, no. 11, pp. 2172-2178, 2000.
- [15] J. Kivinen, P. Suvikunnas, D. Perez, C. Herrero, K. Kalliola, and P. Vainikainen, "Characterisation System for MIMO channels", in Proceedings of 4th International Symposium on Wireless Personal Multimedia Communications WPMC'01, September 2001.
- [16] M.J. Gans, N. Amitay, Y. S. Yeh, H. Xu, T.C. Damen, R.A. Valenzuela, T. Sizer, R. Storz, D. Taylor, W.M. MacDonald, C. Tran, and A. Adamiecki, "Outdoor blast measurement system at 2.44 GHz: calibration and initial results", IEEE Journal on Selected Areas in Communications, vol. 20, no. 3, pp. 570-583, April 2002.
- [17] D. Chizhik, G.J. Foschini, M.J. Gans, and R.A. Valenzuela, "Keyholes, Correlations and Capacities of Multielement Transmit and Receive Antennas", IEEE Transactions on Wireless Communications, vol. 1, no. 2, pp. 361-368, April 2002.
- [18] K. I. Pedersen, J.B. Andersen, J.P. Kermoal, and P. Mogensen, "A Stochastic Multiple-Input-Multiple-Output Radio Channel Model for Evaluation of Space-Time Coding Algorithms", IEEE Vehicular Technology Conference VTC 2000 Fall, Boston, USA, vol. 2, pp. 893-897, September 2000.
- [19] D.S. Shiu, G.J. Foschini, M.J. Gans, and J.M. Kahn, "Fading Correlation and Its Effects on the Capacity of Multielement Antenna Systems", IEEE Transactions on Communications, vol. 48, no. 3, pp. 502-513, March 2000.
- [20] D. Gesbert, H. Bölcskei, D. Gore, and A. Paulraj, "MIMO wireless channels: capacity and performance prediction", GLOBECOM '00, IEEE Global Telecommunications Conference, San Francisco, USA, 2000, vol. 2, pp. 1083-1088, November 27-December 1 2000.
- [21] A. Sibille, "Keyholes and MIMO Channel Modelling", COST 273 TD(01)017, October 2001, Bologna, Italy.
- [22] P. C. F. Eggers, "Angular Dispersive Mobile Radio Environments Sensed by Highly Directive Base Station Antennas", IEEE Proc. PIMRC'95, vol. 2, pp. 522-526, September 1995.
- [23] W. C. Y. Lee, "Effects on Correlation Between Two Mobile Radio Base-Station Antennas", IEEE Transactions on Vehicular Technology, vol. 22, no. 4, pp. 130-140, November 1973.
- [24] F. Adachi, M.T. Feeney, A.G. Williamson, and J.D. Parsons, "Crosscorrelation Between the Envelopes of 900 MHz Signals Received at a Mobile Radio Base Station Site", IEE Proceedings, vol. 133, Pt. F, no. 6, pp. 506-512, October 1986.

- [25] J. Salz and J.H. Winters, "Effect of Fading Correlation on Adaptive Arrays in Digital Mobile Radio", IEEE Transactions on Vehicular Technology, vol. 43, no. 4, pp. 1049-1057, November 1994.
- [26] K.I. Pedersen, P.E. Mogensen, and B.H. Fleury, "Spatial Channel Characteristics in Outdoor Environments and their Impact on BS Antenna System Performance", VTC'98, Ottawa, Canada, pp. 719-724, May 1998.
- [27] B.H. Fleury, "First- and Second-Order Characterization of Direction Dispersion and Space Selectivity in the Radio Channel", IEEE Transactions on Information Theory, vol. 46, no. 6, September 2000.
- [28] P. Petrus, J.H. Reed, and T.S. Rappaport, "Effects of Directional Antennas at the Base Station on the Doppler Spectrum", IEEE Communications Letters, vol. 1, no. 2, March 1997.
- [29] D. Chizhik, G.J. Foschini, and R.A. Valenzuela, "Capacities of multi-element transmit and receive antennas: Correlations and Keyholes", Electronics Letters, vol. 36, no. 13, pp. 1099-1100, June 22 2000.
- [30] J. B. Andersen, "Constraints and Possibilities of Adaptive Antennas for Wireless Broadband", Proc. International Conference on Antennas and Propagation, ICAP, Manchester, UK, vol. 1, pp. 220-225, April 2001.
- [31] J.B. Andersen, "Antenna Arrays in Mobile Communications-Gain, Diversity, and Channel Capacity", IEEE Antennas and Propagation Magazine, vol. 42, no. 2, pp. 12-16, April 2000.
- [32] C.E. Shannon, "Communication in the Presence of Noise", Proceedings of the IRE and waves and electrons, pp. 10-21, January 1949.
- [33] S. Haykin, *Communication Systems*, Prentice Hall International, third edition, 1994.
- [34] P. Kyritsi, D.C. Cox, R. A. Valenzuela, and P.W. Wolniansky, "Effect of Antenna Polarization on the Capacity of a Multiple Element System in an Indoor Environment", Accepted for publication in the IEEE J. Select. Areas Commun., August 2002.
- [35] R.G. Vaughan, *Antenna Diversity in Landmobile Communications*, Ph.D. thesis, Aalborg University, Denmark, 1985.
- [36] P.C.F. Eggers, J. Toftgård, and A.M. Oprea, "Antenna Systems for Base Station Diversity in Urban Small and Micro Cells", IEEE Journal on Select Areas in Communications, vol. 11, no. 7, pp. 1046-1057, September 1993.
- [37] Jr. W. C. Jakes, *Microwave Mobile Communications*, John Wiley and Sons, Inc, 1974.
- [38] W. C. Y. Lee, *Mobile Communications Engineering*, McGraw-Hill Book Company, 1982.
- [39] J.A. McFadden, "The Correlation Function of a Sine Wave Plus Noise after Extreme Clippings", IRE Trans. on Inf. Theory, pp. 82-83, June 1956.
- [40] J.N. Pierce and S. Stein, "Multiple Diversity with Nonindependent Fading", Proceedings of the IRE, pp. 89-104, January 1960.
- [41] P.C.F. Eggers, "Envelope Correlation Coefficients of Rayleigh Fading Signals Corrupted by Additive Gaussian Noise", COST 231 TD(96) 02, 24-26 January 1996, Belfort.
- [42] C. A. Balanis, *Antenna theory*, Wiley, second edition, 1982.
- [43] B.D. Jeffs and D. Elsmore, "Maximally sparse reconstruction of blurred star field images", ICASSP-91, International Conference on Acoustics, Speech, and Signal Processing, vol. 4, 1991.
- [44] Korhonen, *Measuring and Estimating Instantaneous Wideband Radio Channel by Regularized Convolution*, Ph.D. thesis, Helsinki University Of Technology, Finland, 1999.
- [45] Q.H. Spencer, B.D. Jeffs, M.A. Jensen, and A.L. Swindlehurst, "Modeling the Statistical Time and Angle of Arrival Characteristics of an Indoor Multipath Channel", IEEE Journal on Selected Areas in Communications, vol. 18, no. 3, March 2000.
- [46] A. A. M. Saleh and R. A. Valenzuela, "A Statistical Model for Indoor Multipath Propagation", IEEE Journal on Selected areas in communications, vol. 5, no. 2, pp. 128-137, February 1987.
- [47] P. C. F. Eggers, "Internal Note on variance subtraction," Tech. Rep., 1995.
- [48] J. B. Andersen, T. S. Rappaport, and S. Yoshida, "Propagation Measurements and Models for Wireless Communications Channels", IEEE Communications Magazine, vol. 33, no. 1, pp. 42-49, January 1995.
- [49] L.J. Greenstein, D.G. Michelson, and V. Erceg, "Moment-Method Estimation of the Ricean K-Factor", IEEE Communications Letters, vol. 3, no. 6, pp. 175-176, June 1999.
- [50] M.B. Knudsen, *Antenna Systems for Handsets*, Ph.D. thesis, Aalborg University, Denmark, 2001.
- [51] R.J. Mailloux, *Phased Array Antenna Handbook*, Artech House, 1994.
- [52] J. Liberti, "Measuring and Modelling Spatial Radio Channels for Systems", Proc. 1998 IEEE Antennas and Propagation Society Int'l. Symposium, Atlanta, USA, June 1998.

- [53] K. Kalliola, *Experimental Analysis of Multidimensional Radio Channels*, Ph.D. thesis, Helsinki University, Finland, 2002.
- [54] E. Hecht, *Optics*, Addison-Wesley Publishing Company, second edition, 1987.
- [55] O. Nørklit, *Adaptive Antennas in Mobile Communication*, Ph.D. thesis, Aalborg University, Denmark, 1996.
- [56] B.D. Van Veen and K.M. Buckley, "Beamforming: A Versatile Approach to Spatial Filtering", *IEEE ASSP Magazine*, pp. 4-24, April 1988.
- [57] A.V. Oppenheim and R.W. Schaffer, *Discrete-Time Signal Processing*, Prentice Hall Processing Series, 1989.
- [58] E.C. Ifeachor and B.W. Jervis, *Digital Signal Processing: A Practical Approach*, Addison-Wesley Publishers Ltd., 1993.
- [59] J.C. Liberti and T.S. Rappaport, *Smart Antennas for Wireless communications: IS-95 and Third Generation CDMA Applications*, Prentice Hall PTR, 1999.
- [60] H. Dam, *Smart Antennas in GSM System*, M.S. thesis, Aalborg University, Denmark, 1995.
- [61] P.C.F. Eggers, J. Toftgård, and A.M. Oprea, "Antenna Systems for Base Station Diversity in Urban Small and Micro Cells", *IEEE Journal on Selected Areas in Communications*, vol. 11, no. 7, pp. 1046-1057, September 1993.
- [62] T. Klingenbrunn and P. Mogensen, "Modelling Cross-Correlated Shadowing in Network Simulations", *Proc. IEEE Vehicular Technology Conference*, September 1999.
- [63] L. Schumacher, K.I. Pedersen and P.E. Mogensen, "From Antenna Spacings to Theoretical Capacities – Guidelines for Simulating Spatial Correlation in MIMO Systems", *Proc. 13th IEEE International Symposium on Personal Indoor Mobile and Radio Communications*, Lisbon, Portugal, September 2002.
- [64] MIMO Rapporteur, 3GPP document R1-02-0141 "MIMO conference call summary", January 2002.
- [65] J.P. Kermaol, L. Schumacher, K.I. Pedersen and P.E. Mogensen, "A Stochastic MIMO Radio Channel Model with Experimental Validation", *IEEE Journal on Selected Areas in Communications*, vol. 20, n.6, August 2002, pp. 1211-1226.
- [66] K. I. Pedersen, J.B. Andersen, J.P. Kermaol and P.E. Mogensen, "A stochastic multiple-input-multiple-output radio channel model for evaluation of space-time coding algorithms", *Proc. 52nd IEEE Vehicular Technology Conference VTC 2000 Fall*, Boston (USA), September 2000, vol. 2, pp. 893-897.
- [67] M.R. Buehrer, "The Impact of Angular Energy Distribution on Spatial Correlation", *Proc. 56th IEEE Vehicular Technology Conference VTC 2002 Fall*, Vancouver (Canada), September 2002,
- [68] <http://www.synopsys.com>
- [69] MIMO Rapporteur: 3GPP TSG R1-02-0181, "MIMO discussion summary", January 2002.
- [70] G.H. Golub and C.F. Van Loan, "Matrix Computation", The Johns Hopkins University Press, 3rd edition, 1996.
- [71] M.J. Heikkilä, K. Majonen, J.R. Fonollosa, R. Gaspa, M.A. Lagunas, M. Lamarca, X Mestre, D.P. Palomar, A. Pérez-Neira, E. Tiirola, J. Ylitalo, M. Dowds and D. Lister, "Review and Selection of Relevant Algorithms", IST Project IST-1999-11729 METRA Deliverable D3.2, June 2000.
- [72] 3GPP TR 25.869, "Tx diversity solutions for multiple antennas", version 0.1.1
- [73] <http://www.ist-imetra.org>
- [74] SCM AHG: SCM-062, "Spatial Channel Model Text Description", October 2002.
- [75] T. Svantesson, "An antenna solution for MIMO channels: the multimode antenna", *ASILOMAR'2000*, vol. 2, pp. 738-742, November 2000.
- [76] T. Svantesson, *Antennas and Propagation from a Signal Perspective*, Ph.D. thesis, Chalmers University of Technology, Sweden, 2001.